

UNIVERSITY OF OKLAHOMA

GRADUATE COLLEGE

A KINEMATIC AND THERMODYNAMIC ANALYSIS OF THE 17 MAY 2019

MCCOOK / FARNAM, NEBRASKA TORNADIC SUPERCELL

A DISSERTATION

SUBMITTED TO THE GRADUATE FACULTY

in partial fulfillment of the requirements for the

Degree of

DOCTOR OF PHILOSOPHY

By

Martin Satrio

Norman, Oklahoma

2023

A KINEMATIC AND THERMODYNAMIC ANALYSIS OF THE 17 MAY 2019

MCCOOK / FARNAM, NE TORNADIC SUPERCELL

A DISSERTATION APPROVED FOR THE

SCHOOL OF METEOROLOGY

BY THE COMMITTEE CONSISTING OF

Dr. Mike C. Coniglio, Chair

Dr. Erik N. Rasmussen, Co-Chair

Dr. Cameron R. Homeyer

Dr. Mike I. Biggerstaff

Dr. Xuguang Wang

Dr. Nikola Petrov

© Copyright by Martin Satrio 2023

All Rights Reserved.

Acknowledgements

The experiences I gained within my PhD have been unforgettable and it wouldn't have been possible without the many people who have helped me along the way. Firstly, I would like to thank both of my advisors, Dr. Mike Coniglio and Dr. Erik Rasmussen, for granting me the opportunity to pursue research in supercell observations and for providing invaluable guidance along the way. They have not only been instrumental in the progression of this research, but their advice and expertise has made me a much better meteorologist. I would also like to deeply acknowledge Dr. Conrad Ziegler, who provided me not only with the code to conduct the quality control, objective analysis, wind synthesis, diabatic Lagrangian analysis, and trajectory calculations, but has also served as an informal mentor to me during the project. Given my unfamiliarity with observational work before the project began, he has supplied guidance on every step within the analysis, and the final product could not have been completed without the countless email threads and meetings with Conrad. I would also like to thank Dr. Dan Stechman, who answered my endless questions on working with raw radar data and quality control in SOLO3. I also thank my committee members, Dr. Cameron Homeyer, Dr. Mike Biggerstaff, Dr. Xuguang Wang, and Dr. Nikola Petrov for taking the time out of their busy schedules to attend advisory conferences, the general exam, and for ensuring the research conducted in this dissertation meets expectations. Finally, I would like to voice my immense appreciation for my family, friends, and anyone within or outside of the meteorological community

that helped me succeed in the last four years — it is the support from others which allows one to be the best version of themselves. Specifically, I would especially like to thank my parents, who are first generation immigrants to the United States, for working so hard and sacrificing so much starting even before I was born so that I could chase my dreams (and storms!). My parents have always pushed and encouraged me to pursue a career that I am passionate about, and since I was a little kid, I knew this is what I wanted to be — it is because of them that this is a reality. Most importantly, I want to thank my beautiful wife, Claire, who has shared my meteorological passions with me since high school. Through it all — high school, undergraduate, Master’s, and PhD programs — she has carried me through my struggles and pushed me to become a better meteorologist, researcher, and mostly importantly, a better person. She is the light of my life, even in the darkest of days. The importance of her support cannot be measured, and it is because of her that the completion of the last four years has been possible. Last, and certainly not least, thank you to my two dogs, Cali and Kira, for always being a source of joy, comfort, and paw-sitivity.

Contents

1 Chapter 1: Background	1
1.1 Background Studies	1
1.2 Low-Level Rotation	5
1.2.1 Previous Studies	5
1.2.2 Importance of Internal Supercell Boundaries	8
1.2.3 Recent Studies: The Streamwise Vorticity Current	12
1.3 Research Goals	18
2 Chapter 2: Analysis of 4D Kinematic Fields Retrieved via Multi-Doppler Analysis Techniques	20
2.1 Introduction	20
2.2 Data and Methods	21
2.2.1 Quality Control	22
2.2.2 Objective Analysis and Wind Syntheses	24
2.3 Event Overview	29
2.4 Kinematic Analysis	33
2.4.1 Segment 1	33
2.4.2 Segment 2	37
2.4.3 Segment 3	40
2.5 Trajectory Analysis and Potential Streamwise Vorticity Current (SVC)	44

2.6	Comparison to Mobile Mesonet Observations	51
2.7	Summary and Conclusion	55
3	Chapter 3: Analysis of 4D Thermodynamic Fields Retrieved via Diabatic Lagrangian Analysis	59
3.1	Introduction	59
3.2	Data and Methods	59
3.2.1	Diabatic Lagrangian Analysis	60
3.3	Comparison to Observations	64
3.3.1	Comparison of Surface Thermodynamics to Mobile Mesonet Observations	64
3.3.2	Comparison of Vertical Velocities and Above-Ground Thermo- dynamics to Sounding Observations	68
3.4	Thermodynamic Analysis	71
3.4.1	Updraft Structure	71
3.4.2	Evolution of Near-Surface Baroclinic Boundaries	77
3.5	Trajectory Analysis: Vorticity Budgets	81
3.5.1	Residuals	82
3.5.2	Analysis	84
3.6	Summary and Conclusions	90
4	Chapter 4: Thoughts on the Future of Observational Supercell Work	94

List of Tables

1	Specifications of the NOXP radar as operated on 17 May 2019.	114
2	Specifications of the aft and fore P3 radars as operated on 17 May 2019.	115
3	Analysis times of the P3 legs in format HH:MM:SS. The (L) or (R) indicates the positioning of the storm relative to the aircraft during that leg.	116
4	Data on all of the tornadoes that occurred within the analysis period, where PL = Path Length and MW = Max Width.	117
5	Parameters for the perturbation surface-layer downdraft, damping, and surface flux parameterizations similar to Table 1 in Ziegler (2013a). .	118

List of Figures

1	(Caption next page.)	119
1	Classic schematic on how vorticity generated from unidirectional environmental shear interacts with a single updraft (cylindrical arrows). Vortex lines are thin black arrows with sense of rotation given by the flat, white arrows. New forcing from updrafts / downdrafts shown by solid shaded arrows. (a) Initial perturbation upwards tilts the initially horizontal vortex line, creating cyclonic (anticyclonic) vertical vorticity on the southern (northern) flank of the storm. (b) As time progresses, the downdraft in the center of the storm tilts the vortex line downward resulting in storm splitting with a cyclonic / anticyclonic couplet associated with both cells. Figure from Klemp (1987).	120
2	(Caption next page.)	121
2	(a) Areas of relative high and low pressure as well as cyclonic and anticyclonic vertical vorticity in the case of (a) linear environmental shear and (b) nonlinear environmental shear. Cylindrical white arrows show the updraft, flat white arrows represent the direction of the shear vector at that particular level, and thick shaded arrows illustrate the resultant pressure gradient force. Figure from Klemp (1987).	122

3	Top-down schematic of a supercell from Lemon and Doswell (1979). The updraft (UD), forward-flank downdraft (FFD), and rear-flank downdraft (RFD) are annotated and shaded. Arrows represent streamlines and the solid line represents a typical radar reflectivity outline. The location of the outflow boundaries are also noted.	123
4	Volume rendering of streamwise vorticity from Orf et al. (2017). Locations of important features within the supercell, including the SVC, are noted in the figure.	124
5	Sounding released from a far-field vehicle on 17 May 2019 at 23:02:30 UTC. Green, thick orange, and light blue line indicates the dewpoint temperature, temperature, and virtual temperature, respectively. Gray line and thin orange line represent lifted parcel path using surface temperature and surface virtual temperature, respectively. Full, half wind barb, and flag indicates 10, 5, and 50 kts, respectively, with numbering next to the wind barb showing recorded height in km. Values in top right corner show calculated sounding parameters.	125
6	Figure taken from Ziegler (2013b) depicting the time-morphing algorithm used to map two consecutive non-synced radar analyses at T_2 and T_3 to a new analysis time t_{a3}	126

7	Panels (a) and (b) show the location of the sounding indicated by the black star from 17 May 23:02:30 UTC and 18 May 00:57:05 UTC, respectively, along with the closest corresponding radar image from KLNK. Panels (c) and (d) are as in Fig. 5 showing soundings at 23:02:30 UTC and 00:57:05 UTC.	127
8	Panels (a) and (b) show the linearly interpolated sounding with a $\Delta z = 0.25$ km at 17 May 22:57 UTC and 18 May 00:36 UTC. The red and green lines indicate temperature and dewpoint temperature while the black line indicates a lifted surface parcel. Wind barbs are given on the right hand side of the figures.	128
9	Damage track of the tornadoes on 17 May 2019 with the radar image from 22:55 UTC and 00:35 UTC overlaid underneath on the left and right panels, respectively (images from the Damage Assessment Toolkit, DAT; https://apps.dat.noaa.gov/stormdamage/damageviewer/). The triangles indicate each individual damage indicator while the lines represent the approximate track of a single tornado. The numbers in the right panel correspond to the tornado numbers in Table 4 (tornado #2 and #3 are not marked within the DAT).	129

10	Violin plots showing the distribution of positive vertical vorticity within 5 km of the 1 km AGL circulation. The bottom and top of the violin plot show the extrema of the distribution while the black and red lines show the median and 95 th percentile of the data. The dotted black vertical lines represent the separation between S1 / S2 and S2 / S3. The blue, green, yellow, and orange shading represent the times of EF-0, EF-1, EF-2, and EF-3 tornadoes.	130
11	Similar to Fig. 10 except for the negative of the Okubu-Weiss parameter at the surface.	131
12	Gray shaded gridded reflectivity and multi-Doppler wind synthesis horizontal wind vectors at 0.0 km AGL at (a) 22:57, (b) 23:00, (c) 23:03, and (d) 23:06 UTC. Black wind vectors represent those obtained by wind syntheses while gray wind vectors are those obtained by smoothing between wind syntheses and the background wind field. Colored triangles represent damage indicators. Green contours are Okubo-Weiss values contoured starting at $\pm 0.02 \text{ s}^{-1}$ every 0.01 s^{-1} (dashed contours represent negative values).	132
13	As in Fig. 12 but for 1 km AGL. Additionally, blue lines represent vertical velocity contours starting at $\pm 10 \text{ m s}^{-1}$ every 5 m s^{-1} (dotted blue contours represent negative values).	133

14	Sequence of images depicting the tilt of the tornado east of McCook, NE (tornado #1 in Table 4). Images are screenshots from video: https://www.youtube.com/watch?v=J5NYzRx5nhc	134
15	(Caption next page.)	135
15	(a–c) Gray shaded surface reflectivity with black contours of surface vertical vorticity starting from $\pm 0.01 \text{ s}^{-1}$ every 0.01 s^{-1} and blue contours of 1 km AGL vertical velocity starting at $\pm 10 \text{ m s}^{-1}$ every 5 m s^{-1} (dashed contours represent negative values) at 22:57, 23:00, and 23:03 UTC. Damage indicators are marked by the colored triangles. (d–f) Vortex lines (blue) at surface starting locations marked by black squares. Black circles represent clustering of vortex line arches and black arrows represent tilting vortex lines. Damage indicators are marked by colored squares, gray shading is gridded surface reflectivity, and solid / dashed black contours represent surface vertical vorticity as in panels (a–c).	136
16	(Caption next page.)	137

16	Streamline analysis via surface wind syntheses at (a) 23:09, (b) 23:18, (c) 23:27, (d) 23:39, (e) 23:48, and (f) 23:57 UTC with the thickness of the streamline proportional to the wind speed. Gridded surface reflectivity is gray shaded and contours of surface OW and 1 km vertical velocity are contoured in green and blue, respectively (values of contours are as in Fig. 13). Damage indicators are denoted with colored triangles.	138
17	As in Fig. 15 for (a) 00:06, (b) 00:12, (c) 00:18, (d) 00:24, (e) 00:30, and (f) 00:36 UTC.	139
18	Column-averaged vertical vorticity stretching (shaded) from the surface to 1 km AGL (5 total vertical grid levels) for the same analysis times as Fig. 17. Reflectivity is indicated by black contours starting from 5 dBZ every 5 dBZ. Arrows indicated surface horizontal wind vectors and damage indicators are represented by colored triangles.	140
19	Isosurfaces of vertical vorticity representing values of 0.03 s^{-1} (green) and 0.05 s^{-1} at the same analysis times as Fig. 17 and 18. 1 km reflectivity is color shaded. 1 km vertical vorticity is contoured in black every 0.01 s^{-1} , with dotted contours representing negative values.	141
20	(Caption next page.)	142

20	<p>Backward trajectories originating from 1 km AGL around a 1.5×1.5 km box around the low-level mesocyclone (red box) at (a) 23:45, (b) 23:51, (c) 00:00, (d) 00:15, (e) 00:24, and (f) 00:33 UTC. Middle figure in each panel shows reflectivity (gray-shaded) with arrows depicting surface horizontal wind vectors. Each backward trajectory is indicated by a colored line, with the color representing the starting height of the trajectory. Top figure in each panel gives an X-Z plane visualization of trajectories, and right figure gives a Y-Z plane visualization.</p>	143
21	<p>Top figure similar to Fig. 20 for 00:00 UTC, with the additional black line denoting the location of the cross section. Bottom panel shows the cross section with shaded reflectivity with arrows denoting winds in the cross-sectional plane.</p>	144
22	<p>Similar to Fig. 21 but for 00:15 UTC.</p>	145

23	<p>Observed mobile mesonet surface winds compared to the surface winds derived from multi-Doppler wind synthesis at (a) 00:06, (b) 00:15, (c) 00:24, and (d) 00:33 UTC. The gridded surface winds from analysis are indicated by smaller wind barbs superimposed on color-shaded reflectivity. Observed mobile mesonet winds are given by slightly larger wind barbs along the blue-shaded line — the line indicates the location of the mesonet vehicle which is spatially-corrected for storm motion while the color of the line represents potential temperature, with deeper blue colors indicating cooler θ values. Observed wind barbs are plotted every 20th measurement. The black dot indicates the start of the mesonet track and the black star represents the measurement taken at the analysis time.</p>	146
24	<p>Time series of θ_v from the mobile mesonet (black) and closest grid point in the DLA (blue). The orange line represents the DLA θ_v corrected by the median bias.</p>	147

25	(a) Comparison of vertical velocity from the sounding (blue) launched at 23:55:38 UTC using an assumed constant balloon ascent rate of 5 m s^{-1} and an error bar of 4 m s^{-1} (transparent shading). The orange line is the corresponding vertical velocity from the wind synthesis, and the red represents the wind synthesis minus the sounding vertical velocity with error bar shaded. (b) θ_v from the sounding, with colors corresponding to that of panel (a).	148
26	Same as Fig. 25 but for the sounding launched at 00:00:33 UTC.	149
27	(Caption next page.)	150
27	(a) Shaded plots of reflectivity, vertical velocity, θ_v perturbation, water vapor mixing ratio, rain / graupel / hail / snow mixing ratio, and cloud water / cloud ice mixing ratio with wind barbs at 6 km AGL at 23:30 UTC. The solid black line indicates the location of the cross section shown in panel (b) which shows the same variables in the same order as (a).	151
28	Same as in Fig. 27 but for 23:51 UTC.	152
29	Same as in Fig. 27 but for 00:12 UTC.	153
30	Same as in Fig. 27 but for 00:33 UTC.	154

31	Surface θ_v perturbation with surface wind vectors overlaid at (a) 23:30, (b) 23:36, (c) 23:42, (d) 23:48, (e) 23:54, and (f) 00:00 UTC. The black contours are surface reflectivity, with the thickness increasing every 10 dBZ starting from 30 dBZ.	155
32	Same as Fig. 31 but for (a) 00:06, (b) 00:12, (c) 00:18, (d) 00:24, (e) 00:30, and (f) 00:36 UTC.	156
33	Boxplots of streamwise, crosswise, and vertical vorticity accumulated residuals along the 36 trajectories over the 15 min for (a) 23:45, (b) 00:00, (c) 00:15, and (d) 00:30 UTC.	157
34	Vorticity tendency associated with forcing terms for streamwise (top left), crosswise (top right), and vertical vorticity (bottom left), along with the trajectory path superimposed on gray shaded reflectivity and 1 km AGL wind vectors at 2345 UTC (bottom right).	158
35	Vorticity tendency along 36 trajectories related to forcing associated with baroclinic streamwise vorticity (top left), stretching of streamwise vorticity (top right), tilting of horizontal vorticity into the vertical (bottom left), and stretching of vertical vorticity (bottom right). Colored lines represent each trajectory. The black line represents the median value and the red lines (and red shading) represent values in between the 25 th and 75 th percentiles.	159
36	Same as Fig. 34 except for a trajectory terminating at 00:00 UTC.	160

- 37 Same as Fig. 36 except for a different trajectory terminating at 00:00 UTC.160
- 38 Same as Fig. 35 except for all trajectories terminating at 00:00 UTC
which have an observed ζ value greater than 0.01 s^{-1} 161
- 39 Similar to Fig. 35 except for trajectories terminating at 00:15 UTC
which have a path through the forward-flank region (manually identified).162

Abstract

The Targeted Observation by Radars and UAS of Supercells field project successfully deployed on a cyclic tornadic supercell in southwest Nebraska on 17–18 May 2019. This case study uses data from the two airborne radars mounted onto the P3 along with the ground-based NOXP radar for a triple-Doppler wind synthesis from 17 May 22:57 UTC to 18 May 00:36 UTC. Wind syntheses and gridded reflectivity are ingested into a diabatic Lagrangian algorithm (DLA) to obtain gridded thermodynamic information including θ , θ_v , and various hydrometeor mixing ratios.

Low-level analyses in Chapter 2 show that the triple-Doppler winds capture general supercell behavior, including a transition from a weaker to stronger low-level mesocyclone (LLM) as the supercell becomes more actively tornadic, especially after 23:57 UTC. Vortex-line arches (VLAs) are shown to be associated with the first EF-2 tornado, but weak low-level updrafts likely resulted in the short-lived nature of the first tornado. After a clear reorganization period from 23:06 to 23:57 UTC, strengthening of near-surface rotation is coincident with northerly reorientation of the winds within the RFD. LLM strengthening is also coincident with a shift of LLM parcels originating from the forward-flank precipitation region rather than directly from the undisturbed inflow environment, matching well with numerical simulation results showing forward-flank parcels play a large role in LLM modulation. ζ stretching within the 0–1 km layer is relatively weak until 00:15 UTC, evidenced by two significant but short-lived (3 min and 4 min) tornadoes. After 00:15 UTC, however,

collocation of 0–1 km updrafts with ζ centered on and to the northwest of the circulation show consistent stretching, which likely contributed to a longer-lived, 18 min EF-1 tornado after 00:15 UTC. Isosurfaces of ζ show a deep, continuous mesocyclone at this time with the 0.05 s^{-1} isosurface connected from the ground to 9 km prior to occlusion at 00:30 UTC.

Evolution of surface baroclinic boundaries from the DLA in Chapter 3 reveal key changes as the supercell strengthens around 23:57 UTC — namely, a cold pool surge within the forward-flank region simultaneous with a surface warm pocket appearance at 23:48 UTC that leads to rear-flank downdraft maturation just before a significant tornado. Vorticity budgets along parcels terminating within the LLM at 00:00 UTC show clear evidence of baroclinic generation of streamwise horizontal vorticity along θ_v gradients. While observed SVCs have been noted in previous literature via cross-sectional or RHI analyses, this study is the first to explicitly compute vorticity budgets along parcel trajectories within a long-lived tornadic supercell, providing evidence that SVCs in numerical simulations are indeed physical.

1 Chapter 1: Background

1.1 Background Studies

Since the coining of the term “supercell” (Browning, 1964), considerable progress has been made in understanding the complex and highly nonlinear dynamical and thermodynamic structure and processes within such storms. Though studies prior to the advent of Doppler radar attempted to explain the observed persistent rotating updraft (e.g., Wegener, 1928; Brooks, 1949), it was not until remote sensing capabilities allowed for viewing of the overall structure that more significant progress was made. In addition to proposing the term “supercell”, Browning (1964) correctly hypothesized that one of the main roles of the updraft was to eject hydrometeors away from the inflow region and was one of the first to recognize the unique tendency for a supercell to propagate rightward in relation to the mean wind. Another role of the updraft was proposed to be a mechanism for the tilting of horizontal vorticity within the inflow environment into the vertical (Browning and Landry, 1963; Barnes, 1968), though this hypothesis posed an unsolved problem of its own — physically, if an updraft were to tilt environmental vorticity into the vertical, a mirror anticyclonic region should also be present. Recognition of a supercell split between a cyclonic and anticyclonic branch, first proposed by Fujita and Grandoso (1968); Browning (1968), would become essential in solving this issue.

The advent of Doppler Radar in the 1970s led to further breakthroughs in the

understanding of supercell dynamics, as this allowed for the capturing of three-dimensional wind fields for the first time using dual-Doppler techniques. For example, Ray (1976) showed that the mid-level mesocyclone does have a cyclonic-anticyclonic couplet associated with it, with the cyclonic (anticyclonic) portion focused mainly on the updraft (downdraft) and low-levels dominated by cyclonic flow. It was not until full three-dimensional numerical simulations were run by Klemp and Wilhelmson (1978a,b) that dynamical understanding of mid-level mesocyclone and storm splitting behavior really began to take place. One of the most important findings was that storm evolution differed greatly in the case of unidirectional environmental wind shear, in which the direction of the shear vector remained constant with height, versus the case in which there was both directional and speed shear, with the shear vector veering with height.

For the linear shear case, after storm splitting and supercellular characteristics begin to appear, the cyclonic and anticyclonic branches are equally favored, i.e., they remain the same strength and begin to propagate across shear. This process is illustrated in Fig. 1 — the initial tilting of the only-horizontal environmental vorticity by the updraft creates an area of cyclonic (anticyclonic) vorticity located on the southern (northern) flank of the cell, similar to observational findings from Browning (1964); Ray (1976), the latter using dual-Doppler analysis. As time progresses, evaporational cooling and precipitation drag strengthens the downdraft and forces the top of the vortex line arch down where the original updraft was. The downdraft splits the storm

in two, with two separate updrafts associated with the two new cells forming to the south and north of the downdraft — each storm is also associated with a new cyclonic / anticyclonic mesocyclone of its own due to the downward tilting of the vortex line. These processes modeled by Klemp and Wilhelmson (1978a,b) were later replicated in Rotunno (1981).

Linear theory of supercells to explain why a cyclonically-curved hodograph favors the cyclonic, or southern, supercell split was first put forth by Rotunno and Klemp (1981). Namely, linearizing the vertical vorticity (ζ) equation in terms of the shear vector, \mathbf{S} , and the vertical velocity, w , gives

$$\frac{d\zeta}{dt} = \mathbf{k} \cdot (\mathbf{S} \times \nabla_h w) \quad (1)$$

which physically means that for an updraft where $\nabla_h w$ points radially inward, positive (negative) ζ will be generated to the right (left) of the shear vector. Additionally, the pressure term, π , is related to the shear vector by

$$\nabla^2 \pi = -2\mathbf{S} \cdot \nabla_h w \quad (2)$$

which, given the assumption that $-\pi \sim \nabla^2 \pi$, physically means there will be a relative high (low) upshear (downshear) of the updraft. These equations explain why the cyclonic split dominates in directionally-varying environmental shear, and is shown schematically in Fig. 2. In an environment in which the shear is purely linear (Fig. 2a), the shear vector always points in the same direction (westerly in the figure), such that there is a relative high (low) on the western (eastern) flank of the cell. In other

words, the dynamic pressure gradients fail to produce a favored region of vertical motion. In an environment where the wind veers from easterly at the surface to westerly aloft, the shear vector itself turns from southerly near the surface, westerly at mid-levels, and northerly aloft (Fig. 2b). Thus, the southern flank of the supercell has a relative high (low) at the surface (aloft) and vice versa on the northern flank. The dynamic vertical pressure gradients in this case provide enhanced upward motion on the southern flank of the cell and suppressing downward motion on the northern flank — therefore, when the cell splits in this case, the cyclonic or southern split is favored. Davies-Jones (1984) shows that when the cyclonic split travels across-shear, the vorticity vector and storm-relative winds align such that the storm ingests more streamwise rather than crosswise vorticity. Additionally, Rotunno and Klemp (1985) show that splitting and deviant motion are purely dynamical processes, i.e., they still occur in the absence of precipitation processes — however, the strength of low-level rotation is significantly reduced when ignoring thermodynamic effects.

The conceptual model of a supercell presented in Lemon and Doswell (1979) (Fig. 3) shows two different areas of near-surface outflow, the rear-flank downdraft (RFD) and forward-flank downdraft (FFD), with a bean shaped updraft where the two interact along the leading edge of the hook echo. The FFD contains the heaviest precipitation region and is located downshear of the updraft where most of the hydrometeors are ejected. As the supercell matures and the low-level mesocyclone (LLM) intensifies, the pressure minimum associated with the LLM produces an adverse pressure

gradient force (PGF) from aloft towards the surface — thus, some of the precipitation descends towards the opposite side of the updraft, resulting in a hook echo and the classic kidney bean shape of the supercell. The characteristics of both the RFD and FFD are key in tornadogenesis or tornadogenesis failure, but have yet to be completely understood.

1.2 Low-Level Rotation

1.2.1 Previous Studies

While studies noted previously have shown the mid-level mesocyclone to be a product of the tilting of environmental streamwise horizontal vorticity into the vertical, many of the same studies recognized that the same mechanism cannot be solely responsible for the generation of rotation closer to the ground, i.e., within the lowest kilometer, otherwise known as the LLM. Davies-Jones (1982a,b) proved that the eddies needed to transport ζ from the mid-level mesocyclone down to the surface were simply insufficient in strength. Numerical experiments in Rotunno and Klemp (1985) and Walko (1993) confirmed the inability of environmental vorticity alone to be the origination source of low-level rotation, as acceleration of vertical velocity and significant stretching and upward tilting of cyclonic ζ occurred above the surface. Thermal boundaries associated with the RFD and FFD provided a key source streamwise baroclinic vorticity for the updraft to ingest and could not be neglected (Klemp and Rotunno, 1983; Rotunno and Klemp, 1985; Davies-Jones and Brooks, 1993).

More specifically, Klemp and Ray (1981) and Klemp and Rotunno (1983) simulated the 20 May 1977 Del City, OK supercell — while the low-level vorticity was assessed to be partially a result of tilting of vorticity associated with environmental shear, a significant portion was derived from the solenoidally-generated horizontal vorticity along the outflow associated with the FFD. The transient downdrafts, which were dynamically driven as a result of a PGF towards the LLM, acted to enhance convergence and stretch / enhance the low-level vorticity. In a similar study, Rotunno and Klemp (1985) also agreed that while mid-level rotation attained similar strengths in both their precipitation and precipitation-free simulations, analysis of a material curve through the circulation theorem confirmed the presence of baroclinity at low-levels which was essential in producing a low-level (~ 250 -m AGL) maximum of ζ . Namely, cyclonic (positive) vorticity was generated as parcels descend within the downdrafts, both on the left flank and upstream flank . Rotunno and Klemp (1985) was also the first study to correctly state that the observed wall cloud is simply a result of the updraft ingesting cooler, more saturated air from the cool side of the baroclinic zones.

Davies-Jones and Brooks (1993) assessed the sources of vorticity for the LLM by separating into its two components: barotropic and baroclinic. This is beneficial as barotropic vorticity acts as a material curve, i.e., the curve can distort and reorient, but cannot break — thus, at the beginning of the simulation, t_0 , all of the vorticity must be barotropic since thermal gradients have not been introduced. Further into the

simulation at time $t_0 + \Delta t$, the magnitude and the direction of the baroclinic vorticity can be recovered from tracking the barotropic vorticity at each point in time, such that the baroclinic term is simply the difference between the total vorticity and the barotropic vorticity. They found similar results as Klemp and Rotunno (1983) and Rotunno and Klemp (1985) — namely, originally negative ζ above 250 m flipped sign as parcels descended in the downdraft, where it was ingested into the updraft at about 100 m AGL and stretched further. Additional studies that confirmed the importance of baroclinic zones for low-level rotation include Walko (1993) and Wicker and Wilhelmson (1995). These previous findings were summarized by Davies-Jones et al. (2001), who also noted that there is a balance between solenoidally-generated vorticity along the thermal gradients and the speed of the flow. Namely, if the flow is exceedingly fast, then the amount of time the parcels spend in the baroclinic zone may not be sufficient for them to attain sufficient horizontal vorticity to generate a LLM, even after it is tilted and subsequently stretched by the updraft. On the other hand, storm-relative flow that is too slow may not be able to restrain the advancing of the cold pool such that the inflow / updraft gets undercut. Lastly, Davies-Jones et al. (2001) recognized the absence of data within the lowest few hundred meters above the surface which likely contains key information about tornadogenesis processes.

There have been several studies within the 1980s, 1990s, and 2000s that have attempted to use observational methods to confirm the importance of baroclinity in producing low-level rotation. Brandes (1984) used a dual-Doppler analysis in con-

junction with thermodynamic retrievals and concluded that baroclinic generation may not be essential for mesocyclone intensification or for tornadogenesis, but cautioned disregarding this mechanism altogether due to uncertainties in the retrieved buoyancy fields. Dowell and Bluestein (1997) also performed a dual-Doppler synthesis of the 1981 tornadic supercell in Arcadia, Oklahoma — although direct calculations of baroclinic vorticity generation were not made, horizontal vorticity just upstream of the updraft was found to be much larger than ambient vorticity, indicating storm-modifications must be playing a role, likely either via stretching and / or baroclinic generation. Dowell and Bluestein (2002b) also hypothesized that weak baroclinity in the storm likely modified the low-level horizontal vorticity around the LLM calculated via pseudo-dual-Doppler analysis, but again lacked the evidence via direct thermodynamic observations to support this hypothesis.

A more recent dual-Doppler study by Markowski et al. (2008) examined vortex lines within six supercell thunderstorms. It was found that while some vortex lines originated from the ambient environment and extended up towards the top of the supercell (mid-level mesocyclone), vortex lines associated with the LLM tended to arch, with the cyclonic side of the arch associated with the mesocyclone coupled with an anticyclonic region on the opposite flank of the hook echo, found in both tornadic and nontornadic supercells. The orientation of the arches differing from the orientation of vorticity associated with the ambient shear is strongly suggestive of the importance of baroclinic vorticity generation along thermal gradients, especially

along the RFD, and subsequent tilting by the updraft. These archs were also found in Straka et al. (2007). Last, Markowski et al. (2012) showed via circulation analysis that the circulation around the LLM is primarily baroclinically acquired along the forward-flank (FF) precipitation gradient characterized by a horizontal buoyancy gradient.

1.2.2 Importance of Internal Supercell Boundaries

Considering the hypothesized importance of internal thermodynamic boundaries within supercells in generating horizontal vorticity, it is not a surprise that there has been a concerted effort in obtaining direct measurements via in-situ observations. However, creating a consolidated conceptual idea of the FFD and RFD remains elusive, as different methods — in-situ, Doppler radar, and three-dimensional numerical cloud models — have resulted in varying characteristics of the FFD and RFD.

Earlier studies focused primarily on the characteristics of the RFD, as it was hypothesized that RFD properties were crucial in determining the evolution of tornadogenesis. Markowski et al. (2002) was one of the first to analyze collected surface thermodynamic observations within RFDs, collected during the VORTEX field campaign. It was found that tornado intensity, tornado longevity, and the likelihood of tornadogenesis increased as surface buoyancy, potential buoyancy (convective available potential energy, CAPE), and equivalent potential temperature increased, and as convective inhibition (CIN) decreased among parcels within the RFD. Interestingly, in contrast with previous thinking on baroclinic generation of vorticity, Markowski et al.

(2002) stated that baroclinity within the RFD is not a necessary condition for tornado-genesis. Results from Markowski (2002), which analyzed observations from supercells on 3 May 1999, were in general agreement with Markowski et al. (2002) — RFDs were found to have large CAPE, weak CIN, and overall small temperature deficits (i.e., weak baroclinity). Observations during Project Analysis of the Near-Surface Wind and Environment along the Rear-flank of Supercells (ANSWERS) delineated RFDs in nontornadic supercells, in opposition to tornadic supercells, as having colder equivalent potential and virtual potential temperatures; thermodynamic properties within the RFD regions of tornadic supercells differed only slightly from storm inflow characteristics (Grzych et al., 2007). Lastly, Hirth et al. (2008) sampled RFD properties in two different tornadic supercells and found varying characteristics: in the first supercell (weaker tornado), temperature deficits within the RFD were relatively strong and increased with time, while in the second supercell (stronger tornado), temperature deficits were much weaker, even with findings of positive potential temperature perturbations. Hirth et al. (2008) also found the thermodynamic properties within each individual RFD to be highly nonhomogeneous. From the noted studies, it is clear that if baroclinity is of significant importance in regards to providing a source of vorticity to the LLM, it is unlikely that the RFD plays the largest role, as stronger supercells and tornadoes are more likely associated with weaker baroclinity within the RFD.

Kinematically, Lee et al. (2012) found that RFD thermodynamic characteristics

are far from steady-state and are dependent on RFD internal surges (RFDISs), where the more negatively buoyant, cooler RFDISs were associated with the weakening of the tornado and more positively buoyant RFDISs were actually associated with significant tornado development. RFDISs were also observed in Skinner et al. (2014), and they are determined to be very important in lifting potentially negatively buoyant parcels to significant heights, and failure of RFDISs to do so may limit vertical accelerations and stretching of ζ — Kosiba et al. (2013) also determined the RFD is essential for providing convergence and stretching of ζ .

Of course, given numerical evidence of larger baroclinic generation within the FFD, many studies began to focus on analyzing thermodynamic characteristics within the FFD to see if thermal gradients were stronger in this region compared to the RFD. Shabbott and Markowski (2006) analyzed the FFD in 12 different supercells, some of which were tornadic and some of which were nontornadic, which were observed during the VORTEX field campaign. Similar to findings with the RFD, they determined that the FFD of nontornadic supercells were more negatively buoyant than that of tornadic supercells, with the best predictor of buoyancy magnitude being relative humidity / dewpoint depression within the inflow — along the same lines, baroclinic generation of streamwise vorticity along the FFD was interestingly larger in nontornadic supercells than in their tornadic counterparts. Skinner et al. (2011) analyzed mobile mesonet data from the 23 May 2007 Perryton, Texas, weakly tornadic supercell across both the RFD and FFD and found that within the RFD, large

deficits of both virtual potential temperature and equivalent potential temperature were prominent. On the other hand, thermodynamic variations within the FFD were small, similar to findings from Shabbott and Markowski (2006). However, Skinner et al. (2011) found parcels within the FFD downdraft could be characterized by both negative perturbations in virtual potential temperature and positive perturbations of equivalent potential temperature, which have the potential to provide both a source of greater buoyancy and baroclinically-generated streamwise vorticity into the LLM. Several other observational studies have downplayed baroclinity within the FFD, including Romine et al. (2008) which highlighted a warm FFD during the 8 May 2003 Oklahoma City tornadic supercell and Weiss et al. (2015) which showed the weakly tornadic phase actually contained larger θ_v gradients compared to the strongly tornadic phase, though the latter did show that there do exist zones of more intense baroclinic vorticity generation of $O(10^{-4})$ within the FFD.

Kinematically, various radar studies have also presented varying characteristics of the FFD. For example, Dowell and Bluestein (2002a) found subtle near-surface wind shifts north of the mesocyclone using psuedo-dual-Doppler analysis. On the other hand, Beck et al. (2006) failed to find any appreciable wind shift closer to the surface, but rather found a strongly convergent zone approximately 1 km AGL in a nontornadic supercell. Dual-Doppler radar analysis from Frame et al. (2009) not only showed minimal wind shift along the FFD as well, but trajectory analysis from the LLM could not be traced back to parcels along the FFD. However, none of these

studies adequately documented the lowest 250 m AGL which is almost certainly vital in modulating LLM strength.

In summary, observational studies, both from mobile mesonet and dual-Doppler analysis, have downplayed the importance of kinematic and thermodynamic variations along the RFD and FFD in the generation and maintenance of the LLM. This is in direct contrast to numerical studies from the 1980s and 1990s which have shown sharp buoyancy gradients (e.g., Klemp and Rotunno, 1983; Rotunno and Klemp, 1985; Wicker and Wilhelmson, 1995; Adlerman et al., 1999) and wind shifts / convergence zones along the FFD (Rotunno and Klemp, 1985; Wicker and Wilhelmson, 1995; Adlerman et al., 1999) are important contributors to LLM strength. This does not necessarily imply that sharper kinematic and thermodynamic boundaries do not exist, but that perhaps the observational data lacked the spatial and temporal fidelity to properly sample these features that exist in supercell flows.

1.2.3 Recent Studies: The Streamwise Vorticity Current

Within the last decade, continued investigation of the importance of internal boundaries has been prominent within the literature, both through an observational and numerical lens. For example, Beck and Weiss (2013) employed varying microphysics when simulating a supercell using the Weather Research and Forecasting (WRF) model, and found that although the position and strength of the cold pool varied with parameterization, the overall evolution of the boundaries were relatively similar.

Beck and Weiss (2013) outlined a conceptual model of supercell boundary evolution in which the rear-flank gust front develops first, followed by the FF boundary which undergoes balancing of inflow versus outflow before becoming steady-state. The third boundary extending northeast from the LLM develops last, and is produced from evaporative cooling of inflow air. Although all three are denoted as boundaries, only the first is classified as a “gust front” by Beck and Weiss (2013), as this boundary is the only one marked by significant collocated wind shifts and pressure gradients. Nevertheless, trajectory analysis shows parcels associated with the boundaries to the north of the mesocyclone are significant in the production of low-level vorticity, though parcels along the RFD still provide the majority of ζ through tilting of baroclinically-generated horizontal vorticity.

Dahl et al. (2014) was the first to coin the term “vorticity river” or “streamwise vorticity current” (SVC), an area of baroclinically-generated streamwise vorticity just on the cool side of the FFD which continuously feeds ζ into the LLM. Similar to Davies-Jones and Brooks (1993), Dahl et al. (2014) used a Lagrangian technique in order to decompose the vorticity terms into barotropic and baroclinic, the latter of which is simply the barotropic component subtracted from the total vorticity. Through trajectory analysis from parcels that attained significant values of low-level ζ , the study concluded that the “rivers” of vorticity were a result of primarily baroclinic production along the base of downdrafts. This baroclinic horizontal vorticity was tilted downward as it was advected closer to the LLM, with the “tails” of the

vorticity vector descending faster than the “tips”, thus producing positive ζ . On the other hand, barotropic vorticity, though remaining streamwise, did not attain a respectable vertical component as it descended towards the ground — this agrees well with previous studies, in that near-surface ambient vorticity does not solely determine the strength of the LLM. Dahl (2015) confirms that the baroclinic mechanism dominates over barotropic generation through upward tilting, and that this result is independent of microphysics parameterization.

To investigate the role of downdrafts within supercells further, Markowski and Richardson (2014) initialized an idealized, dry simulation with environmental wind shear and introduced a heat source (updraft) such that ζ was generated only through tilting of ambient vorticity. Once steady-state was reached, a heat sink, whose strength was varied along with environmental shear, was introduced to represent a downdraft on the northeastern flank of the updraft at low levels. The LLM was most intense in the simulations where ambient low-level shear was strong and the strength of the cold pool was moderate. This is representative of the “Goldilocks” problem, as the simulations in which the cold pool was too strong or weak (or when the low-level shear was weak) failed to form an intense LLM. Markowski and Richardson (2014) hypothesized that moderately-strong cold pools still generated substantial amounts of baroclinic vorticity near the circulation, while strong environmental low-level shear lowered the base of the mid-level mesocyclone, aiding to dynamically force circulation-rich near-surface air close to the heat sink upwards. In a similar man-

ner, Parker and Dahl (2015) initialized a heat-sink with varying degrees of low-level storm-relative flow, and found that ζ near the surface was generated baroclinically as parcels descended within the heat sink, and that this process occurs in all cases except for when the downdraft-relative flow is zero.

Similarly, Markowski et al. (2014) analyzed ζ sheets within an idealized supercell and found that ζ in the lowest 5 m only existed within the vorticity sheet if the tilting of vorticity occurred within a descending airstream — no ζ below 5 m AGL existed through tilting associated with an ascending airstream. This is consistent with prior work that downdrafts are essential in providing ζ very close to the surface. In a follow-up study, Markowski and Richardson (2017) held the ambient shear and the strength of the heat sink constant and varied the location of the heat sink. Though it was found that the location of the heat sink does play a large role in the intensity of the LLM, the changes are difficult to predict as these processes are highly nonlinear. This illustrates the difficulty in predicting supercell behavior, and shows why supercells may fail to become tornadic in seemingly favorable tornadic environments.

Orf et al. (2017) used the 1977 Del City supercell environment (Klemp et al., 1981) within a CM1 framework employing 30-m grid spacing with a free-slip lower boundary and advanced visualization techniques to develop a new framework of low-level ζ generation. The simulation produced a tornado that lasted 2 h including a consecutive 38 min period in which the tornado was rated at an “EF-5” strength based on the wind speed. Consistent with previous studies, Orf et al. (2017) noted an

SVC along the FFDB that was collocated with vorticity patches that were advected inwards towards the LLM and subsequently tilted upwards — the location in which tilting occurred was collocated with the tornado, the development of which was in conjunction with strengthening of the LLM (Figure 4). The tornado continued to ingest pockets of cyclonic ζ from the FFDB and maintained its strength until the tornado moved rearward into the cold pool and subsequently dissipated, occurring in conjunction with SVC weakening.

While a plethora of studies have outlined the unmistakable role of downdrafts in producing baroclinically-generated vorticity, there is some debate on whether or not friction plays an essential role — the idea is that since flow at the surface must tend to zero, very-near surface horizontal vorticity must be generated through frictional mechanisms which can then be tilted and stretched. While some of the previous studies mentioned neglected surface friction and still found appreciable vorticity generation (e.g., Dahl, 2015), with Parker and Dahl (2015) directly finding no significant difference between simulations with and without surface friction, other studies have found that surface friction plays a larger role. Schenkman et al. (2014) ran simulations both with and without surface drag and found the results between the two differed significantly — the tornado in the no-drag simulation was shorter-lived and took a different path than the drag simulation. Additionally, trajectory analysis with parcels near the base of the downdraft showed a significant portion of their vorticity is attained through horizontal frictional torque processes near the ground. Additionally,

Roberts et al. (2016) runs two simulated supercells using the 3 May 1999 Oklahoma case in a CM1 framework, the first of which surface drag is applied to the full wind and the second where surface drag is applied only to the background environmental wind; the former developed a 10+ min tornado 25 min into the simulation while the latter failed to produce a tornado at all. Roberts et al. (2016) identified three mechanisms in which friction enhances tornadogenesis likelihood: 1) creation of background low-level vertical wind shear (and horizontal vorticity) by near-surface drag, 2) generation of storm-scale near-ground crosswise horizontal vorticity that is transferred into the streamwise direction and tilted, and 3) enhancement of horizontal convergence, increasing both stretching of low-level ζ and the low-level updraft.

Not surprisingly, recent observational studies have attempted to attain confirmation of SVC-like features in observed supercells through various methods. Namely, Markowski et al. (2018) noted a consistent, enhanced band of streamwise vorticity in the general region where Orf et al. (2017) noted the SVC, with intensification of the band coincident with the time leading up to tornadogenesis. Additionally, Murdzek et al. (2020b) hypothesized that failure of streamwise vorticity rich parcels within the FF to reach the LLM, OW minimum, or updraft pulse contributed to tornadogenesis failure in their 26 May 2010 Colorado supercell case study. A deeper dive into that case along with two other supercells in Murdzek et al. (2020a) found that two of the three observed supercells contain a feature similar to numerical SVCs — however, the one without an SVC still produced a brief, weak tornado, so it is noted

that investigation on the true role of SVCs on tornadogenesis is warranted. Schueth et al. (2021) noted stronger values of horizontal vorticity along steady-state Kelvin-Helmholtz billows via range-height indicator scans from the Texas Tech University Ka-band mobile radars — these billows were also found in their simulation of a tornadic supercell, with stretching of streamwise vorticity being the dominant generator over baroclinic mechanisms. Last, Bartos et al. (2022) analyzed swarmsondes and found that LLM parcel paths can be traced back to FF regions including through buoyancy gradients that are strongest in the lowest 750 m.

1.3 Research Goals

Given previous research, there still exists a gap between observational findings which have tended to downplay the importance of baroclinic boundaries (especially within the FFD) versus numerical simulations which have highlighted the importance of baroclinic generation of streamwise vorticity and the SVC. Additionally, while dual- or multi-Doppler studies of supercells are not new, studies that contain longer periods of analysis, especially analysis through multiple periods of supercell weakening / strengthening, are much less common — the rarity gets exacerbated when considering the availability of wind syntheses in conjunction with thermodynamic measurements, whether by direct measurement or thermodynamic retrieval methods.

The study presented herein aims to bridge these gaps by presenting an analysis of a cyclic, tornadic supercell observed by the Targeted Observation by Radars and UAS

of Supercells (TORUS) field campaign on 17 May 2019. The 99 min uninterrupted period of the multi-Doppler analysis through multiple periods of supercell weakening and reorganization (including the presence of 9 separate tornadoes) makes this observational dataset novel. The multi-Doppler analysis ingests data from three separate radars including two airborne radars and one rapid scanning ground-based radar, the latter of which allows for improved coverage of near-surface wind data. The study also presents full 3D thermodynamic data including buoyancy and hydrometeor mixing ratio information through the entire analysis period using a diabatic Lagrangian analysis approach (Ziegler, 2013a,b), adding to the novelty of the dataset. Because of the availability of both 3D kinematic and thermodynamic data at all times, the dataset provides the ability to answer some important research questions, including:

1. What is the evolution of the LLM through multiple cyclic periods, and does its strength (quantified via updraft and circulation parameters) correlate well with observed tornadic / nontornadic periods?
2. How does the structure (including baroclinic gradients) of the FFD and RFD change as the supercell oscillates in strength, and how do structure changes relate to observed periods of strengthening / weakening?
3. Does the supercell contain an observed SVC, and if so, how does the evolution of the SVC relate to tornadogenesis likelihood?
4. Given that the supercell produced 9 separate tornadoes of varying degrees of

strength and longevity during the analysis period, can we correlate differences in vortex behavior (e.g., longevity and structure) to patterns in LLM characteristics?

2 Chapter 2: Analysis of 4D Kinematic Fields Retrieved via Multi-Doppler Analysis Techniques

2.1 Introduction

To bridge the gap between supercell findings in numerical and observational studies, the Targeted Observations by Radar and UAS of Supercells (TORUS) field experiment is aimed at sampling supercells within the Great Plains. This study presents analyses of the 17 May 2019 tornadic supercell in southwest NE that was observed by TORUS. In this chapter specifically, the analyses combines data from the aft and fore radars from the airborne P3 radar (Jorgensen et al., 1983) and the ground-based National Severe Storms Laboratory’s dual-polarized X-band mobile radar NOAA X-POL (NOXP) radar for a triple-Doppler wind synthesis. Because the analysis spans a 99 min period, this study hallmarks one of the most detailed, uninterrupted documentations of supercell evolution, especially in regards to the temporal evolution of 3D wind fields. To our knowledge, it is the first to detail supercell evolution including numerous significantly tornadic periods and a cycling period in between — this includes low-level vortex behavior and evolution. From the wind syntheses, we aim to 1) identify the evolution of the low-level mesocyclone (LLM) and vortex structure as the supercell underwent cyclic processes and 2) characterize the various flow regimes that were observed during the analysis period (including through investigation of backward trajectories) and correlate these flows back to LLM strength and

organization patterns.

2.2 Data and Methods

Retrieval of 4D kinematic data utilized three radars that successfully deployed on the tornadic supercell: the ground-based NOXP radar and the two airborne radars on the P3 (fore and aft radar). The NOXP and P3 operating specifications for 17 May 2019 are shown in Table 1 and 2, respectively. NOXP completed a full volumetric scan approximately every 3 minutes with maximum elevation angle of 20° from 22:57 to 23:21 UTC — after 23:21 UTC, the scanning strategy was modified giving a maximum elevation angle of 30° from 23:21 to 00:39 UTC. For both strategies, the lowest two elevation angles (0.5° and 1.0°) were revisited within a volume scan to obtain higher temporal resolution in the lower portions of the storm.

Two Doppler radars were mounted onto the tail of the aircraft that scanned synchronously at 20° from zenith in opposing directions, one towards the front of the aircraft (fore radar) and one towards the back (aft radar). As the aircraft moved forward straight and level, these angles guaranteed the fore and aft radars were within a dual-Doppler lobe. Regular transects at offset distances of 10–15 km ahead of the storms allowed for dual-Doppler measurements of the supercell’s evolution. The radars completed one sweep every ~ 3 seconds — coupled with a forward motion of approximately 100 m s^{-1} , this gives a horizontal spatial resolution of about 300 m. Additionally, given the P3’s beam width of 2° , the vertical grid spacing below 1 km

AGL within the supercell regions furthest from the plane is on the order of 300–400 m — the supercell regions closest to the plane have vertical grid spacing on the order of 100–200 m. Therefore, the coarsest resolution (Δ_{max}) is defined by the P3 radars. Times of each of the 12 transects or leg of the P3 is given in Table 3, where a transect is defined as a section of the flight path during which the aircraft was not engaging in a turn-around maneuver and the radars were actively scanning the storm of interest directly to the right or left of the aircraft.

2.2.1 Quality Control

Prior to any analysis, each sweep from the NOXP and P3 radars were first run through quality control (QC) using an automated PyART script (Helmus and Collins, 2016). For NOXP, the QC process included removal of ground clutter using gates of spectrum width less than 1 m s^{-1} combined with radial velocity magnitude of less than 1 m s^{-1} , clear air noise filtering, and despeckling, as well as rotation correction for mobile radar orientation relative to true north (Wurman and Gill, 2000; Ziegler et al., 2004). Additionally, because the Nyquist velocity of the NOXP radar is 19.14 m s^{-1} , the velocity field is objectively dealiased using the four-dimensional Doppler dealiasing (4DD) algorithm with an input environmental sounding (James and Houze, 2001) — the chosen input sounding is taken from a far-field sounding released from one of the TORUS vehicles at 23:02:20 UTC (Fig. 5). After objective dealiasing, each sweep was manually analyzed to correct any areas which needed further QC — the main

areas in which this was necessary was in the hook echo region and at higher elevations where velocities were double- or triple-folded.

Every P3 sweep was also run through the same QC script with slightly different options. First, aircraft motion was subtracted from the velocity data and ground echoes were objectively removed in NCAR’s solo polar radar viewer and editor (SOLO3) software. Then, the data was run through the QC script with spoke removal, masking of remaining ground echoes, noise filtering, and correction of dual-PRF processing errors. Because the P3 radar scanned with a dual-PRF ratio of 3:2, this resulted in a Nyquist velocity of 44.4 m s^{-1} . This Nyquist velocity is large enough such that it was determined through visual inspection that automated dealiasing was not a necessary procedure for the two P3 radars — while there were aliased areas near the top of the storm where divergence was strong, these were manually identified and corrected. Lastly, while the QC script was sufficient in cleaning up a vast majority of the data, it was found to be too aggressive in removal of ground echoes within the lowest 2–3 beams above the ground leading to removal of non-ground clutter near-surface echoes. Since reflectivity and velocity data near the ground are essential in capturing low-level processes, these data were manually recovered for all sweeps.

For mobile mesonets (MMs), data was recorded at a nominal spacing of 1 Hz with temperature, relative humidity, and wind sensors calibrated by the Oklahoma Climate Survey (OCS) before deployment. Additionally, wind observations were automatically corrected for vehicle motion. All data were objectively QC’ed during post-processing

and data that are not suitable to be used in the analysis were automatically flagged based on several possible reasons: 1) panel temperature on the data logger changed by a significantly large amount potentially due to voltage issues or radio interference, 2) the vehicle was stationary causing potential biases in insufficient ventilation, 3) vehicle was accelerating (in speed or direction) which may lead to inaccurate derived winds, and 4) any recorded variables (e.g., latitude, longitude, GPS time) fell outside of a normal operating range. Out of the 3404 MM observations that were taken from 23:36 UTC (MM first enters FF region) to 00:33 UTC (MM exits supercell to the NW), 405 observations were flagged as not suitable for research, i.e., $\sim 88.1\%$ of the MM observations are used for the analysis.

2.2.2 Objective Analysis and Wind Syntheses

Because full NOXP volume scans were spaced every 3 minutes, and individual radar volumes from both the NOXP and P3 were not synchronized, a spatiotemporal correction of radar volumes was required before objective analysis (OBAN) could be performed. For an analysis time t_a , the corresponding volumes just before and after the analysis time (t_1 and t_2) were spatially advected to t_a based on the constant storm motion vector $u_{storm} = 8.5 \text{ m s}^{-1}$ and $v_{storm} = 9.6 \text{ m s}^{-1}$. Because there was a time difference between each ray within each PPI scan, each individual ray within the volume scan was temporally corrected based on the time that the data within that ray was collected. Last, the two resulting analyses that were advected linearly in

time were then averaged in a time-weighted sense to produce a “corrected” analysis at the intermediate t_a (Fig. 6) — this is hereafter referred to as the time-morphing algorithm and is analogous to advection correction.

After the data were QC’ed and the volumes were spatiotemporally corrected to each analysis time, the data were then objectively analyzed onto a $0.25 \times 0.25 \times 0.25$ km Cartesian grid using a 1-pass Barnes analysis. After testing, it was determined that, given the size of the storm and greater peak ranges of data gates from various radars, that a 2-pass Barnes analysis did not provide further value than a 1-pass Barnes analysis. The grid spacing of 250 m was chosen to be of the same order with the horizontal spacing of the P3 radar, $\Delta_{max} = 300$ m. The lower-left corner of the grid was chosen to be about 60 km to the southwest of the hook echo at 22:57 UTC and the upper-right corner was chosen to be to the northeast corner of the supercell at 00:36 UTC, such that the supercell moves through the fixed domain rather than implementing a moving grid that translates with the supercell. While this was less efficient in terms of file storage due to the need for a larger horizontal domain (125×135 km) to account for the approximate northeast motion of the supercell, the stationary grid makes backward trajectory calculations for the diabatic Lagrangian algorithm (DLA) much simpler (DLA details in Chapter 3.2.1). The filtering parameter of $\kappa = (1.33\Delta_{max})^2$ is consistent with Pauley and Wu (1990) such the OBAN retains only 50% of the minimum resolvable wavelength of Δ_{max} but retains >80% for wavelengths of $>3\Delta_{max}$. Because the lowest grid point in the

OBAN is at the surface (below the lowest beam height), the data points from the lowest radar beams had to be extrapolated downwards. For example, if the data at the surface is missing and the wind speed at 250 m and 500 m is 10 m s^{-1} and 15 m s^{-1} , respectively, this would extrapolate as a 5 m s^{-1} surface wind speed at that grid point. This method will be compared to MM observations in Chapter 2.6 to determine the accuracy of extrapolation to the surface from vertically adjacent grid points.

The 3D wind field at each time was synthesized from the OBAN Doppler radial velocities. Because there are radial velocities from three radars, an overdetermined dual-Doppler analysis algorithm composed of normal linear equations is solved for u , v , and vertical velocity (w) components which were iteratively solved via vertical integration of the anelastic mass continuity equation (Ray et al., 1980; Ray and Sangren, 1983; Kessinger et al., 1987). Namely, Eqs. (A2-A4) from Kessinger et al. (1987) detail the equations to be solved, but are repeated below for completeness:

$$u = \frac{S_{yy} \sum [R_i V_i (x - x_i)] - S_{xy} [\sum R_i V_i (y - y_i)] + (w + V_t)(S_{xy} S_{yz} - S_{yy} S_{xz})}{S_{xx} S_{yy} - (S_{xy})^2} \quad (3)$$

$$v = \frac{S_{xx} \sum [R_i V_i (y - y_i)] - S_{xy} \sum [R_i V_i (x - x_i)] + (w + V_t)(S_{xy} S_{xz} - S_{xx} S_{yz})}{S_{xx} S_{yy} - (S_{xy})^2} \quad (4)$$

where V_i is the radial velocity observed at range R_i and V_t is the terminal fall speed estimated from radar reflectivity given by Joss and Waldvogel (1970) — while the terminal fall speed relationship is for S-band radars, it is shown to give accurate DLA retrievals in Ziegler (2013b) for mobile X- and C-band radars. The least squares

equation is given by

$$S_{xy} = \sum (x - x_i)(y - y_i) \quad (5)$$

and similarly for S_{xx} , S_{yy} , S_{xz} , and S_{yz} . Once the horizontal components of velocity were solved, w was derived through each vertical grid column via downward integration. The anelastic mass continuity is defined as

$$\frac{\partial u}{\partial x} + \frac{\partial v}{\partial y} + \frac{\partial w}{\partial z} - \kappa w = 0 \quad (6)$$

where κ is the logarithmic change in density with height.

Downward integration was chosen over upward integration due to theoretical arguments that error propagation is lesser with downward integration given stratification in atmospheric density (Ray et al., 1980). In equation form, vertical velocity is given by

$$w(k - \frac{1}{2}) = \left(\frac{1/\Delta z - \kappa/2}{1/\Delta z + \kappa/2}\right)w(k + \frac{1}{2}) - \frac{(u_{i+1,j} - u_{i-1,j})_k}{2\Delta x(1/\Delta z + \kappa/2)} - \frac{(v_{i,j+1} - v_{i,j-1})_k}{2\Delta y(1/\Delta z + \kappa/2)} \quad (7)$$

where i , j , k , are indices denoting horizontal and vertical grid indices. Note that the last two terms in Eq. 7 represent derivatives that are approximated by centered differences. After integration, a velocity hole-filling technique was used to fill grid points with missing data. Additionally, an O'Brien column w-adjustment was performed to reduce vertical velocity errors within a column. A 3D variational adjustment via a strong integral constraint with upper and lower boundary conditions of $w = 0$ was also implemented such that the anelastic mass continuity equation was exactly satisfied. Finally, the analysis at the edge of the storm region (demarcated by reflectivity

less than 20 dBZ) was blended with the ambient winds determined from the environmental sounding — this was done via a horizontal nine-point elliptic low-pass spatial filter which produces a gradual, smoothed transition of wind velocities from ambient to storm environment.

In order to capture the evolution of the ambient environment during the 99 min analysis period, the sounding used at each analysis time was obtained by linearly interpolating between two TORUS soundings, the first recorded on 17 May 23:02:30 UTC and the second on 18 May 00:57:05 UTC. Namely, the first sounding is a far-field sounding while the second sounding is a near-field sounding with the locations shown in Fig. 7a and 7b, respectively. Because the analysis domain extends to 16 km, and the 23:02:30 UTC sounding terminated at 13.5 km, the sounding from 13.5 km to 16 km was filled in with the 00:00 UTC KDDC sounding (data from the spatially closer 00:00 UTC KLBF sounding was not available above 13.5 km). The transition between the 23:02:30 TORUS sounding and the 00:00 UTC KDDC sounding was smoothed to eliminate the discontinuous jump from blending the TORUS and KDDC sounding; the full sounding used is shown in Fig. 7c. The 00:57:05 UTC sounding extended to 8.1 km; above that, the 23:02:30 UTC sounding (including the portion filled in by the 00:00 UTC KDDC sounding) was used to fill and the transition was smoothed again.

Each sounding was then interpolated to a $\Delta z = 0.25$ km vertical resolution grid from the surface to 16 km to match the analysis grid. Once each sounding was on

the $\Delta z = 0.25$ km grid, the sounding at each analysis time was obtained by linearly interpolating in time between the 23:02:30 and 00:57:05 UTC soundings. Note that because the first two analysis times, 22:57 and 23:00 UTC, were before the 23:02:30 UTC sounding, these two soundings were obtained via linear *extrapolation* rather than interpolation. Allowing for temporal evolution of the sounding allows for more accurate capturing of boundary layer (BL) evolution during the 99 min of the analysis period; namely, from 22:57 UTC to 00:36 UTC, surface θ decreased from 306.8 K to 304.6 K and surface q_v increased from 12.87 g kg⁻¹ to 13.71 g kg⁻¹ leading to higher θ_v values and a lower LCL by the end of the period (Fig. 8). Additionally, a dry layer just above the LFC is moistened within this time frame. While thermodynamic evolution only becomes important for the DLA in Chapter 3, kinematically, winds within the BL strengthened and backed in direction which affects wind syntheses presented here in Chapter 2.

2.3 Event Overview

The first detection of a deep convective echo (reflectivity > 30 dBZ) associated with the supercell of interest occurred near Goodland, KS at around 20:00 UTC. While the storm attained mid-level rotation soon after first echo, it continued to remain nontornadic and track northeast for a few hours. The supercell then underwent a cyclic, active tornadic period for several hours starting from 22:40 UTC in which it produced a total of 13 tornadoes from south of Culbertson, NE to 20 miles northeast

of Cozad, NE (9 of the 13 tornadoes occur within the analysis period). Fig. 9 shows all of the damage indicators (DIs) associated with all tornadoes produced with the radar images corresponding to the approximate beginning and end of the analysis period — one tornado prior to McCook, NE and the three tornadoes near and NE of Cozad were the four tornadoes not captured within the analysis. Beyond the DIs in Fig. 9, the supercell remained nontornadic, although it persisted for several more hours before merging with the lagging QLCS. In total, from first deep convective echo to QLCS merging, the supercell lasted an impressive 7 hours, alluding to the relative isolation of the supercell ahead of the QLCS and from surrounding convection.

Because the 99 min analysis period is relatively long, it is helpful to break it up into three different, smaller segments that will be used as demarcation points within this Chapter. The details of the three segments are detailed below, and the details of all the tornadoes within the analysis period can be found in Table 4:

1. Segment 1 (S1), which runs from 22:57 to 23:06 UTC, is the first significant tornadic period, marked by one significant but short-lived EF2 tornado to the east of McCook, NE.
2. Segment 2 (S2), which runs from 23:06 to 23:57 UTC, is the weakly tornadic period. While four separate tornadoes officially occurred in this 48 minute time frame, all were given an EF-0 rating and three of the four had a path length of half a mile or less. The radar presentation of the supercell and mesocyclone during this period was less organized in comparison to S1 or S3.

3. Segment 3 (S3) runs from 23:57 to 00:36 UTC and is denoted as the second significant tornadic period. Unlike S1, S3 contains four separate tornadoes, three of which were EF-1+ and two of which were significant. The presentation of the supercell and mesocyclone are the most impressive during this time, and the strongest tornado (per the EF-scale) that the supercell produced (EF-3) occurred in S3 from 00:05 – 00:09 UTC. S3 also contains the longest-lived tornado, an EF-1 lasting 18 minutes from 00:15 to 00:33 UTC.

The following results in this chapter will focus on key kinematic features found within the 4D wind synthesis during the analysis period, highlighting differences found between S1, S2, and S3. Because full 3D wind vectors are available at each analysis time, derived fields such as convergence / divergence, vorticity, etc can be calculated. It is worthwhile to reiterate that while these sorts of calculations have been done previously within a dual- or multi-Doppler framework, the length of uninterrupted analyses presented herein is novel, and allows for detailed analysis of the *evolution* of key features during the transition from a strongly tornadic period to a weakly tornadic period, and back again to a strongly tornadic period of the supercell.

The time series of 1 km w (w_{1km}) and surface Okubo-Weiss number (OW) distributions (Okubo, 1970; Weiss, 1991) are given in Fig. 10 and 11, which give a measure of low-level updraft strength and near-ground rotation. Distributions are taken from within 5 km of the center of rotation at a given height, where the center is manually identified at each analysis time — also note that only positive values of

w_{1km} and negative OW are included in the distribution since the focus is to capture time evolution of LLM updraft and resolved rotational properties. w_{1km} is directly related to LLM strength and vertical vorticity (ζ) stretching potential while OW is mathematically defined as

$$OW = D^2 - \zeta^2 \quad (8)$$

where D is the total deformation (Okubo, 1970; Weiss, 1991; Markowski et al., 2011). OW is helpful in the fact that it discriminates areas of ζ owing to regions of rotation (OW minima) and deformation (OW maxima). Thus, Fig. 11, which is a time series of the *negative* of the OW field, is a quantification of near-surface rotation around the LLM with time, with higher values indicating stronger rotation.

Fig. 10 illustrates that while there is not much variability in the median of the w_{1km} distribution around the LLM, more extreme values ($\geq 95^{th}$ percentile) exhibit larger temporal fluctuations that correlate well with the supercell segments (S1, S2, and S3). The patterns are especially obvious when examining the maximum w_{1km} value within the distributions indicated by the top of the violin plots. Namely, maximum w_{1km} within S1 starts off quite high near 25 m s^{-1} before decreasing by the end of S1, relating to the dissipation of the EF-2 tornado. The global minimum of w_{1km} is found within S1 at around 23:27–23:30 UTC before beginning to ramp back up especially after 23:45 UTC as the supercell begins to reorganize. The strongest w_{1km} values are found within S3, the most active and significant tornadic period, with 10 of the 13 analysis times having maximum $w_{1km} \geq 20 \text{ m s}^{-1}$ (found in only 3 analysis

times prior to S3).

The patterns within the -OW distributions are perhaps even more well-correlated with the supercell behavior, with a local maximum at the start of the analysis period associated with the ongoing EF-2 tornado (Fig. 11). There is a relative dip before another local maximum at 23:15 UTC perhaps associated with tornado #2 (EF-0; see Table 4) and one at 23:36 UTC coincident with tornado #3 (also EF-0). In between these two maxima is a minimum at 23:27–23:30 UTC which corresponds precisely with the global minimum in w_{1km} — thus, regarding low-level organization, the supercell is likely at maximum disorganization around this time. While there is no -OW maximum with tornado #4 (EF-0), it is possible that this tornado is too short-lived or is too small to be captured by the temporal and / or spatial resolution of the analysis. Nevertheless, the beginning of S3 is marked by a steep increase in -OW where it remains for the rest of the period, signifying the relative robustness of the near-surface rotation during S3. In fact, the minimum value of both the 95th percentile and the maximum of -OW within S3 is larger than the highest value at any time within S1 and S2. Given the trends in Fig. 10 and 11 and how well they correlate with tornadic activity within the supercell, we are confident the wind syntheses are producing low-level near-mesocyclone velocity fields that are evolving consistently with observed tornado occurrences.

2.4 Kinematic Analysis

2.4.1 Segment 1

Segment 1, which includes times between 22:57 to 23:06 UTC, is the shortest of all the segments and is characterized by a short-lived, but significant, EF-2 tornado that was officially on the ground from 22:55 to 23:01 UTC. Surface analyses from S1 show a well-defined hook echo collocated with a robust area of rotation until 23:03 UTC. The area of rotation is elongated from southeast to northwest, also identifiable by the elliptical contours of negative surface OW highlighting the near-surface rotation (Fig. 12a-c) — we note that “rotation” herein refers to regions that have closed, cyclonic flow characteristics that are resolved within the wind syntheses. The actual track of the tornado (indicated by the DIs) is located on the southeast periphery of the negative OW contour. It is important to note that although Fig 12 is a “surface” analysis, because of beam height curvature issues with NOXP and ground-clutter with P3, radar data below 250 m is, for the most part, unavailable — recall that within the OBAN, this is resolved through extrapolation from the nearest vertical grid levels above the surface. Therefore, the surface analyses are likely to be reflective of a combination between the surface truth and the data just above the surface. Additionally, owing to 250 m grid spacing, it is difficult to fully resolve the tornado cyclone within the analysis. Regardless, the DIs being displaced to the southeast from the minimum in surface OW suggests the tornadic cyclone is tilted / displaced from the LLM. Additional evidence for this conjecture is found when examining the 1 km

AGL analysis in S1 (Fig. 13a–c) — namely, the minimum in the OW fields at 1 km are located to the northwest of the surface OW minimums, especially obvious at 22:57 and 23:03 UTC. Visual observations confirm extensive tilt of the tornado especially towards the dissipation stage, with the base of the condensation funnel far displaced from attachment to cloud base (Fig. 14, video screenshots credit of “TheF5Hunter”).

The dissipation of the tornado officially occurs at 23:01 UTC and is reflected through a significant change between the 23:03 and 23:06 UTC analysis. Fig. 12c to d shows a transition to a more outflow-dominant hook echo structure, with weak flow passing through the reflectivity appendage and a loss of any stronger rotation. This is in conjunction with an absence of any strong minima in the OW field at the surface. Fig. 13d shows that the LLM had undergone a kinematic occlusion process displacing it towards the backside of the storm with the center located at around $x = 42.5$ km and $y = 48.5$ km, several kilometers to the west of the hook echo. Within the hook itself, the flow is again passing through the reflectivity associated with the appendage from southwest to northeast, and although there is a new stronger minimum in OW at 1 km within the inflow notch, this is not associated with any strong rotation near the surface. After 22:57 UTC, blue contours in Fig. 13 show 1 km AGL vertical velocities are relatively weak above the surface OW minimum, which indicates stretching of near-ground vertical vorticity was likely not enough to maintain tornadic strength for very long, leading to the short-lived nature of tornado #1.

Even where 1 km vertical velocities are stronger at 22:57 UTC, these updrafts

are displaced from both the OW minimum and ζ maximum to the south, leading to the conclusion that stretching of near-ground ζ is not playing a role in maintaining the tornadic rotation at resolved scales. Investigating further reveals a potentially interesting tornadogenesis / maintenance mechanism associated with tornado #1. Fig. 15a reveals that at 22:57 UTC, there are two updraft maxima which straddle the area in between a positive ζ region to the north and two negative ζ minima to the west and south. This pattern is highly suggestive of a vortex line arch (VLA) feature which was observed in Straka et al. (2007) and Markowski et al. (2008), the latter through pseudo-dual-Doppler analyses of six supercell thunderstorms (see their Fig. 2–4). Per Markowski et al. (2008), VLAs typically extend upwards through the cyclonic vorticity maximum, turn horizontally towards the south or southwest, then turn downwards through the anticyclonic vorticity maximum. Specifically, given the typical orientation of a VLA compared to the ambient horizontal vorticity, the generating mechanism tends to be baroclinic generation of horizontal vorticity which is then tilted by a low-level updraft. While the straddling 1 km updraft weakens at 23:00 and 23:03 UTC, the couplet of positive / negative ζ remain (Fig. 15b–c).

While VLAs have been documented in previous literature both numerically (Weisman and Davis, 1998) and observationally through 3D wind synthesis retrievals (Majcen et al., 2006; Straka et al., 2007; Markowski et al., 2008), their presence within the literature is relatively sparse, so it is worthwhile to investigate whether vortex lines here are of the same nature as presented in those studies. Plotting vortex lines

originating from the surface within a manually-chosen 2×1 km box surrounding the positive surface ζ reveals that there are, in general, two clusters of vortex lines. The first cluster is a set of vortex lines that erupt upward from the surface and continue to tilt NW with height through the LLM and into the mid-level mesocyclone (black arrow Fig. 15d–f) while the second cluster is a set of VLAs that turn horizontally between 0.5 and 1.5 km AGL and descend downward through the region of negative ζ to the west and southwest (the southern minimum of ζ at 22:57 UTC is not associated with any VLAs and is likely just a reflection of the anticyclonic side of the rear-flank downdraft, RFD). The surface grid points at which these VLAs originate tend to be on the very SE flank of the positive ζ contour, and are collocated well with the DIs. Thus, it is possible that the main mechanism for near-surface ζ generation for this tornado could have been the production of VLAs. If this was the case, once 1) the weaker low-level updraft no longer sufficiently tilted horizontal vorticity to produce VLAs or 2) baroclinic boundaries responsible for producing horizontal vorticity weakened, near-surface ζ diminished and the relatively short-lived tornado dissipated. Given the lack of 1 km updraft in the 23:00 and 23:03 UTC analyses (Fig. 15b–c), the former is argued to be the more likely cause.

2.4.2 Segment 2

While 4 tornadoes officially occur during S2, and two are marked by a local temporal maximum in near-surface OW (Fig. 11), all four tornadoes were rated EF-0, with

tornadoes #3–5 having a path length of half a mile or less. Therefore, S2 is generally characterized as the most disorganized period during the observed storm lifecycle, especially at around 23:27–23:30 UTC where both w_{1km} and surface -OW are at or near their global minimum values (Fig. 10 and 11). Fig. 16 shows streamlines of the horizontal wind for 6 key points within S2, namely, the times at which the local temporal minima (23:09, 23:27, 23:48 UTC) and maxima (23:18, 23:39, 23:57 UTC) of surface OW occur. A horizontal streamline analysis is chosen for simple visualization of flow through the supercell at the lowest grid level, especially within the hook echo region.

Fig. 16a–b gives insight as to why the supercell fails to produce or maintain any appreciable surface ζ during the beginning periods of S2. Namely, the streamlines from the inflow region indicate that flow is quickly exiting through the back side (western edge) of the supercell. In fact, the old mesocyclone associated with tornado #1, located at $x = 45.5$ km and $y = 50$ km (marked by bending streamlines) in Fig. 16a, is also being advected towards the back of the storm and is not discernible by 23:18 UTC (Fig. 16b). Especially at 23:18 UTC, 1 km updrafts are weak and disorganized, and the -OW contours which are related to the local maxima in Fig. 11 are far displaced from the hook echo appendage and are likely not associated with the ongoing EF-0 tornado, though the absence of DIs makes that difficult to confirm. Given 1) the weak flow within the hook echo appendage and streamlines indicating flow through the supercell with no convergence associated with the RFD

and 2) the steadiness of the streamlines within the first half of S2 especially, any surface ζ is likely being shed towards the back of the storm. This would result in little to no residence time beneath the disorganized 1 km updrafts. In numerical simulations, prevention of vortex shedding and longer residence times of areas of more concentrated ζ beneath the updraft have been found to be a potential discerning factor in tornadogenesis success or failure (Fischer and Dahl, 2022) while failure of forward-flank (FF) parcels to reach the LLM have been associated with tornadogenesis failure (Murdzek et al., 2020b). Nevertheless, the advection speed of vortex patches relative to the updraft is known to have direct consequences on the likelihood of near-ground vortex intensification both observationally (Dowell and Bluestein, 2002b; Tanamachi et al., 2012; Skinner et al., 2014) and numerically (Markowski and Richardson, 2014; Guarriello et al., 2018; Murdzek et al., 2020b; Gray and Frame, 2021).

By 23:27 UTC, the structure of the supercell and its internal flow have been slightly modified. Namely, the hook echo contains larger amounts of precipitation, and the flow within the hook echo has obtained a northerly component, indicating that the flow may be wrapping around with the beginnings of an RFD, reducing surface ζ shedding (Fig. 16c). However, both surface OW and 1 km ζ reveal continued disorganization for the time being, with no surface OW $\leq -0.02 \text{ s}^{-1}$ and no $w_{1km} \geq 10 \text{ m s}^{-1}$. By 23:39 UTC, a small area of stronger negative surface OW has formed within the hook echo, below a weaker but broad 1 km updraft of $\sim 10 \text{ m s}^{-1}$ (Fig. 16d). Considering the correct placement of the stronger negative OW region, this may

be a reflection of the ongoing EF-0 tornado, although again, lack of DIs makes this difficult to confirm. One interesting feature to note between 23:27 and 23:39 UTC is a persistent region within the FF of the supercell that is characterized by stagnant flow. This region of stagnant flow is very shallow in nature, diminishing with height and only detectable below 750–1000 m. This feature is also resolved within the NOXP scans, but only within the 0.5 and 1.0° elevation angles.

At 23:48 UTC, the supercell has elongated significantly, and the flow within the FF region has become increasingly parallel to the reflectivity gradients, signifying a potential increase in streamwise baroclinic horizontal vorticity (investigated further in Chapter 3; Fig. 16e). While the negative surface OW from 23:39 UTC is no longer present, the hook echo takes on a more classic appearance, with a strong northerly component of the flow within the hook echo and even a slight westerly component, indicating a maturing of the RFD and associated flow. By 23:57 UTC, the last time of S2 and the analysis time just prior to an EF-2 tornado, the streamlines within the hook echo are strongly divergent, with the flow along the eastern reflectivity gradient exhibiting a more significant westerly component (Fig. 16f). Both of these indicate that an RFD surge may be occurring just before the supercell becomes significantly tornadic within S3.

2.4.3 Segment 3

As stated previously, S3 is the most actively tornadic period — although the total tornado count of four matches that of S2, three of the four were stronger than EF-0 with two being significantly tornadic (one EF-2 and one EF-3; Table 4). While the EF-2 and EF-3 were relatively short-lived (~ 2 and 4 min, respectively), tornado #9 (EF-1) was the longest-lived tornado within the analysis period by a factor of 3, lasting ~ 18 total minutes. Prior to tornado #9, the longest-lived tornado was tornado #1 lasting ~ 6 min. Therefore, the analysis here will focus on the ζ and w distributions near the LLM in an attempt to parse out 1) why stronger tornadoes were more frequent during S3 and 2) why tornado #9 was longer-lived compared to the other 8 tornadoes within the analysis period.

Fig. 17 depicts surface ζ and w_{1km} every 6 minutes within S3, starting from 00:06 UTC which is during the EF-3 tornado. Surface ζ patterns at 00:06 UTC expectedly show a broader area of positive ζ with a local maximum near the center of the rotation (Fig. 17a). What is perhaps more interesting is the displacement of the rotation center from the DIs at this time, which are located to the west and north. Based on the track of the DIs, it appears that the tornado takes a quick left turn to the north before dissipating. Due to spatial / temporal resolution limitations, the analysis does not seem to adequately capture the left turn of the tornadic rotation, and the rotation represented in Fig. 17a is likely more representative of the LLM. Nevertheless, this suggests that as the tornado turns left, it is displaced from its

parent mesocyclone / updraft leading to vortex dissipation shortly after producing EF-3 damage. Additionally, displacement of maximum surface ζ from stronger w_{1km} indicates lack of continuous ζ stretching, necessary for longer-lived tornadoes (e.g., Markowski and Richardson, 2014). This pattern continues into 00:12 UTC, where although strong surface rotation with a broad area of positive ζ exists, the displacement of strong w_{1km} from maximum surface ζ implies lack of more substantial ζ stretching.

However, this changes with the 00:18 UTC analysis (beginning of the longer-lived tornado #9), with stronger surface ζ values overlapping well with more intense w_{1km} (Fig. 17c). This favorable overlap not only occurs at the center of the surface rotation, but in a broad region extending a few kilometers to the NW of the rotation center. Thus, enhancement of low-level ζ in the area *surrounding* the surface rotation may be playing a key role in increased longevity with tornado #9. Favorable overlap at and to the NW of very tightly resolved rotation continues at 00:24 UTC, with the surface rotation matching well with the location of damage indicators (Fig. 17d). At 00:30 UTC, nearing the end of tornado #9's lifetime, overlap starts to become less favorable — while strong surface ζ associated with the surface rotation remains, w_{1km} is much weaker, with the 10 m s^{-1} just impinging on the edge of the surface ζ maximum (Fig. 17e). However, the supercell at 00:30 UTC is showing signs of cyclic behavior, with a new region of positive surface ζ juxtaposed with $w_{1km} \geq 15 \text{ m s}^{-1}$ to the northeast of the original rotation. It is also worthwhile to note that, once again, the original surface rotation is displaced to the east of the DIs, suggesting the

analysis is not adequately resolving the left turn of tornado. Finally, at 00:36 UTC, the tornado has officially dissipated, and while a strong surface ζ maximum remains, this is not associated with any upward vertical velocity (Fig. 17). It is surmised that, without any continued ζ stretching, the rotation has entered the spin-down phase in which frictional forces will slowly deplete the positive ζ .

Fig. 18 and 19 shows a quantitative measure of low-level ζ stretching and associated 3D ζ distributions at the same 6 min interval, respectively, reaffirming physical mechanisms alluded to in Fig. 17. Specifically, Fig. 18 quantifies the column-averaged vorticity stretching from 0 to 1 km AGL (over 5 vertical grid levels at and above the surface). At 00:06 UTC, although there is a continuous column of 0.03 s^{-1} ζ with 0.05 s^{-1} value between 1.5 and 4 km AGL (Fig. 19a), column-averaged vorticity stretching indicates that the center of the 0–1 km rotation is actually undergoing negative stretching (Fig. 18a), perhaps a reason why the tornadic rotation is not sustained. While weak positive 0–1 km ζ column-averaged stretching develops around the surface rotation (Fig. 18b), isosurfaces of ζ show scattering / disorganization of 0–1 km ζ with ζ aloft, leading to no continuous columns of positive ζ and a short-lived EF-0 occurring at this time (Fig. 19b).

These patterns change drastically at 00:18 UTC with an axis of larger positive 0–1 km ζ stretching extending out to the NW from the center of rotation which, based on direction of surface flow, may be feeding continuous vorticity at low-levels (Fig. 18c). This feeding of air with vertical vorticity enriched through stretching may be akin to

ζ ribbons that are a primary feature in the Orf et al. (2017) simulations and have been observed as cyclonic mesocyclone-scale vortices in (Snyder et al., 2013; Wurman and Kosiba, 2013; Wurman et al., 2014). The ζ ribbons in the simulation are stretched by low-level updrafts as they are advected towards the tornadic rotation, eventually merging and providing a stream of positive vorticity to the simulated vortex. While the spatiotemporal resolution here is not fine enough to capture such details, the location of positive ζ , positive column-averaged ζ stretching, and direction of 0–1 km storm relative flow indicate that the analysis may be observing such a phenomenon here. The 0.05 s^{-1} ζ isosurface at 00:18 UTC extends from the surface up to 2 km AGL and the 0.03 s^{-1} ζ isosurface nearly connects up to 5 km AGL (Fig. 19c) — additionally, the 0.03 s^{-1} ζ isosurface does extend to the NW of the main rotation, and again may be a coarse representation of vorticity ribbons feeding the tornadic rotation.

By 00:24 UTC, the region of 0–1 km positive column-averaged ζ stretching is still robust (Fig. 18d), and most importantly, this potential feeding of vorticity rich parcels into / near the rotation leads to a vertical consolidation of the ζ isosurfaces (Fig. 19d). The 0.05 s^{-1} ζ isosurface is connected to the surface, extends up past 5 km, and is actually continuous up to nearly 9 km AGL (not shown), indicating with near certainty that there exists a continuity between the near-surface, low-level, mid-level, and even upper-level rotation / mesocyclone. Even as the ribbon of positive 0–1 km column-averaged ζ stretching diminishes at 00:30 and 00:36 UTC (Fig. 18e–

f), the continuous 0.05 s^{-1} ζ isosurface remains. Nevertheless, the vertical extent of the 0.05 s^{-1} ζ isosurface does decrease to 5–6 km AGL (not shown) and the negative accumulated ζ stretching centered on the rotation at 00:36 UTC does indicate that the spin down period has indeed begun, with divergent flow at the surface leading to negative column-averaged ζ stretching values (Fig. 18f).

2.5 Trajectory Analysis and Potential Streamwise Vorticity Current (SVC)

Now that the evolution of the supercell through S1, S2, and S3, including LLM characteristics through ζ and w patterns and ζ stretching, has been documented in detail, we turn our attention towards trajectory analyses to determine source locations of LLM parcels and compare them to what has been found in numerical simulations of supercells. Backward trajectories will be heavily utilized in this analysis, and are calculated with a $\Delta t = 20 \text{ s}$ with reflectivity and winds being temporally interpolated using the time-morphing algorithm (Fig. 6). We note that the length and detail of this analysis provides the opportunity for a novel comparison between the observed supercell here and numerical counterparts, which have highlighted the consistency and importance of trajectories which cross the FF region and end up within the LLM.

The calculation of backward trajectories require the availability of 3D wind information upstream in time. While the DLA process calculates backward trajectories

starting from the first analysis time of 22:57 UTC, upstream information is provided by projecting the 22:57 UTC analysis back in time using the constant storm motion of $u_{storm} = 8.5 \text{ m s}^{-1}$ and $v_{storm} = 9.6 \text{ m s}^{-1}$. Therefore, the trajectories calculated at the earlier analysis times rely on the assumption that the supercell is steady-state prior to 22:57 UTC, which, given the evolving nature of the supercell, is an uncertain assumption at best. Therefore, we opt to conduct trajectory analyses for times after 23:45 UTC, which allows at least 45 min of non-steady state data for calculations. While trajectories farther removed from 22:57 UTC will rely on the steady-state assumption even less, 45 min is a sufficient time such that a significant amount of trajectories have already exited the storm environment and terminated within the inflow environment. Therefore, the uncertainties regarding steady-state use in trajectory calculations is acceptably reduced. We are especially confident that by 00:00 UTC, over an hour after the first analysis time of 22:57 UTC, steady-state assumptions are introducing negligible uncertainties into trajectory calculations.

The trajectory analysis has an emphasis on source areas of parcels that end up within the LLM, which is defined as any grid point within a $1.5 \times 1.5 \text{ km}$ box of the centroid, manually identified as the center of the 1 km rotation. Another reason why this analysis focuses on 23:45 UTC and onward is that the centroid of the LLM is rather obscure for the first half of S2 when the supercell is relatively disorganized. After 23:45 UTC, and after 00:00 UTC especially, the rotation associated with the LLM becomes more well-defined, and therefore the centroid is much easier to define

without subjective error. By investigating from the end of S2 to the beginning of S3, we can evaluate 1) changes in backward trajectory paths coincident with strengthening and organization of the LLM and 2) evolution of LLM trajectories during the most tornadic period in S3. From numerical supercell simulations, it is well-known that the trajectory of the LLM parcels can be directly responsible for modulations in LLM strength (e.g., residence times along baroclinic gradients). While direct calculations / analysis of parcel thermodynamics are left for Chapter 3, we can gain a general understanding of LLM parcel processes by simply examining backward trajectory paths.

At 23:45 UTC, most of the trajectories surrounding the relatively weak rotation at 1 km AGL are streaming in from directly east of the supercell while a few originate from the southeast (Fig. 20a). While trajectories from the southeast originate at around 1 km AGL, most of the trajectories coming in directly from the east flow very near to the surface before ascending into the LLM. While surface-based LLM parcels are no surprise, none of the parcels spend any appreciable time within higher-reflectivity regions and instead are a product of the undisturbed inflow environment. Thus, if past numerical studies are correct that tilting of baroclinically-generated horizontal streamwise vorticity is important to LLM maturation and maintenance, the trajectories here are consistent with this hypothesis as the LLM has yet to fully mature.

However, trajectories within the next few analysis times quickly begin to indicate

significant changes as the supercell begins to strengthen prior to the beginning of S3. With each 3 min interval, a larger proportion of trajectories begin to take a more curved, northward path as they approach the supercell before turning back to the south and ascending into the LLM. This is especially apparent by 23:51 UTC where the trajectories that terminate in the western half of the trajectory box stream in from ~ 10 km north of the LLM and flow south along the reflectivity gradient (Fig. 20b). Again, these trajectories originate and remain very close to the surface, suggesting that these parcels could be attaining some baroclinic horizontal vorticity during their residence time along the reflectivity gradient before being tilted into the LLM. This pattern continues and by 00:00 UTC, nearly all of the parcels in and around the LLM at 1 km AGL have curved trajectories through the FF region, with long residence times along the reflectivity gradient (Fig. 20c). Out of the 36 backward trajectories that terminate within the 1.5×1.5 km box, the number of trajectories that traverse along or to the west of the reflectivity gradient increases from only 1–2 at 23:45 UTC and 23:48 UTC, 6–8 at 23:51 UTC and 23:54 UTC, 17 at 23:57 UTC, and 24 at 00:00 UTC. We do note that radar imagery in the trajectory figures corresponds to the time that trajectories terminate, and therefore may not be completely representative of the state of the supercell where trajectories indicate interesting processes are occurring. Nevertheless, while vorticity tendency calculations are to be done in Chapter 3, this conceptualization of a stronger LLM associated with long-residence trajectories along the FF reflectivity gradient match

well with many numerical supercell simulations.

We can investigate a cross-sectional plane through which the component of the surface winds is large, such that any vertical rotation within the plane would have a significant streamwise component. Investigating vertical velocities within Fig. 21 indicate there is relatively little vertical velocity, especially within the lowest 2 km and more importantly, little change in vertical velocity with respect to the x-direction. This indicates that the storm has not generated significant amounts of resolvable streamwise vorticity at this location in the supercell. Direct calculations of baroclinic vorticity tendency as well as horizontal stretching through strong accelerations towards the LLM along parcel trajectories may yield more information regarding vorticity processes, and will be presented in Chapter 3.

Following 00:00 UTC, trajectory paths remain similar for 00:03 and 00:06 UTC — by 00:09 UTC, while there are still a good amount of parcels with long residence times along the FF region, there is a batch of trajectories that originate in the ambient environment and appear to be undisturbed by the storm. The proportion of trajectories with long residence times in the forward flank decreases in the 00:12 UTC analysis, and then again for 00:15 UTC (Fig. 20d). This change in trajectory paths does occur in conjunction with the presence of weaker -OW values within S3 from 00:09–00:15 UTC (Fig. 11). Increased curvature in parcel trajectories through the FF returns by 00:18 UTC and continues to 00:21 UTC, although the trajectory distribution is not as uniform as it was for 00:00–00:06 UTC with a number of trajectories

not encountering the FF air as they flow toward the LLM.

Unlike at 00:00 UTC, however, a cross-sectional analysis at 00:15 UTC through the trajectory paths just prior to reaching the LLM reveals an interesting horizontal rotor feature within the high-reflectivity centered at around $x = 81$ km at 1 km AGL (Fig. 22). Vertical velocity gradients along the x-direction suggest that positive horizontal vorticity would extend out a couple of kilometers both to the west and east. Evaluating the sense of horizontal vorticity with this rotor would yield the same direction as surface wind vectors, leading to the conclusion that trajectories associated with this rotor would contain streamwise horizontal vorticity and is suggestive of a potential SVC-like feature. The largest caveat here, however, is that the trajectory paths remain at the surface while the rotor itself is centered at $z = 1$ km, although vertical velocity gradients do suggest $dw/dx > 0$ down to $z = 250$ m. Additionally, even if the vorticity doesn't extend to the ground it could induce a negative pressure perturbation that is dynamically important for near-surface parcels. Again, direct calculations of baroclinic vorticity tendencies along parcel trajectories may yield more information on whether this rotor is a true SVC as found in numerical simulations.

Towards the end of S3, trajectory patterns become less uniform at 00:24 and 00:27 UTC, with some trajectories along the FF and some originating from the south of the LLM that originate between 1–2 km AGL (Fig. 20e). These two times are the only times where a substantial percentage of southern parcels originate from >1 km AGL — this may simply be a consequence of the trajectory box capturing

parcels outside the LLM, though it could be that the LLM does ingest some non-surface based parcels during this time as the occlusion process begins to overwhelm the LLM. Nevertheless, parcel trajectories along the FF reflectivity gradient continue to be a defining characteristic at 00:30, 00:33, and 00:36 UTC as the LLM becomes occluded and a new rotation center develops to its northeast. It is worthwhile to note that there do exist trajectories, especially at 00:33 UTC, which are not surface-based and actually originate at the backside of the supercell at heights >4 km (Fig. 20f). These parcels stream in from the northwest and descend within FF downdrafts before being ingested into the LLM.

In summary, this analysis, which illustrates that an observed strengthening LLM was associated with an increase in parcels which have backward trajectories through the FF — these results corroborate trajectories depicted in many numerical supercell studies. At the very least, it confirms that a majority of LLM parcels do have a history of traversing the FF region, and that it is highly unlikely in this case that all LLM parcels originate from the inflow environment.

2.6 Comparison to Mobile Mesonet Observations

The last portion of the kinematic analyses compares the lowest grid level results from the multi-Doppler analyses to MM observations. While the analyses farther above the surface have less uncertainty due to availability of radar data above the ground, radar data directly at the ground are typically 1) unavailable in the case of

Earth curvature effects from ground-based radar or 2) determined to be “bad” from quality-control processes due to ground clutter which is typically the case for the airborne radars. Thus, where surface data is not available, the OBAN methodology extrapolates the winds down from the levels that do have data just above the surface. Therefore, it is likely that some differences will exist between the analyses and the mesonet observations, and it is useful to compare where differences are greatest and what these differences could imply about both the kinematic analyses presented thus far as well as low-level shear implications.

Starting from around 00:00 UTC, the NSSL Mobile Mesonet Probe 2 was able to do transects within the high-precipitation forward-flank region as well as areas to the north of the LLM sampling the strongest of the inflow winds before exiting out the back of the storm again by around 00:33 UTC. Fig. 23a shows the mesonet transect of the entire FF region centered at 00:06 UTC \pm 3 min — it is apparent that the analysis surface winds capture the general trend of slackening and veering winds from west to east, but that the magnitude of gradients appears to be muted, as expected given the parameters used in the 1-pass Barnes analysis described earlier. Specifically, the analysis accurately captures northeasterly and even easterly winds on the backside of the high-reflectivity region transitioning to a more northerly component within the precipitation core and then attaining a light westerly component to the east of the reflectivity core. While speed within the analysis is overestimated in the analysis on the order of 5–10 kts in some regions, the analysis does correctly depict stronger

winds within the precipitation core and weaker winds to the west. The overestimation within the analysis is likely due to extrapolation error, and is perhaps not accurately capturing frictional effects very near to the ground where MM observations are taken (3 m AGL).

By 00:15 UTC, the MM began to transect areas north of the LLM where the strongest winds were located based on the surface wind analysis. At the beginning of the MM track (indicated by the black dot in Fig. 23b), the agreement between the analysis and the observations is fairly good — however, while there are areas where the analysis matches observations well (e.g., turn around point in the mesonet track in Fig. 23b), there are also areas where the analysis overestimates surface winds by 10–20 kts in some regions before 00:15 UTC (indicated by the black star in Fig. 23b). This bias is exaggerated further when looking at mesonet observations after 00:15 UTC where the MM winds are measuring 35–40 kts winds and the analysis shows surface winds exceeding 70–80 kts. Thus, it seems that the areas where differences between analysis and observations are the largest tends to be where analysis depicts the strongest winds close to the mature surface rotation.

Disagreements in direction are not as drastic as speed — however, observed mesonet winds do tend to be slightly more backed than the analysis winds in some regions (Fig. 23b). While this may not seem significant, a difference in direction may have large implications for frictionally-induced near-surface shear. Remember, analysis winds are overestimated due to the lack of near-surface velocity data and

resultant extrapolation from the vertical grid levels from just above the surface. At 250 m and 500 m, these winds are much more likely to be closer to the truth since they have been calculated directly through velocity radar data and not extrapolated downward. Thus, if we consider the mesonet winds to be accurate at the surface and analysis winds to be accurate at 250–500 m, this analysis implies very strong speed shear and some directional shear within the lowest 250–500 m AGL — the latter is important because without directional shear, all horizontal vorticity generated from this near-surface frictional shear would be crosswise.

If we do a rough calculation, we find that the depicted veering wind with height would lead to *streamwise* vorticity generation owing to frictional effects very close to the surface rotation center. From Fig. 23b, north of the rotation center, MM recorded approximately 40 kt flow from a direction of 5° while the wind synthesis has 75 kt from a direction of approximately 20° . If we assume 40 kt flow is realistic at the surface and the 75 kt flow is accurate at 250 m AGL where frictional effects are reduced, this gives 0.03 s^{-1} of vorticity in the x-direction and -0.022 s^{-1} vorticity in the y-direction. Using an average u-component / v-component of the flow of $-7.35 / -24 \text{ m s}^{-1}$ within the 0–500 m layer, the result is antisteamwise vorticity in the x-direction and streamwise vorticity in the y-direction. However, the latter dominates and the total streamwise vorticity from this kinematic profile would be 0.012 s^{-1} which is not insignificant. While we do ignore any effects of horizontal gradients in w in this rough calculation, this would corroborate recent studies such as Roberts

and Xue (2017) that have found frictionally-generated vorticity plays an important role in the intensification and maintenance of the LLM in supercells. These biases of overestimation of surface winds in the analysis compared to observations, along with slightly backed mesonet winds, continues at 00:24 UTC (Fig. 23c). Once the mesonet begins to exit to the northwest by transecting the forward-flank precipitation region at 00:33 UTC, there is once again good agreement between the observed mesonet winds and the surface analysis winds in both speed and direction within the FF region (Fig. 23d), although the analysis wind are rotated 10-20 degrees counterclockwise from the MM winds.

The question then becomes, what do these biases imply about the trajectory results given in the previous section (Chapter 2.5)? The largest biases are constricted to the area around the surface rotation, and that these biases are exaggerated when the rotation is at peak strength within the wind synthesis which occurs at 00:15 UTC and onward. While we hypothesize that much of the error would likely be in regards to the timing of the parcels into the LLM since the majority of the bias was in speed and not direction, a true sensitivity test would be needed to compare original trajectories to corrected trajectories where surface winds are modified to more closely match that of the MM observations. However, using a relatively small number of MM observations to correct these surface analysis is not trivial and is beyond the scope of this dissertation, but future work including potential publications stemming from this analysis should have sensitivity testing of these trajectories. Additionally,

different extrapolation techniques (e.g., logarithmic instead of linear), could yield more accurate surface measurements, but again this is left for future work. For now, we must use caution in interpreting results stemming directly from trajectories near the LLM at 00:15 UTC and beyond — this is especially true when vorticity tendency forcing terms along trajectories are analyzed in Chapter 3 and at the lowest grid level of the analysis which, as shown in the MM comparison to the analysis, has the larger uncertainty which is inherited by trajectory calculations.

2.7 Summary and Conclusion

The analysis herein presents a novel multi-Doppler analysis of the 17 May 2019 tornadic supercell that occurred in southwest Nebraska during the TORUS field campaign. While dual- or multi-Doppler analyses of supercells has been a widely used methodology to retrieve 4D kinematic data, this study is novel in that it details supercell evolution for an uninterrupted 99 minutes at 3 minute temporal spacing. Thus, not only does this allow for documentation of supercell features such as the LLM, FFD, and RFD, but the analysis records the evolution of these features through a supercell as it cycles from strongly tornadic (demarcated as segment 1 or S1 from 22:57 to 23:06 UTC), to weakly tornadic (S2 from 23:06 to 23:57 UTC), and then back to strongly tornadic with a mesocyclone occlusion phase (S3 from 23:57 to 00:36 UTC).

Time series of w at 1 km, ζ , and OW, show that the wind syntheses are accurately capturing the evolution of the LLM through the three segments, with the strength of

these parameters following closely to periods of strong tornadic activity / inactivity. Additionally, vortex lines within S1 show the presence of two vortex line clusters, one that tilts northwest with height into the mid-level mesocyclone and another cluster of VLAs that erupting upward from the surface ζ maxima and curve back down through contours of negative surface ζ . These VLAs have been noted only sparsely in past literature, and given the locations of DIs in comparison to the end of the arches suggest that vortex lines through the tornado itself may have been a part of the arching cluster. The lack of a steady low-level updraft to sustain the vortex line arches may have played a role in the short-lived nature of the first significant tornado.

During S2, the supercell was found to be disorganized with the hook echo containing weak flow with no obvious near-surface rotation. Streamline analysis shows streamlines from the FF region tend to exit through the back of the supercell, which is not an optimal configuration for long residence times of vortex patches to stretch under low-level updrafts. Near the end of S2, the supercell begins to organize once again, with northerly winds within the hook echo indicating the maturation of an RFD and a more classic hook echo. Via trajectory analyses, the proportion of LLM parcels that originate from the inflow environment begins to decrease from 23:45 UTC (LLM parcels almost exclusively from ambient environment) to 00:00 UTC (LLM parcels almost exclusively from the FF region) as the supercell begins to mature.

Finally, within S3 (the most active tornadic period), the analysis depicts intense rotation with large surface ζ values within and to the northwest of the center of the

rotation. However, stronger 1 km updrafts tend to be displaced from the ζ maximum at 00:06 and 00:12 UTC, which may be why the two significant tornadoes at the beginning of S3 tend to be short lived. This changes at 00:15 UTC where accumulated vorticity stretching shows strong positive values both at the rotation center and to the northwest of the ζ maximum that may be helping to continuously “feed” the LLM leading to a longer-lived tornado (18 min). This is akin to ζ ribbons / patches which have been documented previously both observationally and numerically to be important to tornadogenesis / maintenance processes. By 00:24 UTC, the 0.05 s^{-1} ζ isosurface extends all the way to 9 km AGL, indicating an extremely deep and continuous mesocyclone. Eventually, the 1 km updraft wanes and the rotation is left to spin-down as the longer-lived tornado dissipates at 00:33 UTC. Trajectory analyses through all of S3 show that at least some parcels from the FF region are being ingested into the LLM. The regime change from majority inflow parcels to majority FF parcels within S3 as the supercell becomes actively tornadic suggests that baroclinic forcing terms are important in generating streamwise vorticity which is eventually realized as ζ within the LLM.

Future work needs to be done to correct strong surface wind biases close to the LLM within the analysis, including sensitivity testing on parcel trajectories. Additionally, the 20 dBZ reflectivity threshold to demarcate the storm edge should also undergo sensitivity testing to determine potential changes in the derived wind at the storm edge when increasing or decreasing that threshold — this may also affect tra-

jectories, especially those with long residence times along the transition zone between storm and inflow environment. Nevertheless, the results show the wind syntheses appear to faithfully capture the most significant dynamical supercell processes during the 99 min period. Various features that have been sparsely identified in past literature within an observational framework are shown to exist within an individual supercell, including vortex line arches as a tornadogenesis / maintenance mechanisms and LLM trajectories matching similarly to those involved in SVC processes within numerical simulations. Because of the impossibility of such an analysis without the capability of the P3 to follow the supercell, the authors encourage the continued use of airborne radars to observe supercells in conjunction with ground-based assets including radars and mobile mesonets.

3 Chapter 3: Analysis of 4D Thermodynamic Fields

Retrieved via Diabatic Lagrangian Analysis

3.1 Introduction

This chapter continues the analysis of the 17 May 2019 tornadic supercell in southwest NE, and attempts to begin to fill the gap associated with 3D thermodynamic observational data within supercells. Specifically, the gridded wind synthesis described in Chapter 2 is combined with objectively-analyzed (OBAN) radar data from all three radars and uses the diabatic Lagrangian analysis (DLA) technique detailed in Ziegler (2013a,b) to obtain gridded thermodynamic data (potential temperature, water vapor and cloud water mixing ratios, and virtual buoyancy). To our knowledge, an observed dataset with this amount of 3D thermodynamic data of a supercell is the first of its kind. In this chapter, we aim to verify the accuracy of the DLA thermodynamic retrievals using in-situ measurements and characterize the evolution of the near-surface buoyancy field, especially within the FFD and RFD. Additionally, trajectory budgets are conducted to assess the relevance of the terms in generating both horizontal and vertical vorticity, including the impact of baroclinic generation of streamwise vorticity.

3.2 Data and Methods

As detailed in Chapter 2.2, this study uses data from three radars that were deployed on the tornadic supercell on 17 May 2019, namely, the airborne aft and fore radars from the P3 and the ground-based NOXP radar. Details regarding the quality control (QC) process of the radar data can be found in Chapter 2.2. The QC'ed reflectivity and radial velocity were spatially interpolated onto a grid with horizontal and vertical grid spacing of 0.25 km using a 1-pass Barnes scheme and were temporally interpolated to each analysis time using a time-morphing scheme. The analysis period runs from 17 May 22:57 UTC to 18 May 00:36 UTC with a temporal spacing of 3 min, giving 34 individual analysis times. At each analysis time, the gridded reflectivity and velocity from the 3 radars were synthesized into a triple-Doppler wind synthesis to obtain the 3D wind field at each time. Full details on the OBAN and wind synthesis process can be found in Chapter 2.2.2.

3.2.1 Diabatic Lagrangian Analysis

The DLA technique, detailed in Ziegler (2013a,b), allows us to derive thermodynamic fields of potential temperature (θ) and virtual buoyancy (θ_v), as well as water vapor (q_v), cloud water (q_c), and other hydrometeor mixing ratios from the 3D gridded reflectivity and wind syntheses. Retrieval of thermodynamic fields is important in defining thermodynamic gradients that may be important in production of baroclinically-generated horizontal streamwise (SW) vorticity which can feed vorticity to the LLM.

This section will state the fundamentals of the DLA algorithm, but more detail can be found in Ziegler (2013a).

For a particular analysis time, the first step within the DLA was to calculate backward trajectories from each grid point within the DLA domain utilizing the gridded wind syntheses with a 4th order Runge-Kutta method and Δt of 20 s (small enough such that parcel displacements within consecutive time steps are smaller than resolvable wavelengths in the wind syntheses given typical storm wind speeds). The DLA domain is a smaller domain nested within the larger $125 \times 135 \times 16$ km domain that contains the supercell of interest, as calculations of backward trajectories and subsequent thermodynamic calculations were not necessary elsewhere. Specifically, the DLA domain is a $30 \times 30 \times 16$ km box around the supercell with the bottom left of the domain given by

$$x_{BL,i} = 0.25 * \text{floor}\left[\frac{32 + \frac{i*180}{1000}u_{storm}}{0.25}\right] \quad (9)$$

$$y_{BL,i} = 0.25 * \text{floor}\left[\frac{62 + \frac{i*180}{1000}v_{storm}}{0.25}\right] \quad (10)$$

at the i^{th} analysis time (starting at $i=0$ for 22:57 UTC) where $u_{storm} = 8.5 \text{ m s}^{-1}$, $v_{storm} = 9.6 \text{ m s}^{-1}$, and the *floor* function rounds down to the nearest integer. This ensures that $x_{BL,i}$ and $y_{BL,i}$ (given in units of km) is divisible by 0.25 km, i.e., the corners of the DLA domain were on the analysis grid.

As stated previously, the translation of the storm through the analysis period was fully contained within the stationary larger domain to simplify trajectory calculations. Each backward trajectory was checked at each time step to see if the trajectory had

reached an environment outside of the storm representative of the ambient environment defined by the sounding at that analysis time. A trajectory was terminated within the ambient / inflow environment if: 1) number of steps > 76 and reflectivity < 0 dBZ, 2) number of steps > 76 and vertical velocity (w) < 0.5 m s $^{-1}$ for at least five consecutive steps, or 3) the trajectory passed through any lateral boundary. After experimentation, it was determined that 90 minutes was sufficient for nearly all trajectories to meet one of the three criteria — for the few points that did not have a trajectory terminating after 90 minutes, the thermodynamic data for that grid point was determined by averaging non-missing values of surrounding grid points.

After a trajectory was terminated, the second step was to forward integrate a system of ordinary differential equations (ODEs) along that trajectory which represent heat and water substance conservation via microphysical diabatic heating/cooling and simple damping and surface flux parameterizations. Values of θ , q_v , and pressure of the starting trajectory point were initialized via the given sounding profile (q_c is initialized to 0). Recall that each analysis time has its own sounding profile determined by linearly interpolating between the sounding at 23:02:30 and 00:57:05 UTC (Fig. 7 and 8). Specifically, the ODEs determine how θ , q_v , and q_c evolves along the trajectory and are of the form

$$\frac{d\phi(\theta, q_v)}{dt} = M_\phi + D_\phi + F_\phi(\theta, q_v, q_c) \quad (11)$$

where M_ϕ represents the microphysical term, D_ϕ the damping term, and F_ϕ the surface mesoscale flux term. Further details on how these terms are parameterized are

given in Sections 2g-i in Ziegler (2013a) — specific equations for D_ϕ and F_ϕ can be found in Eq. (22) and (27). The parameterization for M_ϕ depends on whether the parcel was saturated and whether w was positive or negative, but includes physical processes of cloud evaporation / condensation, rain evaporation, rain collection and graupel accretion of cloud, graupel sublimation, and graupel melting. Various parameter values for the equations in Ziegler (2013a) are given in Table 5. The Runge-Kutta scheme also employed a predictor-corrector scheme which converges in three iterations making calculations more accurate, especially in strongly curved flow regimes (e.g., near the LLM). Spatially, the values of u , v , w , and reflectivity (Z_H) were trilinearly interpolated from the eight grid points surrounding the trajectory point — temporally, the storm was advected to the trajectory point time via the time-morphing algorithm described in Chap 2.2.2.

Parcels near the surface were specially treated such that there are no trapped trajectories as would be the case if the boundary condition was set to $w = 0 \text{ m s}^{-1}$. Thus, “surface” trajectories were initiated at a prescribed height $H_0 = 10 \text{ m}$ above ground level (AGL) and a parameterized surface downdraft was added in areas of precipitation which prevented trapping of surface trajectories, namely

$$w_{sfc} = \max[Z^* w_{mix0} w_{k=2}, w_{mix1}] \quad (12)$$

where Z^* is the reflectivity scale prescribed by

$$Z^* = \min[\max(\frac{Z_{H,k=1} - Z_0}{Z_{DDC} - Z_0}, 0), 1] \quad (13)$$

such that $0 \leq Z^* \leq 1$. Eqs. 12 and 13 were only valid if $w_{k=2} \equiv w_{500m} < 0 \text{ m s}^{-1}$; else, $w_{sfc} = 0 \text{ m s}^{-1}$. The values in the above equations are $w_{mix0} = 0.5 \text{ m s}^{-1}$, $w_{mix1} = -0.75 \text{ m s}^{-1}$, $Z_0 = 20 \text{ dBZ}$, and $Z_{DDC} = 50 \text{ dBZ}$ which represents the surface layer w scale, the minimum surface layer w , the minimum reflectivity, and the peak surface downdraft-core reflectivity, respectively. The relationship between radar reflectivity and precipitation content as well as full details on bulk precipitation size distribution parameters, precipitation parameters and moments, etc. are not repeated here, but can be found in Ziegler (2013a) in Sections 2c-f. Once the ODEs are calculated along each trajectory ending at each grid point, the last step in the DLA was to smooth the fields with a horizontal nine-point elliptic low-pass filter to minimize small-scale, poorly resolved variations.

3.3 Comparison to Observations

3.3.1 Comparison of Surface Thermodynamics to Mobile Mesonet Observations

As stated in both the previous section and in Chapter 2, the DLA requires calculations of backward trajectories at each grid point until the trajectory is determined to have terminated in the non-storm environment, at which point it is initialized using the inputted sounding. Thus, in order to calculate trajectories for analysis times closer to 22:57 UTC, the 22:57 UTC analysis has to be advected backward in time to allow enough time for trajectories to terminate. This requires a steady-state assumption

prior to 22:57 UTC, which given the evolution of the supercell documented in Chapter 2, is likely to introduce significant departure from reality. Thus, we restrict the DLA presented herein to times after 23:30 UTC, with most analysis focusing on 23:45 UTC and onward — this gives over 30 min for trajectories to terminate within the inflow environment — the handful that do not are not likely presenting significant thermodynamic errors from steady-state assumptions.

Following in line with the end of the analysis in Chapter 2.6, we aim to compare the DLA to observations to determine in what aspects the DLA is performing well and in what situations we should be cautious in interpreting results. While the DLA is an extremely powerful tool, the reliance of thermodynamic calculations on backward trajectories which may have some errors given three minute spacing on analysis times warrant a closer look before proceeding further. Two comparisons will be made: first, surface analyses will be compared with MM observations and secondly, thermodynamic characteristics within the DLA updraft will be compared to two soundings that were launched near 00:00 UTC and were ingested into the updraft. These two comparisons will give an estimate on accuracy in both the near-surface baroclinic zones (e.g., FF and near-mesocyclone region) and within the updraft and allow for evaluation of DLA accuracy in key supercell regions.

Probe 2 of the National Severe Storms Laboratory’s MM began to approach the supercell just after 23:30 UTC and started to transect within the FF region at around 23:36 UTC. The mesonet operated in and around the supercell, mostly within the FF

and north of the LLM, until around 00:33 UTC at which point it exits the storm to the northwest. This gives nearly a full hour of comparison between the DLA and MM observations. Specifically, the variable to compare is chosen to be θ_v , because it gives a measure of the accuracy of both temperature and moisture. In order to compare the 1 Hz mesonet observations with the 3 min analyses, each mesonet observation is correlated to the closest analysis (temporally) which is then advected accordingly in time (using $u_{storm}=8.5$ and $v_{storm}=9.6$ m s⁻¹) to match the time and location of the MM observation. The largest caveat to this comparison is that, while the analyses are advected to match the MM observation as closely as possible, no evolution of the supercell (including baroclinic boundaries) is resolved in between the 3 min analyses. This means that it is possible for the MM observations to differ from the DLA due to unresolved supercell evolution — however, this comparison provides a good understanding of how the DLA is performing, especially in areas of baroclinic gradients, before proceeding with the rest of the analysis.

Fig. 24 shows the time series of MM θ_v and the DLA θ_v . It is apparent that the DLA does not match the MM observations exactly — specifically, at times when the DLA does not match observations, it tends to overestimate θ_v by as much as 2–3 K in areas of maximum disagreement. Through the entire ~ 1 hr, the mean and median bias of the DLA compared to the MM observations is 1.21 and 1.31 K, respectively. If we shift the DLA θ_v in Fig. 24a by the mean bias, we find that the analysis (especially beyond 23:50 UTC) θ_v agrees with MM θ_v fairly well, especially

in regards to the magnitude of θ_v increase from approximately 00:05 – 00:11 UTC and θ_v decrease from 00:28 – 00:32 UTC. Running a Pearson correlation coefficient for the entire time series reveals a value of 0.775, which indicates that 60% variance in the MM observations is shared in the DLA analysis for θ_v — if the time series is restricted to 23:50 UTC and after, this correlation value increases to 0.827. However, even when corrected for bias, there are times when the DLA still has a cool bias (e.g., 23:40 – 23:45 UTC), a warm bias (e.g., 23:55 – 00:05 UTC), or indicates boundaries that are not detected by MM observations (e.g., 00:14 UTC).

What do these results indicate about the meaningfulness of the DLA and what information can be extracted from the gridded thermodynamic data? Firstly, we must take caution when evaluating small-scale variations / features within the thermodynamic fields, as these are the most likely to be improperly resolved and could differ the most from MM observations. Secondly, given the overall warm bias presented within the DLA, it is better to not focus on exact thermodynamic values but rather the gradients in thermodynamic fields and use them to generate conclusions about the environment, e.g., it would not be wise to investigate storm-scale modifications on calculated absolute values such as CAPE since those are sensitive to surface thermodynamic values. That being said, in general the DLA is acceptably skillful in assessing both the location and magnitude of baroclinic gradients within the storm as demonstrated by 60% covariance through the entire time series. Thus, the main focus of the results herein Chapter 3 will be on characteristics of baroclinic gradi-

ents, including the resultant potential of these gradients in generating baroclinic SW vorticity and general locations of warmer versus cooler θ_v values.

3.3.2 Comparison of Vertical Velocities and Above-Ground Thermodynamics to Sounding Observations

In addition to MM observations, there were two soundings launched at 23:55:38 and 00:00:33 UTC, respectively, that were released within the inflow environment but were close enough to the supercell to be ingested in and around the updraft region. Because the DLA provides thermodynamic information above the surface up to the top of the domain (16 km AGL), it is worthwhile to compare upper-air observations to the DLA to assess performance away from the surface. The values of w obtained from the sounding can also be compared to the wind synthesis to determine the accuracy of w values in and around the updraft. The latitude, longitude, and time value (in seconds after launch) are used to determine the closest analysis time which is then advected as necessary to the time at which the data is collected, similar to the process of correcting the MM data. Once the closest grid point to the observation is determined, the w and θ_v data are linearly interpolated to the recorded height AGL using the column associated with that grid point. We approximate the ascent rate of the balloon to be 5 m s^{-1} which is subtracted from the recorded total balloon ascent to obtain w . While the ascent uncertainty owing to not knowing the exact buoyancy of the balloon is likely $\pm 1.5 \text{ m s}^{-1}$, uncertainties from turbulent eddies and water

loading increase the total uncertainty which is set to $\pm 4 \text{ m s}^{-1}$.

Fig. 25 shows the profiles of w and θ_v from the sounding launched at 23:55:38 UTC and how the values compare to the wind synthesis and DLA. From the surface up to about 4.5 km AGL, the difference between the sounding and the wind synthesis is such that w from the wind synthesis is contained within the error bars of w from the sounding, except for a few pockets from 2–3 km AGL where the analysis slightly underestimates the observed vertical velocities (Fig. 25a). Above 4.5 km, the updraft within the wind synthesis becomes much stronger than the sounding values — this may be due to the inability to resolve smaller updraft pulses within the analysis, or the structure of the analyzed mid-level updraft may be slightly different than what occurred and was sampled by the balloon path. Regardless, the agreement (especially within the lower-levels of the storm) is encouraging since the main portion of the analysis is focused closer to the surface. In terms of θ_v , we see a somewhat similar pattern in that the agreement is better closer to the surface and begins to diverge aloft (Fig. 25b). However, θ_v diverges earlier, with an underestimation in the analysis by about 5 K by ~ 3 km AGL which continues to increase with height. Upon investigation, the DLA may be under-predicting cloud coverage around the supercell — while RH values in the sounding data converge to 100% by ~ 1.2 km AGL, the RH within the DLA remains under 100% at this location as the sounding has yet to be ingested by the main updraft. However, sensitivity testing related to the amount of cloud water mixing ratio in and around the updraft has been performed, and the

qualitative results relating to the surface baroclinic gradients (where the analysis is focused) were unaffected. Therefore, we remain confident that differences in cloud cover and thus θ_v between the analysis and observation do not negate results presented herein.

Last, Fig. 26 shows the same comparison but for the sounding launched at 00:00:33 UTC. Unlike the previous sounding, the sounding at 00:00:33 UTC does not get ingested into the main updraft as maximum observed w (corrected for balloon ascent) stays in between 5–10 m s⁻¹. Looking at the wind synthesis w minus the sounding w , the zero value is contained within error bars demonstrating acceptable agreement between the two (Fig. 26a). The jump in w from the wind synthesis at around 2.5 km AGL is related to a new analysis time being used for comparison, and illustrates the inability of the analysis to capture the likely strengthening updraft in between these two analysis times. In terms of θ_v , the analysis tends to underestimate the values of θ_v , with the differences growing larger above 1.2 km AGL and maximizing at around 6 K at 3.4 km AGL — again, this is likely representative of a cloud-layer away from the main updraft that is underpredicted within the DLA, but should not affect surface thermodynamic analyses or low-level updraft characteristics.

In summary, there do exist differences between the analyses and observed thermodynamic measurements from Probe 2 and estimated w values from two soundings launched at 23:55:38 and 00:00:33 UTC. However, there is acceptably good correlation between mesonet and analyzed θ_v values, especially when corrected for the slight

warm bias of the analysis. Given potential errors of using a constant balloon ascent of 5 m s^{-1} , the vertical velocity comparisons show that the main updraft is well-predicted in the lower part of the storm. While θ_v values tend to be underestimated in the analysis, these differences do not occur until above 1.2 km AGL. Given all this, we feel comfortable with the performance of the DLA, and continue the analysis bearing these differences in mind.

3.4 Thermodynamic Analysis

The following subsection presents an analysis of the DLA in terms of thermodynamic supercell characteristics and how these features evolve through the course of the DLA period. Once again, in order to mitigate errors that may accrue from steady-state assumptions, only times after 23:30 UTC will be investigated, and the heavy focus will be on the strengthening period into the actively tornadic period after 23:45 UTC.

3.4.1 Updraft Structure

We first investigate the representation of the updraft within the DLA in order to 1) ensure that the updraft is properly ingesting parcels that originate below the lifted condensation level (LCL) and condensing water vapor into them as they lift and 2) study cloud-updraft structure and how this evolves as the supercell matures. In regards to the former, it is expected that above the LCL, the DLA should resolve positive cloud-water and cloud-ice mixing ratios as parcels condense water vapor into

liquid and, as a result of latent heat release, should result in positive θ_v perturbations where the cloud-water and cloud-ice mixing ratios are the highest. Additionally, given the continuous vertical structure of the updraft especially after 00:00 UTC, we expect that the cloud-updraft structure will be vertically continuous, and cross-sections through the updraft will be shown to ensure that this is the case. A handful of times from 23:30 to 00:36 UTC will be selected for this analysis, spaced every 21 minutes to capture some evolution regarding the supercell, namely 23:30, 23:51, 00:12, and 00:33 UTC. Figs. 27–30 show the cross sections of reflectivity, w , θ_v perturbation (θ_v'), water vapor mixing ratio (q_v), rain / graupel + hail / snow mixing ratio (q_{r+g+s}), and cloud water + ice mixing ratio (q_{cw+ci}) through the updraft at each of the four times — while the selected cross section is chosen to best capture the entirety of the updraft structure, it should be stated that they do not capture all of the important details. For example, some of the times have updrafts with a comma-head like structure (Fig. 28a) that cannot be seen by the cross-section (Fig. 28b). Nevertheless, these cross sections are chosen such that, in conjunction with the 6 km AGL horizontal view, these figures give a good idea of updraft characteristics for these four times.

At 23:30 UTC at 6 km AGL, the wind synthesis and DLA produces a weak echo hole (WEH) collocated with the strongest $w > 40 \text{ m s}^{-1}$ associated with the mid-level updraft (Fig. 27a). Thermodynamically, this is associated with a small maximum of q_{cw+ci} exceeding 2.5 g kg^{-1} and slightly positive θ_v' compared to the immediate

surrounding area (latent heat is enough at this level to lead to positive θ_v'). The cross-sectional view, which gives the view as if looking at the cross section from the south, shows the WEH extending up through 10 km with $w > 50 \text{ m s}^{-1}$ extending up through the same height (Fig. 27b). Positive q_{cw+ci} are continuous through above 10 km starting from about 1.25 km AGL, which represents the first vertical grid level above the LCL indicating parcels being drawn from below the LCL, condensing, and releasing latent heat. The maximum θ_v' from latent heat release through the cross section occurs at around 6 km AGL, and it is apparent that q_v for a given height within the updraft is larger than the ambient environment owing to the vertical displacement via upward motion before the water vapor is condensed into cloud water. The largest q_{r+g+s} is collocated with the highest reflectivity which makes intuitive sense. From the 23:30 UTC analysis, it seems as if the DLA is performing as expected and there are no glaring issues with regards to updraft characteristics. It should be noted that the core of the updraft with positive q_{cw+ci} is relatively narrow (less than 1 km in the x-direction between 2–5 km). While the skinny reflection of the updraft is partially owing to the SW to NE oriented cross-section across the updraft that is elongated in the NW to SE direction (Fig. 27a), the core of the updraft is relatively smaller at this time, which is feasible given the higher degree of disorganization at 23:30 UTC.

Fig. 28a shows relatively the same patterns at 23:51 UTC as 23:30 UTC, except that it is clear the core of the updraft has become more consolidated by this time, consistent with ongoing supercell maturation. The WEH is centered at $x = 74$,

$y = 81$ with strong upward motion at 6 km. Condensation and latent heat release within the updraft is more significant, with a much broader area of positive θ_v' and a consolidated core with maximum q_{cw+ci} values around 4 g kg^{-1} . The cloud structure via q_{cw+ci} has an obvious comma shape structure, which indicates the updraft is helical in nature, which has been noted both numerically (e.g., Lemon and Doswell, 1979; Klemp and Rotunno, 1983) and observationally through similar DLA methods (personal communication with Conrad Ziegler). Latent heat release is enough to lead to values of $\theta_v' > 2 \text{ K}$. Taking a SSW to NNE orientated cross-section shows the WEH extending to 7–8 km AGL with strong upward motion throughout (Fig. 28b). Parcels begin to condense and form a cloud base at 1.25 km AGL, this time several kilometers wide at the base continuing up through 6 km. Above 6 km, the cloud becomes slightly skinnier in the x-direction, though the highest q_{cw+ci} values nearing 4 g kg^{-1} are found at about 7 km AGL. The broad area of positive nonzero q_{cw+ci} matches well with positive θ_v' (maximum between 2–3 K) and an obvious bulge upward of q_v . Not surprisingly, due to the updraft, highest values of q_{r+g+s} are suspended far above the ground at 6.5 km AGL, with little indicated precipitation at the ground beneath the updraft.

Fig. 29a represents a more complex scenario at 00:12 UTC where the wind synthesis actually depicts 4 separate (but relatively close) vertical velocity maxima leading to a broad area of positive q_{cw+ci} at 6 km AGL with maximum values of $q_{ci+cw} > 2 \text{ g kg}^{-1}$. In fact, reflectivity indicates two weak echo holes as well as two separate

regions of strong convergence, one located at $x = 78$, $y = 92$ km and another at $x = 84$, $y = 94$ km associated with two separate areas of vertical velocities $> 40 \text{ m s}^{-1}$. This disorganization of the mid-level updraft, even though the supercell has matured at this time, is perhaps not too surprising given the results in Chapter 2.3. Recall that the isosurfaces of vertical vorticity at this time via Fig. 19 are also relatively disjointed, with a 0.03 s^{-1} connected to the surface, but disconnected from two different vertical vorticity isosurfaces aloft that have values $> 0.05 \text{ s}^{-1}$. These two 0.05 s^{-1} ζ isosurfaces aloft are associated with the two updraft maxima with cyclonic rotation. Given the complex patterns, it is impossible to take a single cross section that show the complex nature of the updraft at 00:12 UTC — thus, the cross section chosen is SW to NE oriented through the maximum q_{cw+ci} at 6 km (Fig. 29b). Beyond the same patterns seen in 23:30 and 23:51 UTC (WEH, strong vertical velocities, etc.), we note that the cross section does go through two separate updrafts with a weak downdraft in the middle centered at 3 km AGL. The updraft to the east is associated with a higher positive q_{cw+ci} values (that tilt with height) along with more positive θ_v' .

On a similar note, the analysis at 00:33 UTC also shows two updraft maxima, but this time owing to the fact that the supercell is beginning to cycle. The southwestern updraft / circulation is associated with the old mesocyclone and one to the northeast is the newly formed updraft (Fig. 30a; recall that in Fig. 19, the old mesocyclone still shows a coherent 0.05 s^{-1} ζ isosurface despite the occlusion process). Thus, we

choose to take the cross-section through the two updraft maxima which correlates well with the two maxima in q_{cw+ci} . The vertical velocities in Fig. 30b show that we are successfully transecting the two updraft cores, with both having $w > 40 \text{ m s}^{-1}$. There is a difference in the height of the maximum w with the old updraft centered at 4 km AGL and the new updraft at around 6–7 km AGL. Beyond the height of maximum w , the two updrafts have other differing characteristics that are worth comparing. Perhaps the most obvious one is the difference in q_{cw+ci} — while the old updraft has q_{cw+ci} nearing 5 g kg^{-1} in the mid-levels, the new updraft has maximum values closer to 3 g kg^{-1} . This is reflected in θ_v' values, with a larger area exceeding 3 K in the old updraft than the new one. Closer to the LCL, it is also validating to see that the old updraft contains a slightly wider base right at the LCL compared to just aloft, representing the classic bell-shaped updraft that is often seen in the field.

In summary, kinematic and thermodynamic evaluation of the updrafts at four separate times via cross-sectional analyses reveal that the DLA is performing as it should. The analysis is adequately resolving WEHs where stronger vertical velocities occur, with appropriate condensation occurring at the LCL extending continuously through at least 10 km. Condensation and subsequent latent heat release is accompanied by positive θ_v' , and the highest values of q_{r+g+s} are confined to the mid-levels as updrafts suspend hydrometeors far above the surface. Evaluation of updraft evolution reveals complex changes in cloud width both at the base and in the mid-levels, along with multiple maxima of mid-level vertical velocity at 00:12 UTC and 00:33 UTC,

the latter potentially owing to cyclical supercell processes occurring at the end of the analysis period.

3.4.2 Evolution of Near-Surface Baroclinic Boundaries

Given the heavy focus within both numerical and observational supercell literature on analyzing and observing baroclinic boundaries within supercells, both within the FF and RF regions, perhaps the most important feature to be analyzed within the DLA is near-surface θ_v ' gradients. Specifically, the development of these boundaries as the supercell strengthens and becomes significantly tornadic, as well as how they evolve during the longer-track tornado into the occlusion process, is documented in this section. For organization, the analysis is split into two parts, one from 23:30 UTC to 00:00 UTC (hereafter, the weakly tornadic period) and the second after 00:00 UTC (hereafter, the strongly tornadic period).

The evolution of the surface θ_v ' field during the weakly tornadic period is shown in Fig. 31. At 23:30 UTC, the maximum θ_v deficits run between 4–5 K, with two separate pockets of colder air, one within the middle of the forward-flank region and another that is being shed out of the back of the storm (Fig. 31a). Recall that the supercell at this time is at its weakest point, and the θ_v analysis in Fig. 31a–b gives a couple of insights as to potentially why that is. Firstly, the wind vectors roughly illustrate that the the flow is not organized along the θ_v gradients, especially further away from the hook echo where there is a strong component perpendicular

to the θ_v ' contours. Secondly, and perhaps most importantly, while the flow just to the north and northwest of the hook echo is oriented parallel to the θ_v contours, the wind vectors roughly indicate that none of these parcels have trajectories towards the hook echo (assuming steadiness). Rather, flow is exiting towards the back of the storm (also seen in the streamline analysis in Fig. 16) and the cold pool is clearly being advected away from the storm. This pattern is potentially unfavorable for near-surface ζ generation beneath the low-level updraft perhaps because there is no barrier to beneficially modify the advection speed of vortex patches to have longer residence times beneath the low-level updraft (e.g., Dowell and Bluestein, 2002b; Markowski and Richardson, 2014; Guarriello et al., 2018; Murdzek et al., 2020b; Gray and Frame, 2021). Fig. 31c shows another cold pool pulse with θ_v deficits between 5–6 K at 23:42 UTC. This time, however, the evolution of this cold pool pulse ends up being different than the last — rather than being advected away from the storm, the surface winds obtain a more northerly component by 23:48 UTC (Fig. 31d), which becomes a key player in the organization and strengthening of the supercell over the next 15 min. Larger θ_v deficits remain close to and within the hook echo region, setting the stage for supercell maturation as flow becomes more parallel to the θ_v contours leading to longer residence times of surface parcels along these gradients.

One feature of interest that begins to show up at 23:48 UTC is a pocket of warmer air (with positive θ_v ') that begins to develop to the north and northwest of the main cold pool, the result of some sub-saturated adiabatic warming within a downdraft.

These warm pockets have been observed fairly frequently in mobile mesonet data in this region of supercells (Sean Waugh, personal communication). The warm pocket here is a persistent feature, and strengthens at 23:54 and 00:00 UTC, with a relatively large area of +1–2 K θ_v ' (Fig. 31e–f). This warm pocket associated with the downdraft is attendant with divergence at the surface northwest of the LLM, and it results in surface flow north of the hook echo obtaining a stronger northerly component. While this warm pocket is stronger within the DLA than within MM observations, two spikes in MM θ_v correlating with two spikes in DLA θ_v collocated with the warm pocket suggests that this warm pocket does indeed exist, and is associated with a downdraft inducing adiabatic warming of parcels (Fig. 24).

Additionally, w_{1km} begins increasing after 23:45 UTC indicating a strengthening of the LLM (Fig. 10) which may also be inducing favorable pressure gradients for more curved flow towards the LLM. By 23:54 and 0000 UTC, surface θ_v deficits of 3–4 K have impinged on the hook echo region, with surface wind vectors indicating long residence times along these baroclinic gradients as confirmed in Fig. 20. While the strongest deficits are consistently 5–6 K, it is important to note that the inflow notch / region remains clear of any θ_v deficits at all, which suggest that the supercell and LLM still have access to high θ_e air associated with warm, moist near-surface inflow.

After 00:00 UTC, the supercell enters the strongly tornadic phase, and the surface θ_v evolution is shown in Fig. 32. From 00:06 to 00:12 UTC, the cold pool begins to

surge rapidly to the south, seen most clearly by the surge of the -4 K θ_v ' contour to >5 km south of the center of the surface circulation (Fig. 32a–b). Though the cold pool still remains to the west of the surface circulation and the inflow is yet to be undercut, we can see the beginnings of what may be colder air wrapping around to the south of the surface circulation with a tail of 3–4 K surface θ_v deficits protruding to the southeast of LLM (Fig. 32b). At 00:18 UTC (Fig. 32c), there is a clear downdraft within the RFD region indicated by both divergent flow and weaker θ_v deficits centered at $x=82$ and $y=91$ km indicative of adiabatic warming / compression— this downdraft is reminiscent of an internal RFD surge or RFD momentum surge that has been documented extensively in both observations (e.g., Markowski, 2002; Grzych et al., 2007; Hirth et al., 2008; Skinner et al., 2014; Atkins et al., 2014; Satrio et al., 2021) and numerical work (e.g., Mashiko et al., 2009; Schenkman et al., 2014). Because of this internal RFD surge, θ_v deficits by 00:24 UTC to the south of the hook echo actually are warmer than what they were at 00:18 UTC, but it is at this point that the inflow begins to be impacted by the colder air (Fig. 32d). Parcels characterized by 3–4 K θ_v deficits have wrapped all the way around to the east of the surface circulation, and strong southerly winds indicate that this colder air will continue to be advected northward until the inflow into the surface circulation is choked off. Indeed, this is what happens at 00:30 UTC, as colder θ_v ' has wrapped around the circulation marking the completion of the occlusion process with the warmer surface inflow air having no direct path to the LLM (Fig. 32e). This continues at 00:36 UTC,

with the vortex spinning down and seemingly about to be completely undercut by very cold $-5-6$ K θ_v air from the north, though this is unconfirmed since the analysis ends at this time (Fig. 32f).

In summary, the evolution of the surface baroclinic gradients show 1) initial shedding of colder air away from the storm, 2) warm pocket generation from a downdraft, 3) shift to northerly flow within the hook echo leading to potential damming of surface vorticity underneath the LLM and long residence times of parcels along baroclinic gradients around 00:00 UTC after an EF-2 tornado, 4) surging of colder air southward associated with strong RFD winds including a potential internal RFD surge during the longer-lived EF-1 tornado, and 5) eventual wrapping of cooler air around the surface circulation essentially choking off warmer inflow air and marking the potential beginning of the occlusion process. While this evolution has been seen in numerical simulations, this is the first study that has shown the full surface thermodynamic evolution from the nontornadic to tornadic to the occlusion phase.

3.5 Trajectory Analysis: Vorticity Budgets

Given the intense baroclinic gradients along the forward-flank region coupled with the backward trajectory analysis in Chapter 2.5 that shows a large number of LLM parcels originating from along those gradients, a more in-depth look on the parcel trajectories and vorticity tendency forcing terms is warranted. This includes calculation of baroclinic generation of SW horizontal vorticity along those trajectories

and their potential / role in producing low-level vertical vorticity by way of tilting and stretching as these parcels approach the LLM. While vorticity budget analyses are done frequently within numerical model studies, difficulty in obtaining both accurate parcel trajectories and thermodynamic information within an observational framework makes this type of analysis novel.

3.5.1 Residuals

First, it is worthwhile to first discuss some potential caveats / shortcomings of vorticity tendency calculations along the parcel trajectories. The first one has been previously stated, namely, the time morphing algorithm assumes linear evolution between the 3 min spaced analysis times, which may lead to erroneous parcel paths and thus poorly constrained calculation of vorticity forcing terms given this assumption. Additionally, 250 m grid spacing may not capture finer-scale details such as tight thermodynamic gradients that may be important to vorticity budgets — while this is less of an issue in numerical simulations that have much finer spatial resolution, unresolved features here may also contribute to vorticity tendency errors along the trajectory. Last, absence of near-ground ($< 250\text{-m}$) data and subsequent extrapolation of data to the surface contributes to uncertainties in both parcel trajectory and vorticity tendency calculations. Therefore, the residuals (computed minus observed) in both horizontal and vertical vorticity can end up being relatively large, especially compared to typical residual values within CM1. This can be especially true in areas

where the gradients in wind speed are very large (e.g., near a strong rotation center).

Figure 33 shows the accumulated vorticity residuals at each of the four times that will be analyzed — 23:45, 00:00, 00:15, and 00:30 UTC — where the accumulated residual is simply defined as the sum of the residuals at each time step (computed minus observed) over the entire 15 min trajectory. For the most part, the accumulated residuals are contained within $\pm 1 \text{ s}^{-1}$ over the 15 min, except for a couple of notable exceptions. Namely, streamwise vorticity at 23:45 UTC is drastically underestimated within the calculations and ζ at 00:15 UTC is also underestimated. These significant disagreements will be referenced in the context of the trajectory analysis below. Otherwise, while ± 0.5 to 1 s^{-1} accumulated error may not seem very significant, this translates to an average of approximately 0.01 to 0.02 s^{-1} error per time step, or per 20 s. In the context of vorticity, this can be somewhat large, and again, is likely due to the reasons mentioned above. Overall, via Fig. 33, there is a tendency to underestimate vorticity terms rather than to overestimate terms.

Nevertheless, it is argued that valuable information about baroclinic and barotropic vorticity tendency forcing mechanisms along parcel trajectories can still be extracted. To prevent overreaching conclusions from the analysis hereafter, we opt to focus mainly on the sign of forcing mechanisms, i.e., whether each forcing term is contributing positively or negatively to vorticity, rather than calculated tendency magnitudes. Additionally, while individual trajectories are analyzed, these will be assessed in conjunction with an ensemble of trajectories such that we do not draw false conclusions

from any potential errant or outlier trajectories. Last, calculations for vorticity tendency forcing terms are constricted to 15 min prior to the specified analysis time — we believe that most of the “important” dynamics as it relates to ζ generation happen within these 15 minutes, and that calculating tendencies beyond that serves to only unnecessarily increase residuals. With these caveats in mind, vorticity budgets along parcel trajectories will be analyzed for 23:45, 00:00, 00:15, and 00:30 UTC — as will be shown, drawing conclusions from 00:15 and 00:30 UTC become more difficult due to the intensity of wind gradients around the intense LLM, so much of the focus will be on 00:00 UTC trajectories, where vorticity budget calculations illustrate notable vorticity generation processes. At each time, 36 trajectories are initiated around a 1.5×1.5 km box around the 1 km AGL circulation.

3.5.2 Analysis

Recall that at 23:45 UTC, the supercell is becoming slightly more organized in that it has formed a typical hook echo indicated by a reflectivity appendage, but has yet to show a well-defined closed rotation or appreciable low-level updraft (Fig. 16d–e). Fig. 20a also showed that nearly all trajectories around the LLM originate from the undisturbed inflow environment. Via a representative parcel, it is clear that because the parcel originates in the inflow and does not cross any reflectivity gradients, the baroclinic forcing terms (θ_v solenoid and hydrometeor loading) are negligible along the parcel path and that barotropic terms are responsible for modifications in SW and

crosswise (CW) vorticity (Fig. 34). Because flow within the hook echo is disorganized and relatively weak compared to the inflow environment, deceleration of the parcel at it approaches the hook results in consistent negative tendencies of SW vorticity. In terms of ζ tendencies, it is only within the last minute of the approach that the vertical stretching becomes positive — because tilting of streamwise and crosswise vorticity into the vertical is negligible, it is likely that this is stretching of existing ζ due to cyclonic horizontal shearing of the flow.

Upon analyzing the streamwise and ζ forcing terms along *all* 36 trajectories at 23:45 UTC, it is evident that the baroclinic terms do not play a significant role in SW vorticity generation for almost all parcels. Additionally, negative SW stretching associated with deceleration approaching the hook is consistent amongst all 36 LLM parcels (Fig. 35). However, this compression of streamwise vorticity may be exaggerated in the analysis, as residuals indicate computed streamwise vorticity is drastically less than the observed streamwise vorticity (Fig. 33a). This may be due to the assumption that external to the storm, the environment is initialized using the appropriate reference sounding — meaning that, apart from smoothing the storm winds to the ambient winds, 1) we are not taking into account any modifications the storm may induce onto its own environment and 2) the inflow environment is homogeneous. These assumptions may be introducing errors in trajectory calculations, and therefore, trajectory calculations which traverse through only the storm environment (e.g., FF parcels) may be less prone to these errors. Nevertheless, during the

last minute of approach to the hook, as most parcels ascend up to 1 km AGL, the other forcing terms tend to diverge. Specifically, there are both positive and negative tendencies observed for stretching of SW vorticity, tilting of horizontal vorticity into the ζ , and stretching of ζ . This lack of consistent positive vorticity tendencies is potentially a key reason why the supercell failed to produce a consolidated LLM at 23:45 UTC.

At 00:00 UTC, parcel trajectories change significantly as most take a curved path through the FF region before turning southward into the LLM (Fig. 20c). Intuitively, the immediate hypothesis is that baroclinic forcing is likely to play a more significant role, and this is indeed shown to be the case. Looking at an individual trajectory that takes a long path through the FF region in the 15 min prior to entering the LLM, it is apparent that the baroclinic contributions to SW vorticity, both in terms of the θ_v solenoid and hydrometeor loading forcing terms, are small but consistently positive for T-15 to approximately T-5, where T-0 is the time of trajectory termination (00:00 UTC in this case; Fig. 36). Then, approximately starting at T-3, that accumulated SW vorticity is then tilted into ζ at which point it is then stretched from T-1 to T-0. Looking at a different trajectory that terminates to the southeast of the LLM center shows a similar story, in which there are (large) positive contributions to SW vorticity from θ_v solenoid forcing from T-11 to T-8 before intense accelerations yield strong SW stretching from T-8 all the way to T-0 (Fig. 37). Beginning at T-6 until T-1, SW vorticity is tilted into the vertical while simultaneously being stretched

from T-3 to T-0.

The ensemble of trajectories confirm the processes indicated in Fig. 36 and 37 — namely, looking at trajectories that end with an observed ζ value of 0.01 s^{-1} or greater (17 of the 36 trajectories), parcels undergo positive baroclinic forcing from T-15 to T-9, generating positive SW vorticity (Fig. 38). Starting from T-7 to about T-2, these parcels undergo SW stretching which enhances the positive SW vorticity that is baroclinically generated. This enhanced SW vorticity is then realized into ζ through tilting from T-3 to T-0, while simultaneously being stretched by convergence under the LLM, especially within the last minute. This process of

1. Baroclinic generation of SW horizontal vorticity along parcel trajectories parallel to baroclinic gradients,
2. Stretching of SW horizontal vorticity through accelerated flow towards the LLM, and
3. Tilting and stretching of SW horizontal vorticity into appreciable ζ associated with the LLM circulation

is the first instance within known literature explicitly quantifying such a process within an observed long-lived, tornadic supercell as it is producing a significant tornado through vorticity tendency calculations. Keeping the caveats mentioned previously in mind and given acceptable residuals for 00:00 UTC (Fig. 33b), this analysis confirms not only the existence of baroclinic gradients within the FF region, but that

these baroclinic gradients play a role in the generation of SW horizontal vorticity that eventually becomes ζ within the LLM. These processes along the trajectories are analogous to SVC parcels within numerical simulations, and gives strong evidence that these processes seen in some numerical simulations are occurring prior and during the primary strengthening period of the LLM. Whether or not SVCs are pertinent to every supercell remains to be seen, but the combination of θ_v gradients, trajectory paths along those gradients, and positive baroclinic SW vorticity forcing terms shown here provide observational justification to features seen in numerical simulations.

At 00:15 UTC, there are two groupings of trajectories, one group that originates from the undisturbed inflow environment and another group which takes a path through the FF region. It is found that the trajectories that originate from the inflow environment tend to meander below but close to the LLM before ascending to 1 km AGL (not shown) from T-15 onward. Because the LLM at this time is extremely robust, the gradients of u , v , and w are quite large, and it is likely that the analysis is not adequately resolving and capturing even finer-scale gradients that play a significant role in vorticity forcing terms / tendencies. Therefore, we choose to plot only trajectories which traverse through the FF region (Fig. 39). Though there are a few individual trajectories which do have non-negligible SW baroclinic forcing tendencies which get tilted and stretched into ζ , it is clear that most trajectories, even though they take a path through the FF, do not obtain SW vorticity through baroclinic mechanisms. Positive contributions to ζ come in the form of stretching of

ζ as parcels enter an intense convergence zone to the west / northwest of the LLM, consistent with the area of strong accumulated vertical vorticity stretching (recall Fig. 18). While the individual lines for ζ stretching in Fig. 39 look rather chaotic, this seems to be a result of individual trajectories hitting peak ζ stretching at different times, dependent on when that trajectory enters the convergence zone. Investigating closely does show that almost all parcels undergo positive ζ stretching after T-3 especially.

Therefore, this indicates that baroclinic SW vorticity contribution from θ_v gradients within the FF region become less important at 00:15 UTC to the LLM ζ . However, given 1) the significant decrease of uniformity of tendency calculations amongst individual trajectories compared to 00:00 UTC and 2) the stark overestimation of surface analysis winds compared to MM winds at 00:15 UTC, we are less confident in the 00:15 UTC results compared to the 00:00 UTC results. In addition, it is important to note that given the median residuals slightly underestimate both streamwise and crosswise vorticity, and that ζ is being significantly underestimated, it is more than likely that tendency calculations are not capturing forcing terms adequately, as it relates to both generation of horizontal vorticity and tilting / stretching into ζ . Therefore, it is possible that baroclinic mechanisms are still playing a non-negligible role, even though Fig. 39 shows otherwise.

While the residuals for 00:30 UTC are fairly acceptable, the distribution of individual vorticity tendency budgets amongst the 36 trajectories at 00:30 UTC become

even more chaotic than 00:15 UTC, so we opt not to show or interpret those results at the caution of attempting to draw conclusions from inconclusive results — the one consistency of the 00:30 UTC results is strong ζ stretching values occurring from T-4 to T-1. Thus, the one persistent conclusion among all four times that can be drawn is that, along parcel trajectories that terminate in and around the LLM which have a final ζ value that is positive, the large majority of the positive ζ is acquired only at the last portion of the trajectory (T-4 or sooner) which corroborates numerical studies that have shown this result for some time (e.g., Klemp and Rotunno, 1983).

3.6 Summary and Conclusions

Using the diabatic Lagrangian analysis approach developed by Ziegler (2013a,b), this chapter presented a 4D thermodynamic analysis of the 17 May 2019 tornadic supercell observed during TORUS. Given the sparsity of thermodynamic analyses of supercell in past literature, especially when considering 3D observations, simply the availability of the data for a long-track, cyclic supercell is significant and novel. Comparisons to MM observations show acceptable covariance for surface θ_v within the analysis for the hour between 23:33 and 00:33 UTC, signifying the usefulness and accuracy the thermodynamic data at the lowest level within the analysis. This also gives confidence that analysis regarding baroclinic boundaries as well as their evolution in correlation with supercell and LLM evolution is rooted in reality. Above the surface, 1) comparisons of the DLA to two separate soundings launched at 23:55:38 UTC and

00:00:33 UTC and 2) cross-sections through the updraft showing continuous positive w along with positive q_{cw+ci} where there is positive θ_v' , confirm that the DLA is resolving the updraft well in terms of both kinematics (e.g., w) and thermodynamics (e.g., condensing below-LCL parcels).

Surface θ_v' evolution from 23:30 to 00:00 UTC show cold pool pulses initially are shed to the west of the storm, with a lack of northerly component indicating an absence of a more mature RFD. It is also hypothesized that the lack of an RFD would also prevent any vortex patches (which are not resolved in the analysis due to the 250 m grid spacing) from incurring long residence times beneath the low-level updraft necessary for ζ stretching and enhancement of LLM and stronger surface ζ . However, by 23:48 UTC, a stronger cold pool pulse occurs with surface θ_v deficits reaching 5–6 K — this occurs nearly simultaneous with a surface warm pocket of θ_v' values of 1–2 K to the northwest / west of the cold pool pulse. Assuming there is a relative high / low associated with the coldest / warmest θ_v air, this would suggest a dynamic horizontal pressure gradient force that drives flow to the north of the hook echo to obtain a more northerly component by 23:54 UTC. This develops into a classic RFD with a wrapping reflectivity appendage around the circulation by 00:00 UTC. More analysis on other cases would need to be completed to deduce whether a warm pocket feature is common in other supercells, and whether this warm pocket is associated with RFD development.

Trajectory analyses at 23:45 UTC show barotropic forcing terms dominate over

baroclinic terms, which is not unexpected given nearly all LLM trajectories do not traverse through the FF or any precipitation regions. While negative SW vorticity generation is a consistent feature amongst all trajectories as flow decelerates in approach to the LLM, this seems to be exaggerated as residuals of SW vorticity are significantly more negative compared to other residuals. This does raise questions about the validity of neglecting the role the storm plays in modifying its own environment — parcels which traverse through precipitation regions do not have this issue, as velocity data is obtained from radar radial velocity rather than input soundings.

At 00:00 UTC, surface θ_v shows the cold pool maintains 5–6 K deficits while avoiding undercutting of the LLM from warmer inflow air. However, an internal RFD momentum surge indicated by a relative warm pocket within the RFD along with strongly divergent flow at 00:18 UTC leads to a surging of cooler air to the east of the RFD by 00:24 UTC, eventually cutting off the LLM from surface inflow parcels by 00:30 UTC. By 00:36 UTC, cut off of the old circulation by -5–6 K θ_v parcels seems to be imminent, though the end of the analysis prevents confirmation that this actually happens.

Perhaps most importantly, trajectory analyses at 00:00 UTC show that vorticity tendency forcing terms with parcels through the FF behave analogous to parcels associated with SVCs in numerical simulations. Namely, parcels attain SW vorticity at the surface through baroclinic mechanisms (θ_v solenoid plus differential hydrometeor loading) which is enhanced through horizontal stretching via acceleration to the

LLM. Once the parcel is within three minutes of the LLM, this is then tilted into ζ and stretched via the low-level updraft. To the author's knowledge, this is the first study to explicitly calculate these terms in the context of a long-track supercell producing a significant tornado, showing that SVC processes in numerical simulations have concrete observational backing. While trajectories at 00:15 and 00:30 UTC become more chaotic due to intense flow gradients near the LLM, it is apparent via all the trajectory calculations that the vast majority of ζ is not attained until the very end, where tilting and especially vertical stretching become dominant indicative of a mature LLM and tornado.

While a sensitivity analysis on trajectory calculations needs to be performed to allow for closer matching of analysis surface winds to MM winds (as stated in Chapter 2), the DLA results allow for detailed evolution of thermodynamic features on a cyclic, tornadic supercell, which is the first of its kind. The authors encourage the continued use of the DLA on other tornadic and non-tornadic supercells, as well as non-supercell storms. Despite its shortcomings, the DLA is extremely powerful tool in attaining 4D thermodynamic data given availability of gridded reflectivity and wind data. In the future, gridded polarimetric variables from dual-polarimetric radar (such as NOXP) can be used to improve the DLA for even more accurate thermodynamic retrievals.

4 Chapter 4: Thoughts on the Future of Observational Supercell Work

Upon completing the analysis for this dissertation, it is clear that even though observational supercell work has been a main focus within the severe storms community for decades, there are still many questions left unanswered. For example, why two supercells in a seemingly similar environment can have drastically different evolutionary paths is a frequently asked question, answering this has remained an extremely difficult challenge. It has quickly become evident that the answer to this question lies within internal storm-scale processes such as cold pool generation and internal boundary evolution, but these processes must be related to the broader scale environment in some shape or form — one must keep this in mind when attempting to disentangle one from the other. Thus, how should the severe storms community proceed with future supercell observations to discover pieces to this extremely complex puzzle? And how does the work and methodologies presented within the dissertation fit within the scope of future severe storms research?

Firstly, vorticity trajectory budgets within the DLA show that parcels ingested into the LLM are likely both a product of the undisturbed inflow environment as well as forward-flank parcels. Forward-flank parcels attain streamwise horizontal vorticity through baroclinic gradients associated with the forward-flank cold pool, so it is clear that numerical simulations which have emphasized the importance of the

SVC in providing ζ to the LLM are indeed rooted in reality. This is perhaps the most significant finding of the research presented herein, but it still leaves questions unanswered about the true nature of the SVC. Firstly, is the SVC a consistent feature across all supercells, or is it a feature that exists in some supercells and not in others depending on internal processes? Since the tornadic supercell here is shown to have an SVC, it may be tempting to conclude that SVCs are indeed important for LLM modulation in all supercells, but we caution against this generalization. Dynamics within supercells cannot be binned into binary categories, and it is possible (and perhaps probable) that some supercells contain SVCs and some supercells do not. In fact, the analysis herein shows the potentially transient nature of the SVC during its lifetime.

Additionally, the characteristics of the SVC within each supercell will likely be different depending on both internal processes and its environment (again, these two things are inherently tied together), so the next question would be: what does the spectrum of SVC characterization look like? For example, is the SVC a persistent feature as in numerical simulations that constantly supplies streamwise vorticity, or does it possess a more fickle nature upon where it comes and goes / strengthens and weakens? Again, both answers depend on the supercell, so understanding the spectrum of SVC characteristics and how this plays into LLM strength and modulation becomes a key question. Adding onto that would be the role of the RFD — within the analysis, RFD parcels for the most part are not ingested into the LLM, but its

maturation is tied to supercell and LLM strengthening. What then, is the true role of the RFD? We hypothesize that the RFD plays a significant role in preventing vortex patch shedding by essentially acting as a barrier or dam to the easterly storm-relative flow. While recent research has begun to show this process, the grid spacing is much too coarse here to resolve vortex patches which may stall and stretch beneath the LLM.

These are just some questions that stem from the work relating to internal supercell processes. How do we continue to find answers to these questions? By continuing to observe both tornadic *and* nontornadic supercells within the field as we have been doing. A main focus should be positioning radars in the field for long-duration dual- or multi-Doppler observations such as the data presented here to capture longer-scale evolution of the supercell. A key component to this is likely going to be the continued use of airborne radar given the difficulty of containing the storm within ground-based dual- or multi-Doppler lobes for long periods of time. Of course, ground-based instruments such as radars and mesonets are still essential at attaining higher-resolution data near the surface. DLA methods as described herein and in Ziegler (2013a,b) should be utilized more often where 3D wind data is available, as it gives a general representation of surface thermodynamics throughout the entire supercell. Additionally, there should be an emphasis on adequately combining airborne data with the higher-resolution surface observations to fill in and / or correct the data below 500 m — this would bring far more accuracy to the near-surface grid levels, replacing the

extrapolation approach.

While low-level data is typically the main focus (and for good reason), recent research has begun to investigate updraft properties as they relate to supercell behavior and evolution, e.g., updraft width. Data from airborne radars represent a prime opportunity to compile an observational dataset of updraft characteristics to compare to the numerical findings — because the weakness in utilizing P3 data is the lack of available data closest to the ground, analysis on the mid-level updraft is not susceptible to these issues. From personal conversation, there are several supercell cases from various field experiments in which the P3 collected data. Processing these cases through the efficient, automated QC script, OBAN, and wind synthesis workflow presented herein provides an opportunity for updraft characterization amongst numerous cases (including those that have already been completed). The comparisons of the wind synthesis to the two launched soundings that were ingested into the updraft shows the viability of the wind synthesis in attaining accurate vertical velocity measurements, even within the updraft core. While the vast majority of supercell literature focuses on low-levels, this would be a great opportunity to compile 3D observations of supercell updrafts which are likely correlated to low-level processes. Purposeful launches into the updraft of supercells, perhaps via windsondes to conduct more launches leading to a higher chance of updraft ingestion, would aid in verifying wind synthesis data for future updraft studies.

Last, there are two topics pertinent to supercells that remain relatively unan-

swered due to their complexities but are extremely important in understanding supercell behavior: storm environment modifications and the convective initiation into early evolution stage. Regarding the former, we are aware that storms modify the environments they are in, usually including enhanced inflow as well as changes in boundary layer characteristics due to processes such as leading edge precipitation or anvil shading. However, untangling these modifications and how the supercell responds to each one (i.e., what does the supercell actually “feel”) is extremely difficult, but is a research topic that should be expanded upon within the next decade. Ignoring storm-environment modifications may have led to larger residuals in vorticity calculations for LLM parcels that originated within the inflow environment. Regarding the latter, not much is known about the time from convective initiation to early evolution of the supercell, but it is likely that a lot of information about the future potential of a storm is contained within this time frame. On a given day, there are many updrafts that attempt to develop and even become deeply convective, but only a fraction of these will become a mature storm, a smaller fraction will become supercells, and an even smaller fraction will become tornadic. Because field experiments are typically designed to capture the mature (and potentially tornadic) phase of a supercell, this time frame is often missed or forgotten, but may hold some important pieces to the puzzle.

References

- Adlerman, E. J., K. K. Droegemeier, and R. Davies-Jones, 1999: A numerical simulation of cyclic mesocyclogenesis. *J. Atmos. Sci.*, **56**, 2045–2069.
- Atkins, N. T., K. M. Butler, K. R. Flynn, and R. M. Wakimoto, 2014: An integrated damage, visual, and radar analysis of the 2013 Moore, Oklahoma EF5 tornado. *Bull. Amer. Meteor. Soc.*, **95**, 1549–1561, <https://doi.org/10.1175/BAMS-D-14-00033.1>.
- Barnes, S. L., 1968: On the source of thunderstorm rotation. *ESSA Tech. Memo. ERLTM-NSSL*, Natl. Severe Storm Lab., Ed., Norman, OK, 28.
- Bartos, E. A., P. M. Markowski, and Y. P. Richardson, 2022: Three-dimensional thermodynamic observations in supercell thunderstorms from swarms of balloon-borne sondes. *Mon. Wea. Rev.*, **150**, 1689–1723, <https://doi.org/10.1175/MWR-D-21-0122.1>.
- Beck, J., and C. Weiss, 2013: An assessment of low-level baroclinity and vorticity within a simulated supercell. *Mon. Wea. Rev.*, **141**, 649–669, <https://doi.org/10.1175/MWR-D-11-00115.1>.
- Beck, J. R., J. L. Schroeder, and J. M. Wurman, 2006: High-resolution dual-Doppler analysis of the 29 may 2001 kress, texas, cyclic supercell. *Mon. Wea. Rev.*, **134**, 3125–3148, <https://doi.org/10.1175/MWR3246.1>.
- Brandes, E. A., 1984: Relationships between radar-derived thermodynamic variables

- and tornadogenesis. *Mon. Wea. Rev.*, **112**, 1033–1052, [https://doi.org/10.1175/1520-0493\(1984\)112<1033:RBRDTV>2.0.CO;2](https://doi.org/10.1175/1520-0493(1984)112<1033:RBRDTV>2.0.CO;2).
- Brooks, E. M., 1949: The tornado cyclone. *Weatherwise*, **2**, 32–33, <https://doi.org/10.1080/00431672.1949.9930047>.
- Browning, K. A., 1964: Airflow and precipitation trajectories within severe local storms which travel to the right of the mean wind. *J. Atmos. Sci.*, **21**, 634–639, [https://doi.org/10.1175/1520-0469\(1964\)021<0634:AAPTWS>2.0.CO;2](https://doi.org/10.1175/1520-0469(1964)021<0634:AAPTWS>2.0.CO;2).
- Browning, K. A., 1968: The organization of severe local storms. *Weather*, **23**, 429–434, <https://doi.org/10.1002/j.1477-8696.1968.tb03018.x>.
- Browning, K. A., and C. R. Landry, 1963: Airflow within a tornadic storm. *19th Weather Radar Conf.*, Amer. Meteor. Soc., Ed., Boston, MA, 116–112.
- Dahl, J. M., M. D. Parker, and L. J. Wicker, 2014: Imported and storm-generated near-ground vertical vorticity in a simulated supercell. *J. Atmos. Sci.*, **71**, 3027–3051, <https://doi.org/10.1175/JAS-D-13-0123.1>.
- Dahl, J. M. L., 2015: Near-ground rotation in simulated supercells: On the robustness of the baroclinic mechanism. *Mon. Wea. Rev.*, **143**, 4929–4942, <https://doi.org/10.1175/MWR-D-15-0115.1>.
- Davies-Jones, R. P., 1982a: A new look at the vorticity equation with application

to tornadogenesis. *12th Conf. on Severe Local Storms*, Amer. Meteor. Soc., Ed., Boston, MA, 249-252.

Davies-Jones, R. P., 1982b: Observational and theoretical aspects of tornadogenesis. *Topics in Atmospheric and Oceanographic Sciences: Intense Atmospheric Vortices*, L. Bengtsson, and J. Lighthill, Eds., Springer-Verlag, New York, 175–189, https://doi.org/10.1007/978-3-642-81866-0_14.

Davies-Jones, R. P., 1984: Streamwise vorticity: The origin of updraft rotation in supercell storms. *J. Atmos. Sci.*, **41**, 2991–3006, [https://doi.org/10.1175/1520-0469\(1984\)041<2991:SVTOOU>2.0.CO;2](https://doi.org/10.1175/1520-0469(1984)041<2991:SVTOOU>2.0.CO;2).

Davies-Jones, R. P., and H. Brooks, 1993: Mesocyclogenesis from a theoretical perspective. *The Tornado: Its Structure, Dynamics, Prediction, and Hazards*, G. Monogr., Ed., No. 79, Amer. Geophys. Union, 105–114, <https://doi.org/10.1029/GM079>.

Davies-Jones, R. P., R. J. Trapp, and H. B. Bluestein, 2001: Tornadoes and tornadic storms. *Severe Convective Storms*, M. Monogr., Ed., No. 28, Amer. Meteor. Soc., 126–221.

Dowell, D. C., and H. B. Bluestein, 1997: The Arcadia, Oklahoma, storm of 17 May 1981: Analysis of a supercell during tornadogenesis. *Mon. Wea. Rev.*, **125**, 2562–2582, [https://doi.org/10.1175/1520-0493\(1997\)125<2562:TAOSOM>2.0.CO;2](https://doi.org/10.1175/1520-0493(1997)125<2562:TAOSOM>2.0.CO;2).

Dowell, D. C., and H. B. Bluestein, 2002a: The 8 June 1995 McLean, Texas, storm. Part I: Observations of cyclic tornadogenesis. *Mon. Wea. Rev.*, **130**, 2626–2548, [https://doi.org/10.1175/1520-0493\(2002\)130<2626:TJMTSP>2.0.CO;2](https://doi.org/10.1175/1520-0493(2002)130<2626:TJMTSP>2.0.CO;2).

Dowell, D. C., and H. B. Bluestein, 2002b: The 8 June 1995 McLean, Texas, storm. Part II: Cyclic tornado formation, maintenance, and dissipation. *Mon. Wea. Rev.*, **130**, 2649–2670, [https://doi.org/10.1175/1520-0493\(2002\)130<2649:TJMTSP>2.0.CO;2](https://doi.org/10.1175/1520-0493(2002)130<2649:TJMTSP>2.0.CO;2).

Fischer, J., and J. M. L. Dahl, 2022: Supercell-external storms and boundaries acting as catalysts for tornadogenesis. *Mon. Wea. Rev.*, **151**, 23–38, <https://doi.org/10.1175/MWR-D-22-0026.1>.

Frame, J., P. M. Markowski, Y. P. Richardson, J. M. Strake, and J. M. Wurman, 2009: Polarimetric and dual-Doppler radar observations of the Lipscomb County, Texas, supercell thunderstorm of 23 May 2002. *Mon. Wea. Rev.*, **137**, 544–561, <https://doi.org/10.1175/2008MWR2425.1>.

Fujita, T., and H. Grandoso, 1968: Split of a thunderstorm into anticyclonic and cyclonic storms and their motion as determined from numerical model experiments. *J. Atmos. Sci.*, **25**, 416–439.

Gray, K., and J. Frame, 2021: The impact of midlevel shear orientation on the longevity of and downdraft location and tornado-like vortex formation within

- simulated supercells. *Mon. Wea. Rev.*, **149**, 3739–3759, <https://doi.org/10.1175/MWR-D-21-0085.1>.
- Grzych, M. L., B. D. Lee, and C. A. Finley, 2007: Thermodynamic analysis of supercell rear-flank downdrafts from Project ANSWERS 2003. *Mon. Wea. Rev.*, **135**, 240–246, <https://doi.org/10.1175/MWR3288.1>.
- Guarriello, F., C. J. Nowotarski, and C. C. Epifanio, 2018: Effects of the low-level wind profile on outflow position and near-surface vertical vorticity in simulated supercell thunderstorms. *J. Atmos. Sci.*, **75**, 731–753, <https://doi.org/10.1175/JAS-D-17-0174.1>.
- Helmus, J. J., and S. M. Collins, 2016: The Python ARM radar toolkit (Py-ART), a library for working with weather radar data in the python programming language. *J. of Open Research Software*, **4**, e25, <https://doi.org/10.5334/jors.119>.
- Hirth, B. D., J. L. Schroeder, and C. C. Weiss, 2008: Surface analysis of the rear-flank downdraft outflow in two tornadic supercells. *Mon. Wea. Rev.*, **136**, 2344–2363, <https://doi.org/10.1175/2007MWR2285.1>.
- James, C. N., and R. A. Houze, 2001: A real-time four-dimensional Doppler dealiasing scheme. *J. Atmos. Oceanic Technol.*, **18**, 1674–1683, [https://doi.org/10.1175/1520-0426\(2001\)018<1674:ARTFDD>2.0.CO;2](https://doi.org/10.1175/1520-0426(2001)018<1674:ARTFDD>2.0.CO;2).
- Jorgensen, D. P., P. H. Hildebrand, and C. L. Frush, 1983: Feasibility test of an

- airborne pulse-doppler meteorological radar. *J. Appl. Meteor. Climatol.*, **22**, 744–757, [https://doi.org/10.1175/1520-0450\(1983\)022<0744:FTO AAP>2.0.CO;2](https://doi.org/10.1175/1520-0450(1983)022<0744:FTO AAP>2.0.CO;2).
- Joss, J., and A. Waldvogel, 1970: A method to improve the accuracy of radar-measured amounts of precipitation. *14th Radar Meteorology Conf.*, Tuscon, AZ, Amer. Meteor. Soc., 237–238.
- Kessinger, C., P. Ray, and C. Hane, 1987: The Oklahoma squall line of 19 May 1977. Part I: A multiple Doppler analysis of convective and stratiform structure. *J. Atmos. Sci.*, **44**, 2840–2864, [https://doi.org/10.1175/1520-0469\(1987\)044<2840:TOSLOM>2.0.CO;2](https://doi.org/10.1175/1520-0469(1987)044<2840:TOSLOM>2.0.CO;2).
- Klemp, J. B., 1987: Dynamics of tornadic thunderstorms. *Annu. Rev. Fluid Mech.*, **19**, 369–402.
- Klemp, J. B., and P. S. Ray, 1981: Observed and numerically simulated structure of a mature supercell thunderstorm. *J. Atmos. Sci.*, **38**, 1558–1580.
- Klemp, J. B., and R. Rotunno, 1983: A study of the tornadic region within a supercell thunderstorm. *J. Atmos. Sci.*, **40**, 359–377, [https://doi.org/10.1175/1520-0469\(1983\)040<0359:ASOTTR>2.0.CO;2](https://doi.org/10.1175/1520-0469(1983)040<0359:ASOTTR>2.0.CO;2).
- Klemp, J. B., and R. B. Wilhelmson, 1978a: The simulation of three-dimensional convective storm dynamics. *J. Atmos. Sci.*, **35**, 1070–1096, [https://doi.org/10.1175/1520-0469\(1978\)035<1070:TSOTDC>2.0.CO;2](https://doi.org/10.1175/1520-0469(1978)035<1070:TSOTDC>2.0.CO;2).

- Klemp, J. B., and R. B. Wilhelmson, 1978b: Simulations of right- and left-moving storms produced through storm splitting. *J. Atmos. Sci.*, **35**, 1097–1110, [https://doi.org/10.1175/1520-0469\(1978\)035<1097:SORALM>2.0.CO;2](https://doi.org/10.1175/1520-0469(1978)035<1097:SORALM>2.0.CO;2).
- Klemp, J. B., R. B. Wilhelmson, and P. S. Ray, 1981: Observed and numerically simulated structure of a mature supercell thunderstorm. *J. Atmos. Sci.*, **38**, 1558–1580, [https://doi.org/10.1175/1520-0469\(1981\)038<1558:OANSSO>2.0.CO;2](https://doi.org/10.1175/1520-0469(1981)038<1558:OANSSO>2.0.CO;2).
- Kosiba, K., J. Wurman, Y. Richardson, P. Markowski, P. Robinson, and J. Marquis, 2013: Genesis of the Goshen County, Wyoming, tornado on 5 June 2009 during VORTEX2. *Mon. Wea. Rev.*, **141**, 1157–1181, <https://doi.org/10.1175/MWR-D-12-00056.1>.
- Lee, B. D., C. A. Finley, and C. D. Karstens, 2012: The Bowdle, South Dakota, cyclic tornadic supercell of 22 May 2010: Surface analysis of rear-flank downdraft evolution and multiple internal surges. *Mon. Wea. Rev.*, **140**, 3419–3441, <https://doi.org/10.1175/MWR-D-11-00351.1>.
- Lemon, L. R., and C. A. Doswell, 1979: Severe thunderstorm evolution and mesocyclone structure as related to tornadogenesis. *Mon. Wea. Rev.*, **107**, 1184–1197.
- Majcen, M., P. Markowski, Y. Richardson, and J. Wurman, 2006: A dual-Doppler analysis of a nontornadic supercell observed on 12 June 2004 using ground-based Doppler radars. *23rd Conf. on Severe Local Storms*, St. Louis, MO, Amer. Meteor. Soc., 15.2, available online at <http://ams.confex.com/ams/pdfpapers/115382.pdf>.

- Markowski, P., M. Majcen, Y. Richardson, J. Marquis, and J. Wurman, 2011: Characteristics of the wind field in three nontornadic low-level mesocyclones observed by the Doppler on Wheels radars. *Electron. J. Severe Storms Meteor.*, **6**, <https://doi.org/http://www.ejssm.org/ojs/index.php/ejssm/issue/view/28>.
- Markowski, P., E. Rasmussen, J. Straka, R. Davies-Jones, Y. Richardson, and R. J. Trapp, 2008: Vortex lines within low-level mesocyclones obtained from psuedo-dual-Doppler radar observations. *Mon. Wea. Rev.*, **136**, 3513–3535, <https://doi.org/10.1175/2008MWR2315.1>.
- Markowski, P., Y. Richardson, and G. Bryan, 2014: The origins of vortex sheets in a simulated supercell thunderstorm. *Mon. Wea. Rev.*, **142**, 3944–3954, <https://doi.org/10.1175/MWR-D-14-00162.1>.
- Markowski, P., and Coauthors, 2012: The pretornadic phase of the Goshen County, Wyoming, supercell of 5 June 2009 intercepted by VORTEX2. Part II: Intensification of low-level rotation. *Mon. Wea. Rev.*, **140**, 2916–2938, <https://doi.org/10.1175/MWR-D-11-00337.1>.
- Markowski, P. M., 2002: Mobile mesonet observations on 3 may 1999. *Wea. Forecasting*, **17**, 430–444, [https://doi.org/10.1175/1520-0434\(2002\)017<0430:MMOOM>2.0.CO;2](https://doi.org/10.1175/1520-0434(2002)017<0430:MMOOM>2.0.CO;2).
- Markowski, P. M., T. P. Hatlee, and Y. P. Richardson, 2018: Tornadogenesis in the 12 May 2010 supercell thunderstorm intercepted by VORTEX2 near

- Clinton, Oklahoma. *Mon. Wea. Rev.*, **146**, 3623–2650, <https://doi.org/10.1175/MWR-D-18-0196.1>.
- Markowski, P. M., and Y. P. Richardson, 2014: The influence of environmental low-level shear and cold pools on tornadogenesis: Insights from idealized simulations. *J. Atmos. Sci.*, **71**, 243–275, <https://doi.org/10.1175/JAS-D-13-0159.1>.
- Markowski, P. M., and Y. P. Richardson, 2017: Large sensitivity of near-surface vertical vorticity development to heat sink location in idealized simulations of supercell-like storms. *J. Atmos. Sci.*, **74**, 1095–1104, <https://doi.org/10.1175/JAS-D-16-0372.1>.
- Markowski, P. M., J. M. Straka, and E. N. Rasmussen, 2002: Direct surface thermodynamic observations within the rear-flank downdrafts of nontornadic and tornadic supercells. *Mon. Wea. Rev.*, **130**, 1692–1721, [https://doi.org/10.1175/1520-0493\(2002\)130<1692:DSTOWT>2.0.CO;2](https://doi.org/10.1175/1520-0493(2002)130<1692:DSTOWT>2.0.CO;2).
- Mashiko, W., H. Niino, and T. Kato, 2009: Numerical simulation of tornadogenesis in an outer-rainband minisupercell of Typhoon ShanShan on 17 September 2006. *Mon. Wea. Rev.*, **137**, 4238–4260, <https://doi.org/10.1175/2009MWR2959.1>.
- Murdzek, S. S., P. M. Markowski, and Y. P. Richardson, 2020a: Simultaneous Dual-Doppler and Mobile Mesonet Observations of Streamwise Vorticity Currents in Three Supercells. *Mon. Wea. Rev.*, **148**, 4859–4874, <https://doi.org/10.1175/MWR-D-20-0239.1>.

- Murdzek, S. S., P. M. Markowski, Y. P. Richardson, and R. L. Tanamachi, 2020b: Processes preventing the development of a significant tornado in a Colorado supercell on 26 May 2010. *Mon. Wea. Rev.*, **148**, 1753–1778, <https://doi.org/10.1175/MWR-D-19-0288.1>.
- Okubo, K., 1970: Horizontal dispersion of floatable particles in the vicinity of velocity singularities such as convergences. *Deep-Sea Res.*, **17**, 445–454, [https://doi.org/https://doi.org/10.1016/0011-7471\(70\)90059-8](https://doi.org/https://doi.org/10.1016/0011-7471(70)90059-8).
- Orf, L., R. Wilhelmson, B. Lee, C. Finley, and A. Houston, 2017: Evolution of a long-track violent tornado within a simulated supercell. *Bull. Amer. Meteor. Soc.*, **98**, 45–68, <https://doi.org/10.1175/BAMS-D-15-00073.1>.
- Parker, M. D., and J. M. L. Dahl, 2015: Production of near-surface vertical vorticity by idealized downdrafts. *Mon. Wea. Rev.*, **143**, 2795–2816, <https://doi.org/10.1175/MWR-D-14-00310.1>.
- Pauley, P. M., and X. Wu, 1990: The theoretical, discrete, and actual response of the Barnes objective analysis scheme for one- and two-dimensional fields. *Mon. Wea. Rev.*, **118**, 1145–1164, [https://doi.org/10.1175/1520-0493\(1990\)118<1145:TTDAAR>2.0.CO;2](https://doi.org/10.1175/1520-0493(1990)118<1145:TTDAAR>2.0.CO;2).
- Ray, P. S., 1976: Vorticity and divergence within tornadic storms from dual doppler radar. *J. Appl. Meteorol.*, **15**, 879–890, [https://doi.org/10.1175/1520-0450\(1976\)015<0879:VADFWT>2.0.CO;2](https://doi.org/10.1175/1520-0450(1976)015<0879:VADFWT>2.0.CO;2).

- Ray, P. S., and K. L. Sangren, 1983: Multiple-Doppler radar network design. *J. Climate Appl. Meteor.*, **22**, 1444–1454, [https://doi.org/10.1175/1520-0450\(1983\)022<1444:MDRND>2.0.CO;2](https://doi.org/10.1175/1520-0450(1983)022<1444:MDRND>2.0.CO;2).
- Ray, P. S., C. L. Ziegler, W. L. Bumgarner, and R. J. Serafin, 1980: Single- and multiple-Doppler radar observations of tornadic storms. *Mon. Wea. Rev.*, **108**, 1607–1625, [https://doi.org/10.1175/1520-0493\(1980\)108<1607:SAMDRO>2.0.CO;2](https://doi.org/10.1175/1520-0493(1980)108<1607:SAMDRO>2.0.CO;2).
- Roberts, B., and M. Xue, 2017: The role of surface drag in mesocyclone intensification leading to tornadogenesis within an idealized supercell simulation. *J. Atmos. Sci.*, **74**, 3055–3077, <https://doi.org/10.1175/JAS-D-16-0364.1>.
- Roberts, B., M. Xue, A. D. Schenkman, and D. T. Dawson, 2016: The role of surface drag in tornadogenesis within an idealized supercell simulation. *J. Atmos. Sci.*, **73**, 3371–3395, <https://doi.org/10.1175/JAS-D-15-0332.1>.
- Romine, G. S., D. W. Burgess, and R. B. Wilhelmson, 2008: A dual-polarization radar-based assessment of the 8 May 2003 Oklahoma City area tornadic supercell. *Mon. Wea. Rev.*, **136**, 2849–2870, <https://doi.org/10.1175/2008MWR2330.1>.
- Rotunno, R., 1981: On the evolution of thunderstorm rotation. *Mon. Wea. Rev.*, **109**, 577–586, [https://doi.org/10.1175/1520-0493\(1981\)109<0577:OTEOTR>2.0.CO;2](https://doi.org/10.1175/1520-0493(1981)109<0577:OTEOTR>2.0.CO;2).
- Rotunno, R., and J. B. Klemp, 1981: The influence of the shear-induced pressure

- gradient on thunderstorm motion. *Mon. Wea. Rev.*, **110**, 136–151, [https://doi.org/10.1175/1520-0493\(1982\)110<0136:TLOTSI>2.0.CO;2](https://doi.org/10.1175/1520-0493(1982)110<0136:TLOTSI>2.0.CO;2).
- Rotunno, R., and J. B. Klemp, 1985: On the rotation and propagation of simulated supercell thunderstorms. *J. Atmos. Sci.*, **42**, 271–292, [https://doi.org/10.1175/1520-0469\(1985\)042<0271:OTRAPO>2.0.CO;2](https://doi.org/10.1175/1520-0469(1985)042<0271:OTRAPO>2.0.CO;2).
- Satrio, C. N., D. J. Bodine, R. D. Palmer, and C. M. Kuster, 2021: Multi-radar analysis of the 20 May Moore, Oklahoma supercell through tornadogenesis and intensification. *Atmosphere*, **12**, 313, <https://doi.org/10.3390/atmos12030313>.
- Schenkman, A. D., M. Xue, and M. Hu, 2014: Tornadogenesis in a high-resolution simulation of the 8 May 2003 Oklahoma City supercell. *J. Atmos. Sci.*, **71**, 130–154, <https://doi.org/10.1175/JAS-D-13-073.1>.
- Schueth, A., C. Weiss, and J. M. L. Dahl, 2021: Comparing Observations and Simulations of the Streamwise Vorticity Current and the forward-flank convergence boundary in a supercell storm. *Mon. Wea. Rev.*, **149**, 1651–1671, <https://doi.org/10.1175/MWR-D-20-0251.1>.
- Shabbott, C. J., and P. M. Markowski, 2006: Surface in situ observations within the outflow of the forward-flank downdrafts of supercell thunderstorms. *Mon. Wea. Rev.*, **134**, 1422–1441, <https://doi.org/10.1175/MWR3131.1>.
- Skinner, P. S., C. C. Weiss, M. M. French, H. B. Blustein, P. M. Markowski, and Y. P. Richardson, 2014: VORTEX2 observations of a low-level mesocyclone

- with multiple internal rear-flank downdraft momentum surges in the 18 May 2010 Dumas, Texas, supercell. *Mon. Wea. Rev.*, **142**, 2935–2960, <https://doi.org/10.1175/MWR-D-13-00240.1>.
- Skinner, P. S., C. C. Weiss, J. L. Schroeder, L. J. Wicker, and M. I. Biggerstaff, 2011: Observations of the surface boundary structure within the 23 May 2007 Perryton, Texas, supercell. *Mon. Wea. Rev.*, **139**, 3730–3749, <https://doi.org/10.1175/MWR-D-10-05078.1>.
- Snyder, J. C., H. B. Bluestein, V. Venkatesh, and S. J. Frasier, 2013: Observations of polarimetric signatures in supercells by an X-band mobile Doppler radar. *Mon. Wea. Rev.*, **141**, 3–29, <https://doi.org/10.1175/MWR-D-12-00068.1>.
- Straka, J. M., E. N. Rasmussen, R. P. Davies-Jones, and P. M. Markowski, 2007: An observational and idealized numerical examination of low-level counter-rotating vortices toward the rear flank of supercells. *Electron. J. Severe Storms Meteor.*, **2**, 1–22, <https://doi.org/10.55599/ejssm.v2i8.13>.
- Tanamachi, R. L., H. B. Bluestein, J. B. Houser, S. J. Frasier, and K. M. Hardwick, 2012: Mobile, X-band, polarimetric Doppler radar observations of the 4 May 2007 Greensburg, Kansas, tornadic supercell. *Mon. Wea. Rev.*, **140**, 2103–2125, <https://doi.org/10.1175/MWR-D-11-00142.1>.
- Walko, R. L., 1993: Tornado spin-up beneath a convective cell: Required basic structure of the near-field boundary layer winds. *The Tornado: Its Structure, Dynamics,*

- Prediction, and Hazards*, G. Monogr., Ed., No. 79, Amer. Geophys. Union, 89–95, <https://doi.org/10.1029/GM079>.
- Wegener, A., 1928: Beitrage zur mechanik der tromben und tornados (Contributions to the mechanics of vortices and tornadoes). *Meteorol. Z.*, **45**, 201–214.
- Weisman, M. L., and C. A. Davis, 1998: Mechanisms for the generation of mesoscale vortices within quasi-linear convective systems. *J. Atmos. Sci.*, **55**, 2603–2622, [https://doi.org/10.1175/1520-0469\(1998\)055<2603:MFTGOM>2.0.CO;2](https://doi.org/10.1175/1520-0469(1998)055<2603:MFTGOM>2.0.CO;2).
- Weiss, C. C., D. C. Dowell, J. L. Schroeder, P. S. Skinner, A. E. Reinhart, P. M. Markowski, and Y. P. Richardson, 2015: A comparison of near-surface buoyancy and baroclinity across three VORTEX2 supercell intercepts. *Mon. Wea. Rev.*, **143**, 2736–2753, <https://doi.org/10.1175/MWR-D-14-00307.1>.
- Weiss, J., 1991: The dynamics of enstrophy transfer in two-dimensional hydrodynamics. *Physica D*, **48**, 273–294, [https://doi.org/https://doi.org/10.1016/0167-2789\(91\)90088-Q](https://doi.org/https://doi.org/10.1016/0167-2789(91)90088-Q).
- Wicker, L. J., and R. B. Wilhelmson, 1995: Simulation and analysis of tornado development and decay within a three-dimensional supercell thunderstorm. *J. Atmos. Sci.*, **52**, 2675–2703, [https://doi.org/10.1175/1520-0469\(1995\)052<2675:SAAOTD>2.0.CO;2](https://doi.org/10.1175/1520-0469(1995)052<2675:SAAOTD>2.0.CO;2).
- Wurman, J., and S. Gill, 2000: Finescale radar observations of the Dimmitt, Texas (2

- June 1995), tornado. *Mon. Wea. Rev.*, **128**, 2135–2164, [https://doi.org/10.1175/1520-0493\(2000\)128<2135:FROOTD>2.0.CO;2](https://doi.org/10.1175/1520-0493(2000)128<2135:FROOTD>2.0.CO;2).
- Wurman, J., and K. Kosiba, 2013: Finescale radar observations of tornado and mesocyclone structures. *Wea. Forecasting*, **28**, 1157–1174, <https://doi.org/10.1175/WAF-D-12-00127.1>.
- Wurman, J., K. Kosiba, and T. Marshall, 2014: The role of multiple-vortex tornado structure in causing storm researcher fatalities. *Bull. Amer. Meteor. Soc.*, **95**, 31–45, <https://doi.org/10.1175/BAMS-D-13-00221.1>.
- Ziegler, C. L., 2013a: A diabatic Lagrangian technique for the analysis of convective storms. Part I: Description and validation via an observing system simulation experiment. *J. Atmos. Oceanic Technol.*, **30**, 2248–2265, <https://doi.org/10.1175/JTECH-D-12-00194.1>.
- Ziegler, C. L., 2013b: A diabatic Lagrangian technique for the analysis of convective storms. Part II: Application to a radar-observed storm. *J. Atmos. Oceanic Technol.*, **30**, 2266–2280, <https://doi.org/10.1175/JTECH-D-13-00036.1>.
- Ziegler, C. L., D. Kennedy, and E. N. Rasmussen, 2004: A wireless network for collection and synthesis of mobile mesoscale weather observations. *J. Atmos. Oceanic Technol.*, **21**, 1659–1669, <https://doi.org/10.1175/JTECH1678.1>.

Table 1: Specifications of the NOXP radar as operated on 17 May 2019.

NOXP Specifications	
Antenna Type	Parabolic Dish
Polarization	Dual Linear
Latitude	40.5112
Longitude	-100.1918
Altitude MSL (m)	300
Frequency (MHz)	9397
Wavelength (cm)	3.22
PRF (Hz)	2500
Pulse Width (μs)	0.25
Beamwidth ($^{\circ}$)	0.88
Gate Spacing (m)	37
Unambiguous Range (km)	62.456
Nyquist Velocity ($m s^{-1}$)	19.14

Table 2: Specifications of the aft and fore P3 radars as operated on 17 May 2019.

P3 Specifications	
Polarization	Linear
Altitude MSL (m)	~2200
Frequency (MHz)	9368
Wavelength (cm)	3.22
Dual PRF Ratio	3/2
Pulse Width (μ s)	18.1
Beamwidth ($^{\circ}$)	2
Gate Spacing (m)	75
Unambiguous Range (km)	54.016
Nyquist Velocity (m s^{-1})	44.4

Table 3: Analysis times of the P3 legs in format HH:MM:SS. The (L) or (R) indicates the positioning of the storm relative to the aircraft during that leg.

P3 Leg Number	Time (UTC)
1	22:57:28 – 23:02:11 (R)
2	23:05:36 – 23:09:40 (L)
3	23:12:12 – 23:16:47 (R)
4	23:19:39 – 23:23:04 (L)
5	23:25:49 – 23:29:47 (R)
6	23:32:13 – 23:37:46 (R)
7	23:50:50 – 23:57:20 (L)
8	00:01:38 – 00:06:36 (R)
9	00:09:11 – 00:14:12 (L)
10	00:17:44 – 00:22:08 (R)
11	00:25:23 – 00:29:35 (L)
12	00:34:09 – 00:38:54 (R)

Table 4: Data on all of the tornadoes that occurred within the analysis period, where PL = Path Length and MW = Max Width.

Tornado #	EF	Segment	Time (UTC)	Start Lat, Lon	PL (mi)	MW (yd)
1	2	S1	22:55 – 23:01	40.203, -100.76	6	350
2	0	S2	23:10 – 23:15	40.345, -100.627	2.98	100
3	0	S2	23:32 – 23:33	40.47, -100.46	0.1	20
4	0	S2	23:45 – 23:46	40.53, -100.38	0.1	50
5	0	S2	23:55 – 23:57	40.56, -100.34	0.5	315
6	2	S3	23:58 – 00:00	40.581, -100.312	0.6	178
7	3	S3	00:05 – 00:09	40.612, 100.272	2.12	400
8	0	S3	00:12 – 00:13	40.673, -100.191	0.3	40
9	1	S3	00:15 – 00:33	40.7, -100.197	4.67	400

Table 5: Parameters for the perturbation surface-layer downdraft, damping, and surface flux parameterizations similar to Table 1 in Ziegler (2013a).

Parameter (units)	Symbol	Value
Surface layer w scale (m s ⁻¹)	w_{mix0}	0.5
Min surface layer w (m s ⁻¹)	w_{mix1}	-0.75
Min reflectivity (dBZ)	Z_0	20.0
Peak surface downdraft-core reflectivity (dBZ)	Z_{DDC}	50.0
Surface trajectory offset height (km)	H_0	0.01
Damping coefficient	c_d	0.2
Threshold $ w = W_0$ for surface damping (m s ⁻¹)	W_0	0.1
L_m value (m) for $w = W_0$	L_{m0}^+	5000
L_m value (m) for $w = -W_0$	L_{m0}^-	300
dL_m/dw (s) for $w > W_0$	L_w^+	2000
dL_m/dw (s) for $w < -W_0$	L_w^-	100
Min C_{m0} (m ⁻¹)	C_{min0}	7×10^{-5}
Max C_{m0} (m ⁻¹)	C_{max0}	2×10^{-4}
Threshold q_p (g kg ⁻¹)	q_{p0}	1

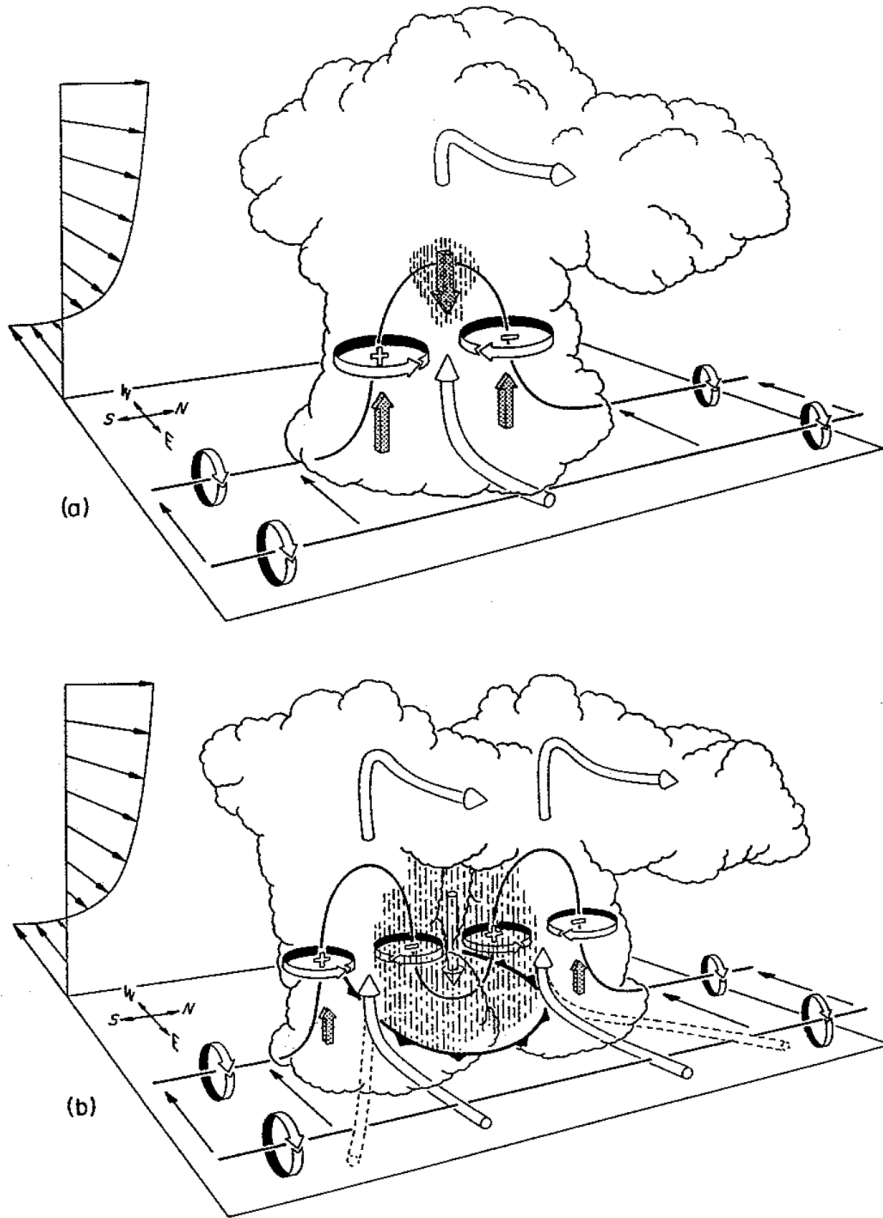


Figure 1: (Caption next page.)

Figure 1: Classic schematic on how vorticity generated from unidirectional environmental shear interacts with a single updraft (cylindrical arrows). Vortex lines are thin black arrows with sense of rotation given by the flat, white arrows. New forcing from updrafts / downdrafts shown by solid shaded arrows. (a) Initial perturbation upwards tilts the initially horizontal vortex line, creating cyclonic (anticyclonic) vertical vorticity on the southern (northern) flank of the storm. (b) As time progresses, the downdraft in the center of the storm tilts the vortex line downward resulting in storm splitting with a cyclonic / anticyclonic couplet associated with both cells. Figure from Klemp (1987).

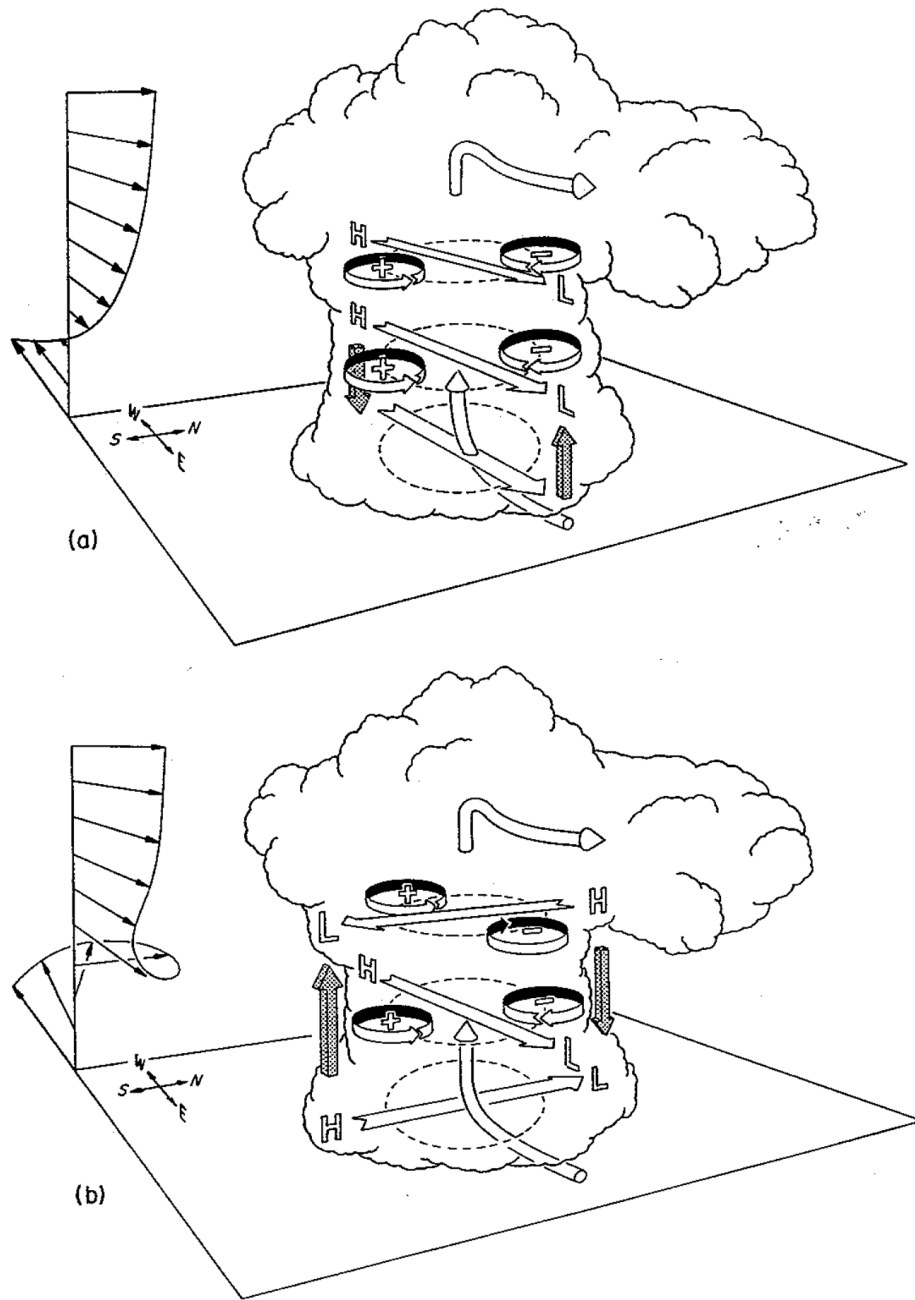


Figure 2: (Caption next page.)

Figure 2: (a) Areas of relative high and low pressure as well as cyclonic and anticyclonic vertical vorticity in the case of (a) linear environmental shear and (b) nonlinear environmental shear. Cylindrical white arrows show the updraft, flat white arrows represent the direction of the shear vector at that particular level, and thick shaded arrows illustrate the resultant pressure gradient force. Figure from Klemp (1987).

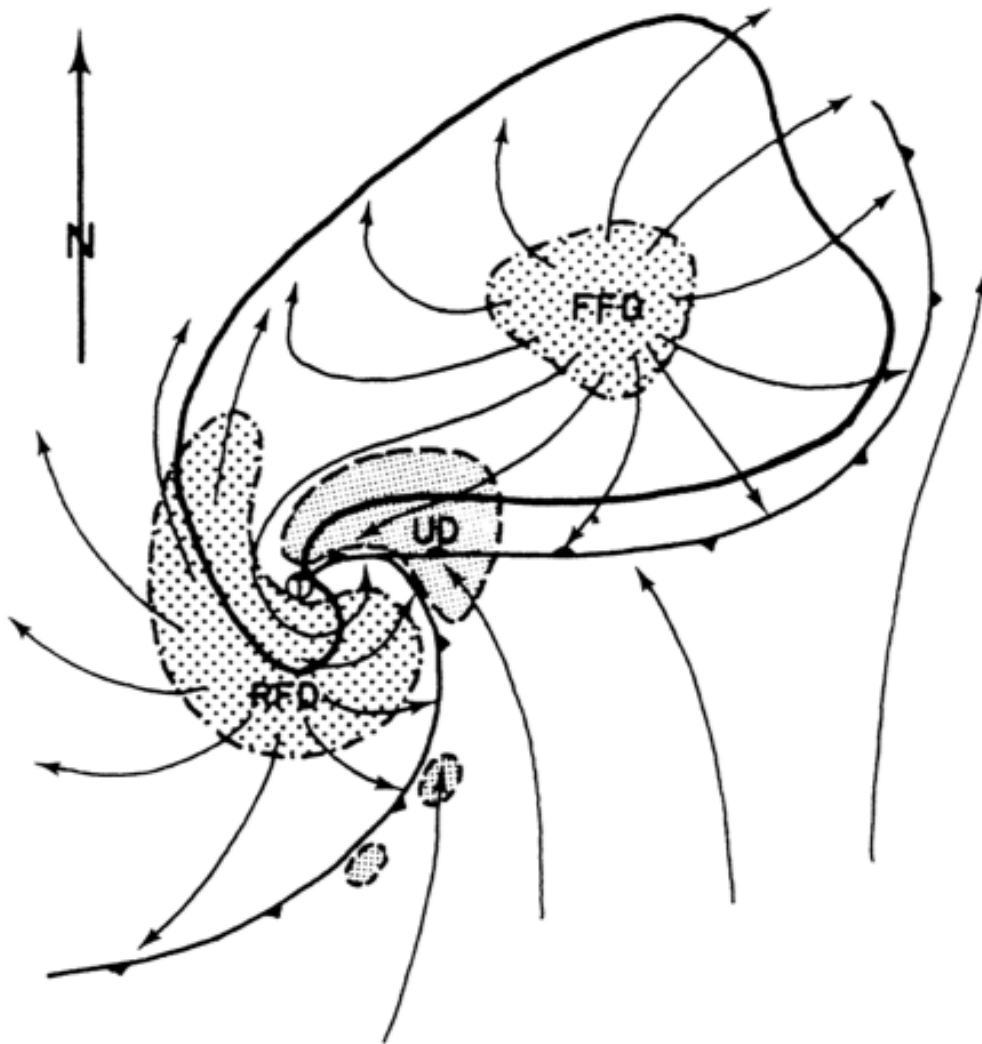


Figure 3: Top-down schematic of a supercell from Lemon and Doswell (1979). The updraft (UD), forward-flank downdraft (FFD), and rear-flank downdraft (RFD) are annotated and shaded. Arrows represent streamlines and the solid line represents a typical radar reflectivity outline. The location of the outflow boundaries are also noted.

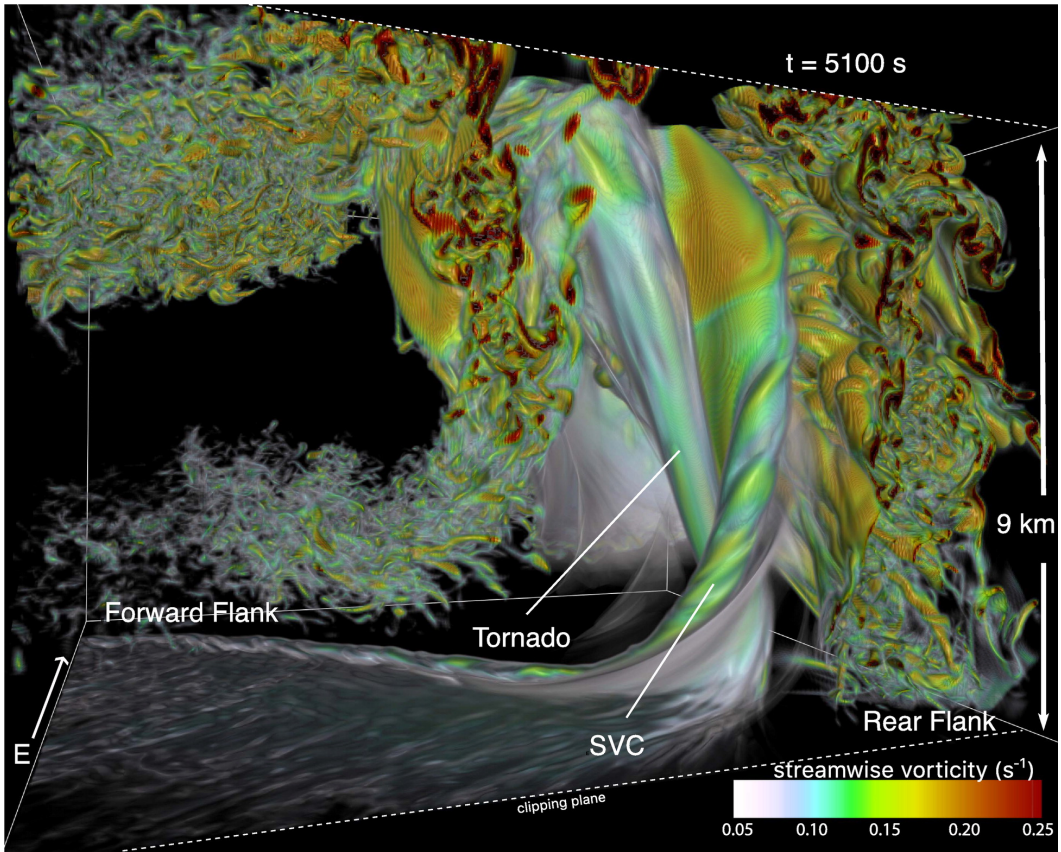


Figure 4: Volume rendering of streamwise vorticity from Orf et al. (2017). Locations of important features within the supercell, including the SVC, are noted in the figure.

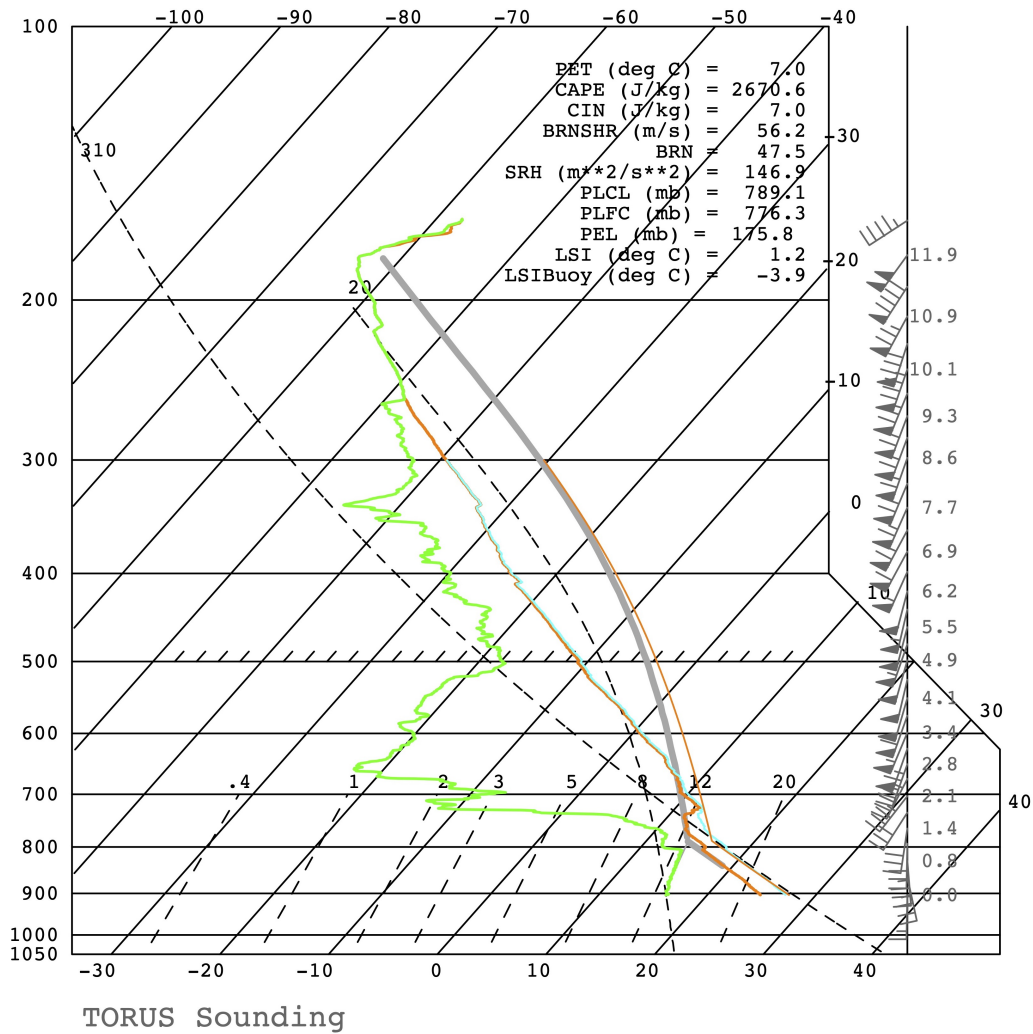


Figure 5: Sounding released from a far-field vehicle on 17 May 2019 at 23:02:30 UTC. Green, thick orange, and light blue line indicates the dewpoint temperature, temperature, and virtual temperature, respectively. Gray line and thin orange line represent lifted parcel path using surface temperature and surface virtual temperature, respectively. Full, half wind barb, and flag indicates 10, 5, and 50 kts, respectively, with numbering next to the wind barb showing recorded height in km. Values in top right corner show calculated sounding parameters.

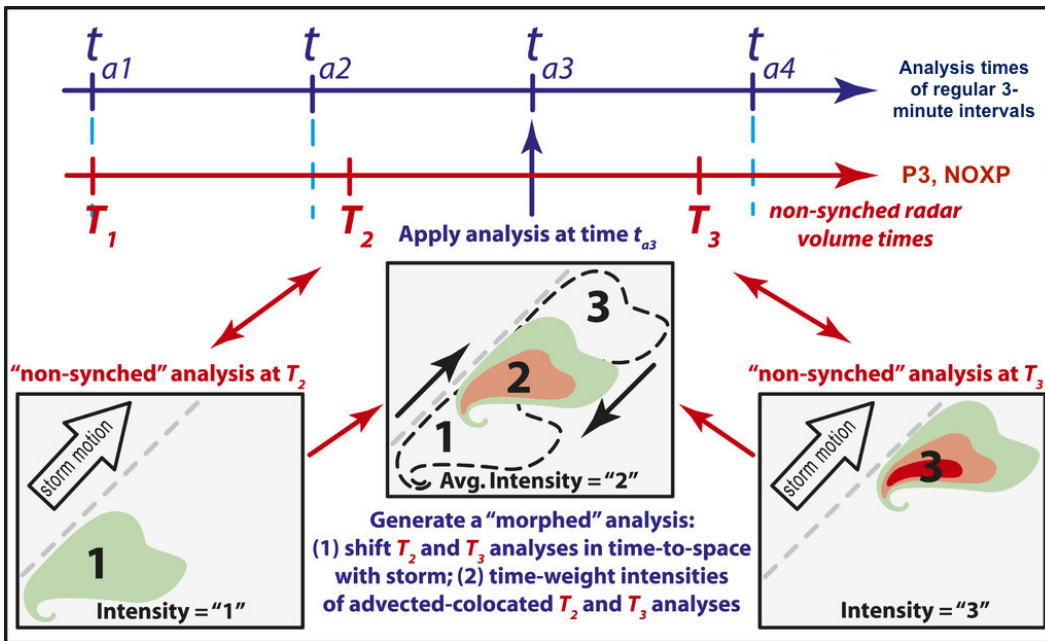


Figure 6: Figure taken from Ziegler (2013b) depicting the time-morphing algorithm used to map two consecutive non-synched radar analyses at T_2 and T_3 to a new analysis time t_{a3} .

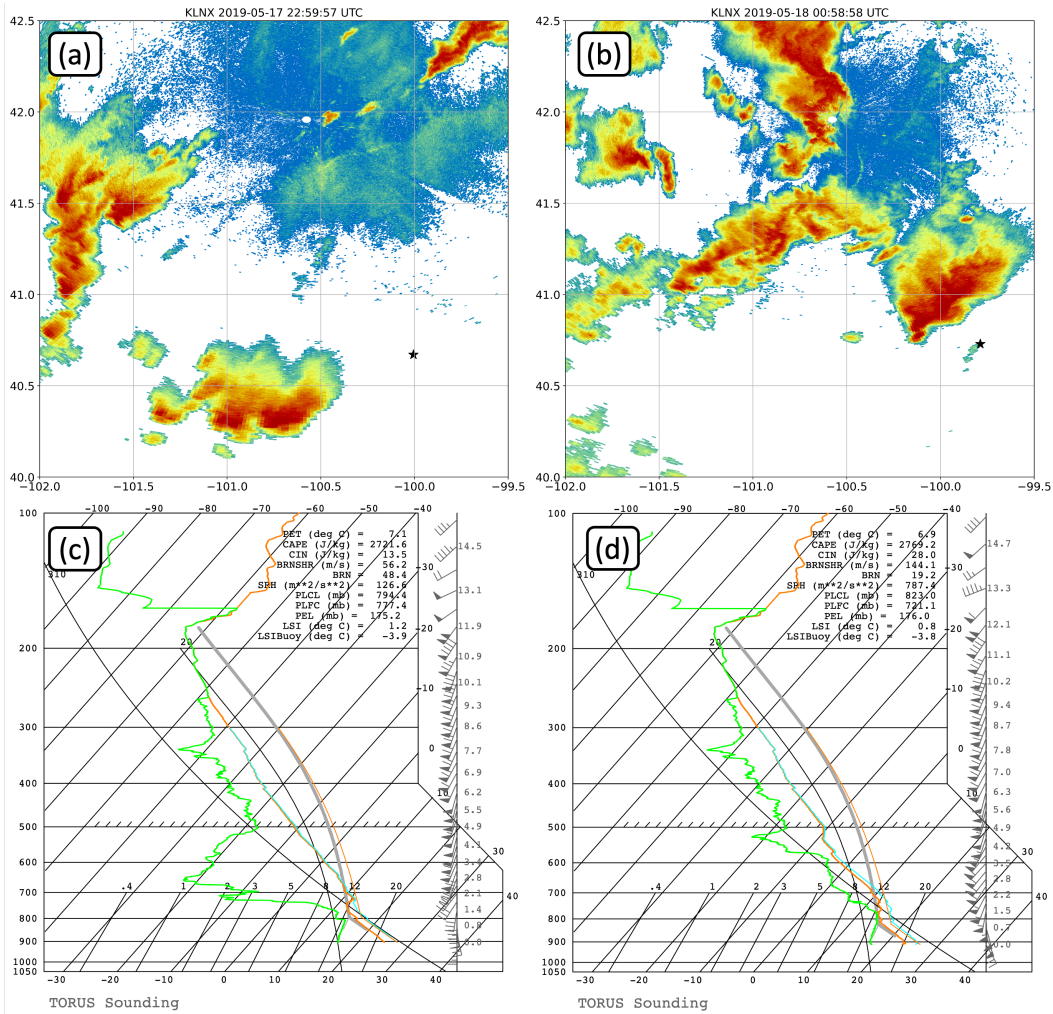


Figure 7: Panels (a) and (b) show the location of the sounding indicated by the black star from 17 May 23:02:30 UTC and 18 May 00:57:05 UTC, respectively, along with the closest corresponding radar image from KLNX. Panels (c) and (d) are as in Fig. 5 showing soundings at 23:02:30 UTC and 00:57:05 UTC.

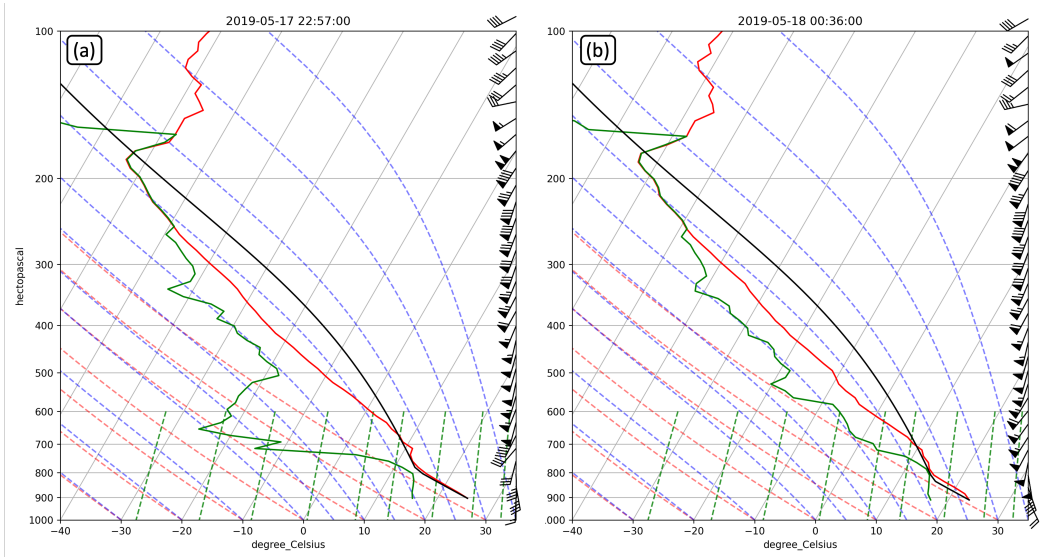


Figure 8: Panels (a) and (b) show the linearly interpolated sounding with a $\Delta z = 0.25$ km at 17 May 22:57 UTC and 18 May 00:36 UTC. The red and green lines indicate temperature and dewpoint temperature while the black line indicates a lifted surface parcel. Wind barbs are given on the right hand side of the figures.

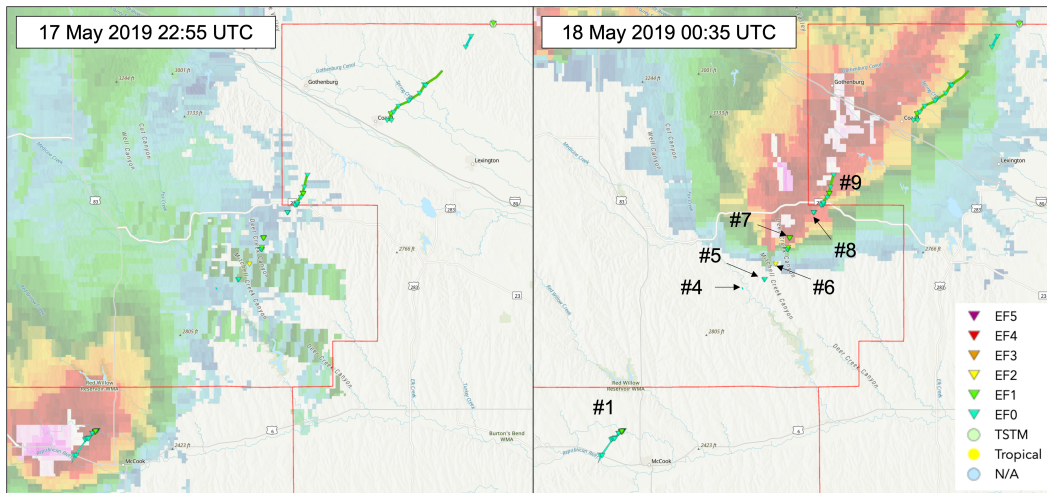


Figure 9: Damage track of the tornadoes on 17 May 2019 with the radar image from 22:55 UTC and 00:35 UTC overlaid underneath on the left and right panels, respectively (images from the Damage Assessment Toolkit, DAT; <https://apps.dat.noaa.gov/stormdamage/damageviewer/>). The triangles indicate each individual damage indicator while the lines represent the approximate track of a single tornado. The numbers in the right panel correspond to the tornado numbers in Table 4 (tornado #2 and #3 are not marked within the DAT).

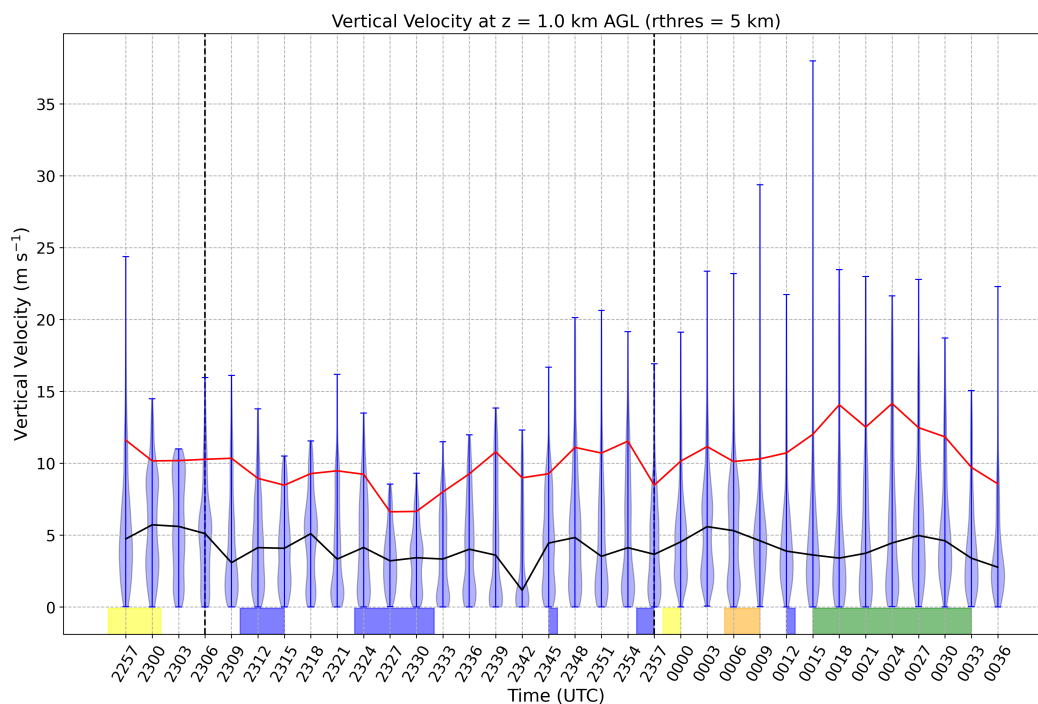


Figure 10: Violin plots showing the distribution of positive vertical vorticity within 5 km of the 1 km AGL circulation. The bottom and top of the violin plot show the extrema of the distribution while the black and red lines show the median and 95th percentile of the data. The dotted black vertical lines represent the separation between S1 / S2 and S2 / S3. The blue, green, yellow, and orange shading represent the times of EF-0, EF-1, EF-2, and EF-3 tornadoes.

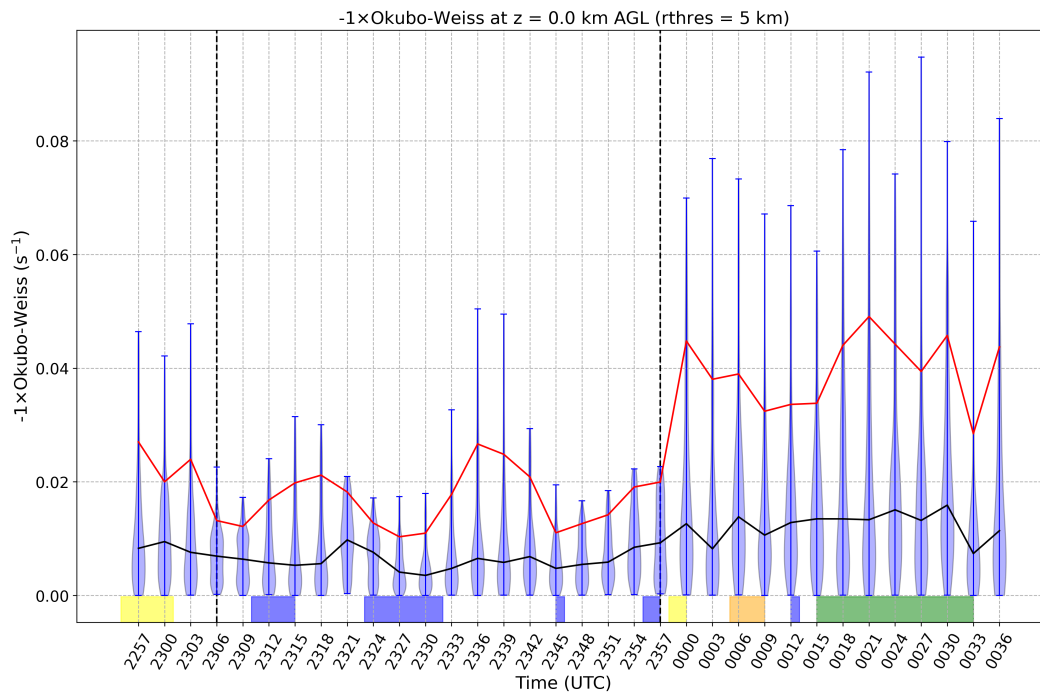


Figure 11: Similar to Fig. 10 except for the negative of the Okubo-Weiss parameter at the surface.

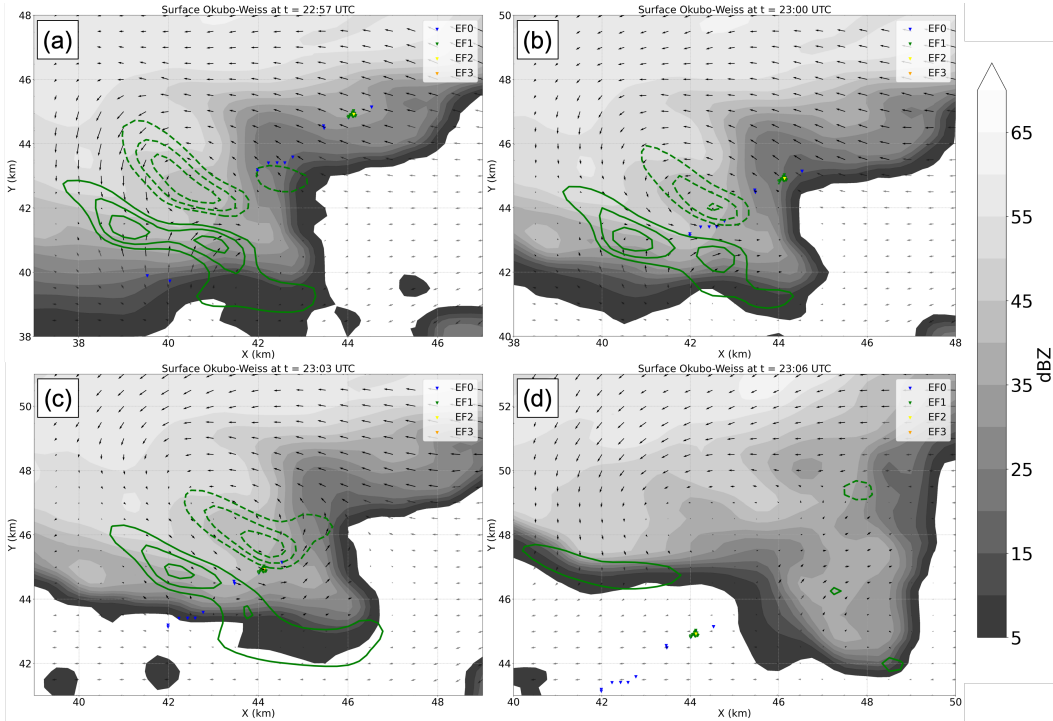


Figure 12: Gray shaded gridded reflectivity and multi-Doppler wind synthesis horizontal wind vectors at 0.0 km AGL at (a) 22:57, (b) 23:00, (c) 23:03, and (d) 23:06 UTC. Black wind vectors represent those obtained by wind syntheses while gray wind vectors are those obtained by smoothing between wind syntheses and the background wind field. Colored triangles represent damage indicators. Green contours are Okubo-Weiss values contoured starting at $\pm 0.02 \text{ s}^{-1}$ every 0.01 s^{-1} (dashed contours represent negative values).

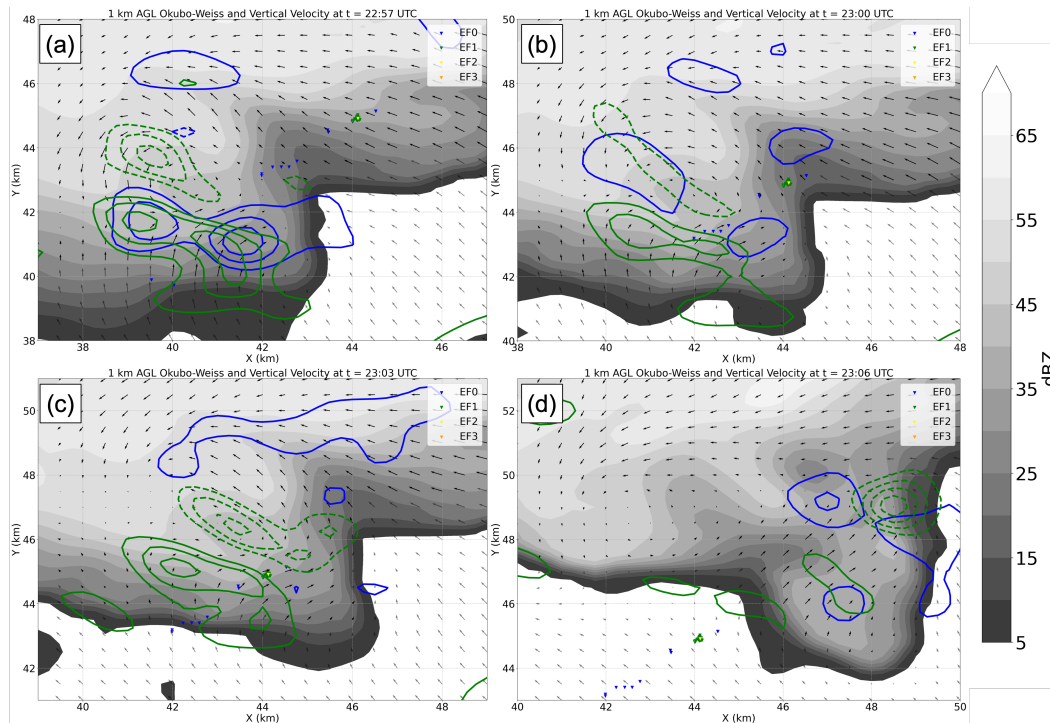


Figure 13: As in Fig. 12 but for 1 km AGL. Additionally, blue lines represent vertical velocity contours starting at $\pm 10 \text{ m s}^{-1}$ every 5 m s^{-1} (dotted blue contours represent negative values).



Figure 14: Sequence of images depicting the tilt of the tornado east of McCook, NE (tornado #1 in Table 4). Images are screenshots from video: <https://www.youtube.com/watch?v=J5NYzRx5nhc>.

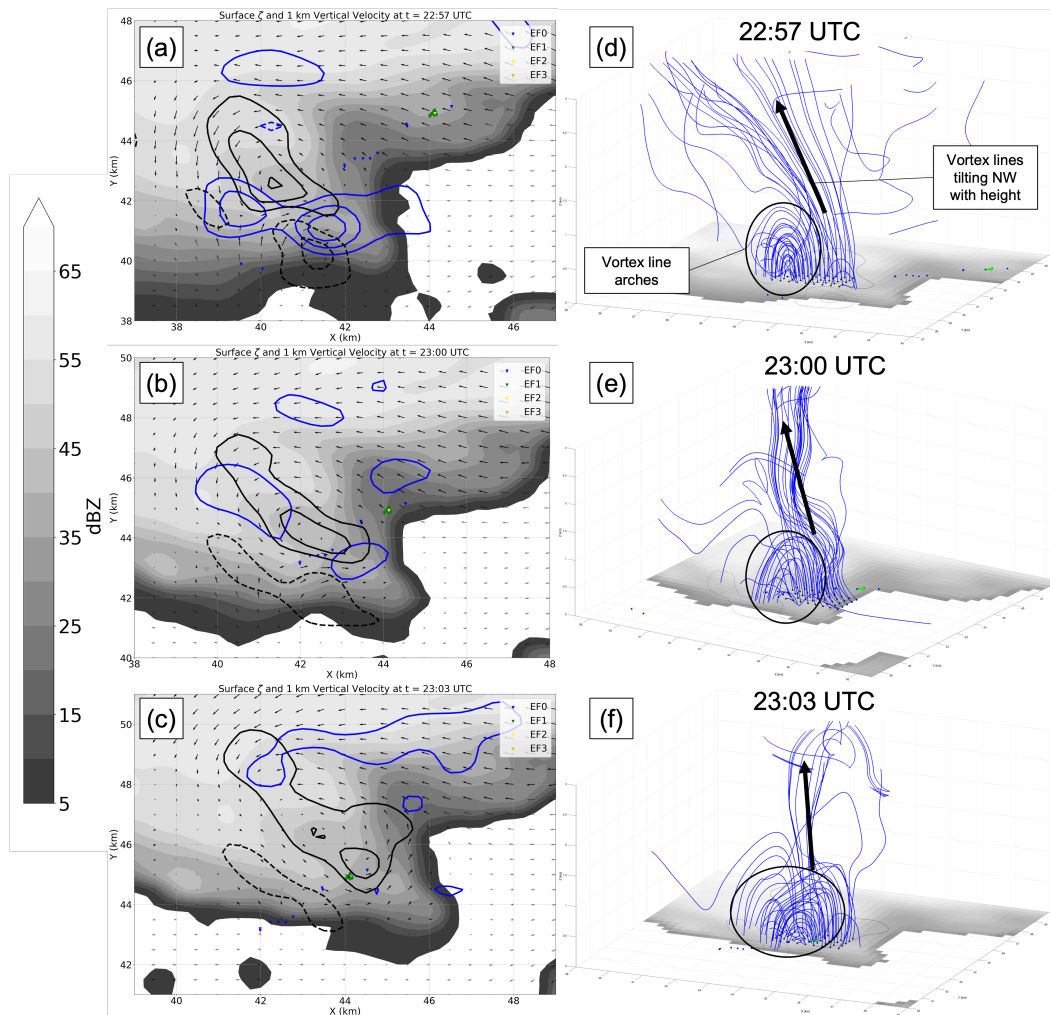


Figure 15: (Caption next page.)

Figure 15: (a–c) Gray shaded surface reflectivity with black contours of surface vertical vorticity starting from $\pm 0.01 \text{ s}^{-1}$ every 0.01 s^{-1} and blue contours of 1 km AGL vertical velocity starting at $\pm 10 \text{ m s}^{-1}$ every 5 m s^{-1} (dashed contours represent negative values) at 22:57, 23:00, and 23:03 UTC. Damage indicators are marked by the colored triangles. (d–f) Vortex lines (blue) at surface starting locations marked by black squares. Black circles represent clustering of vortex line arches and black arrows represent tilting vortex lines. Damage indicators are marked by colored squares, gray shading is gridded surface reflectivity, and solid / dashed black contours represent surface vertical vorticity as in panels (a–c).

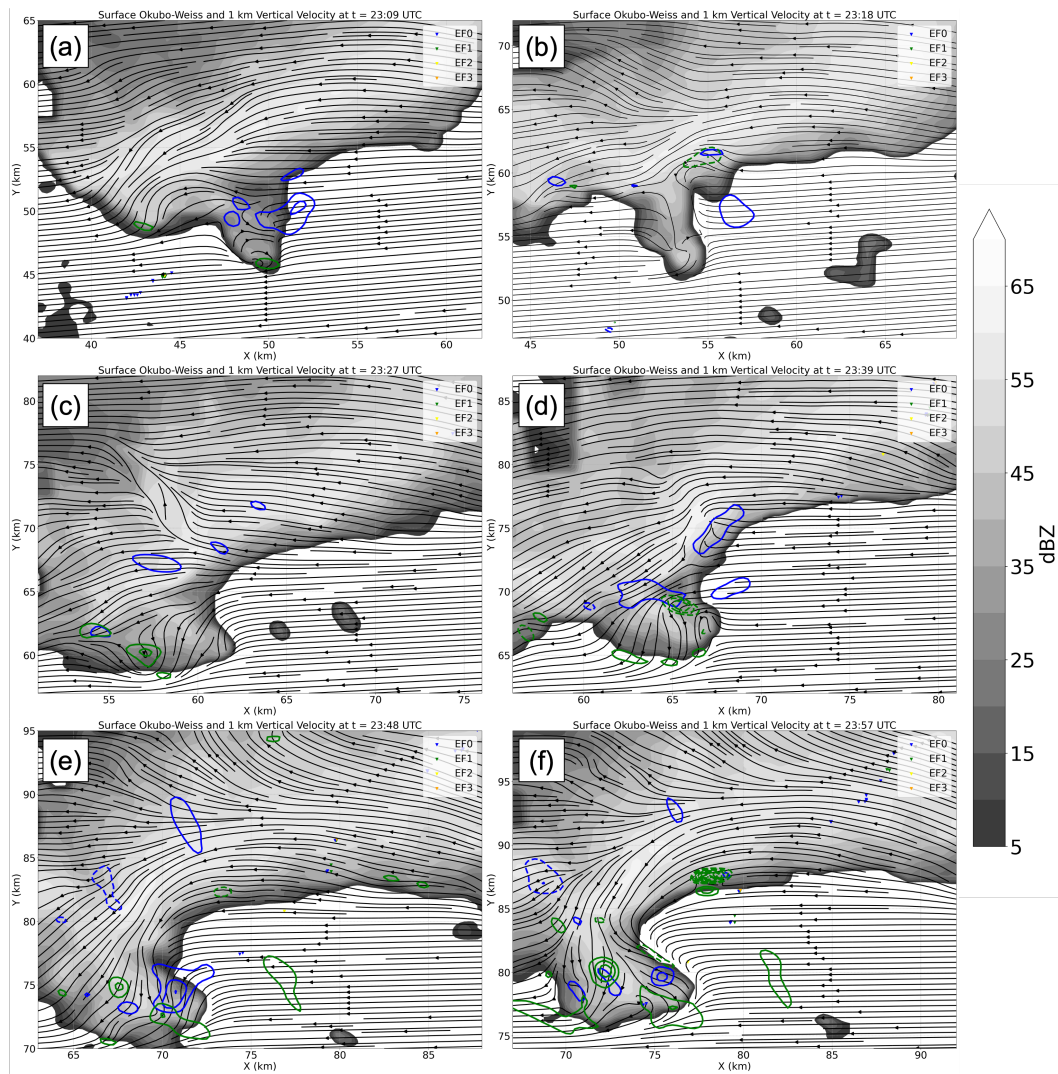


Figure 16: (Caption next page.)

Figure 16: Streamline analysis via surface wind syntheses at (a) 23:09, (b) 23:18, (c) 23:27, (d) 23:39, (e) 23:48, and (f) 23:57 UTC with the thickness of the streamline proportional to the wind speed. Gridded surface reflectivity is gray shaded and contours of surface OW and 1 km vertical velocity are contoured in green and blue, respectively (values of contours are as in Fig. 13). Damage indicators are denoted with colored triangles.

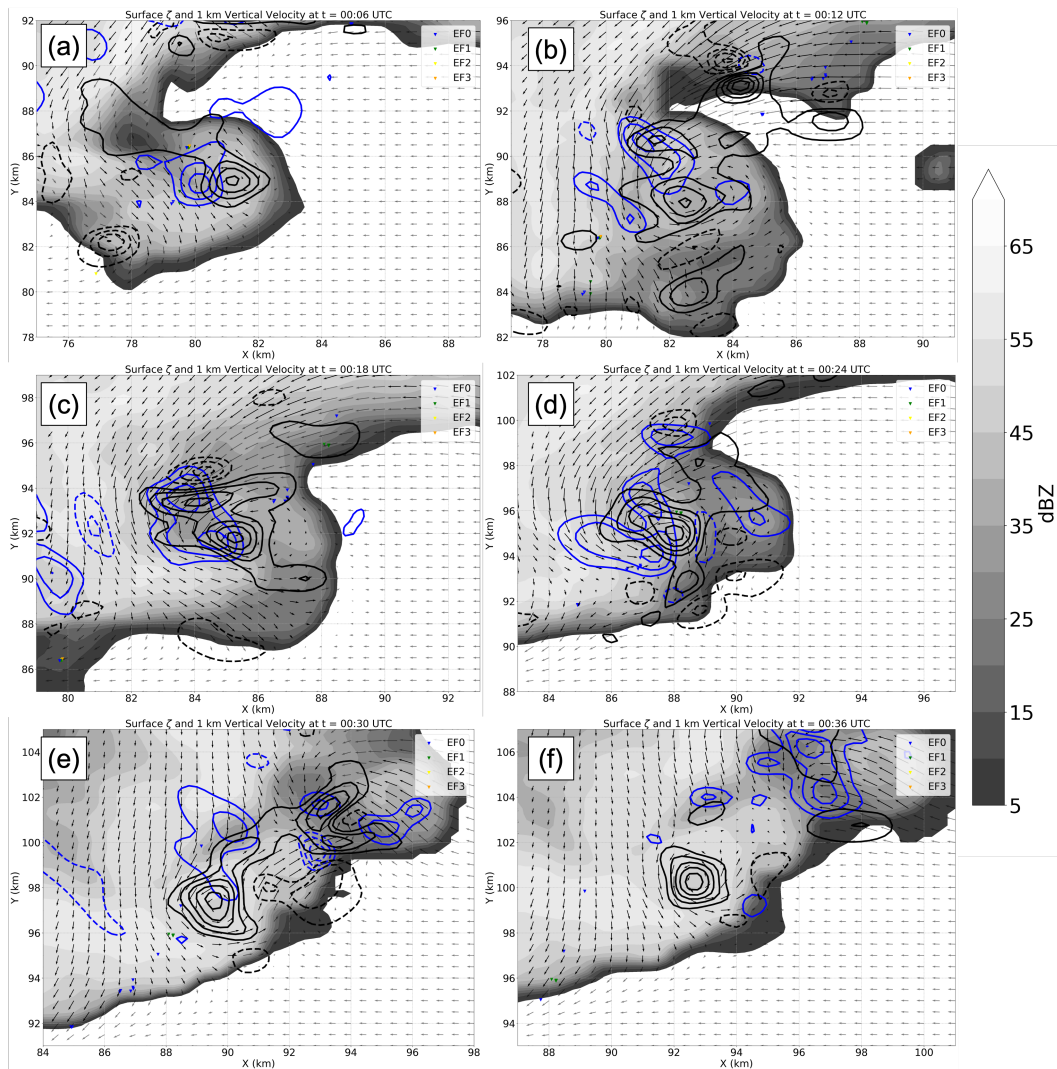


Figure 17: As in Fig. 15 for (a) 00:06, (b) 00:12, (c) 00:18, (d) 00:24, (e) 00:30, and (f) 00:36 UTC.

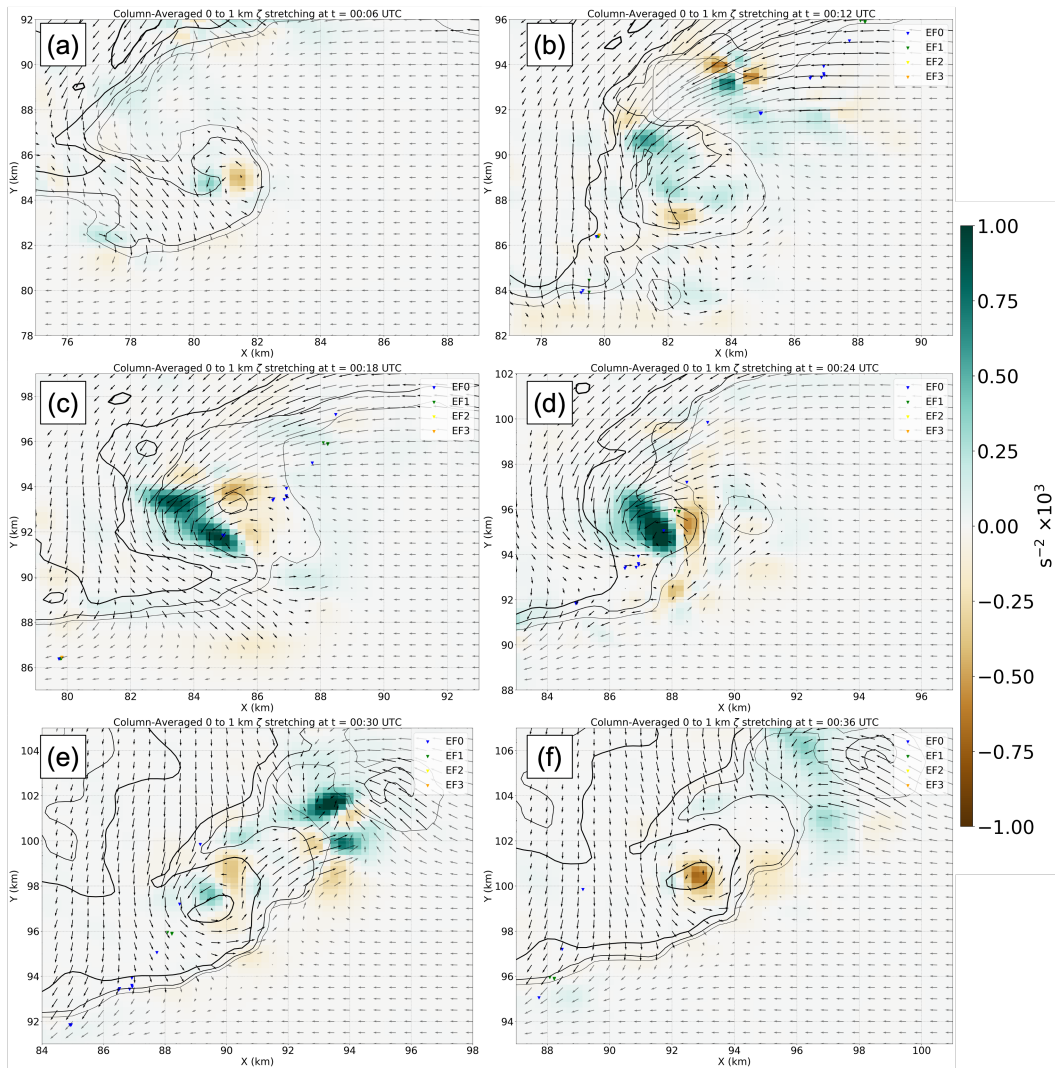


Figure 18: Column-averaged vertical vorticity stretching (shaded) from the surface to 1 km AGL (5 total vertical grid levels) for the same analysis times as Fig. 17. Reflectivity is indicated by black contours starting from 5 dBZ every 5 dBZ. Arrows indicated surface horizontal wind vectors and damage indicators are represented by colored triangles.

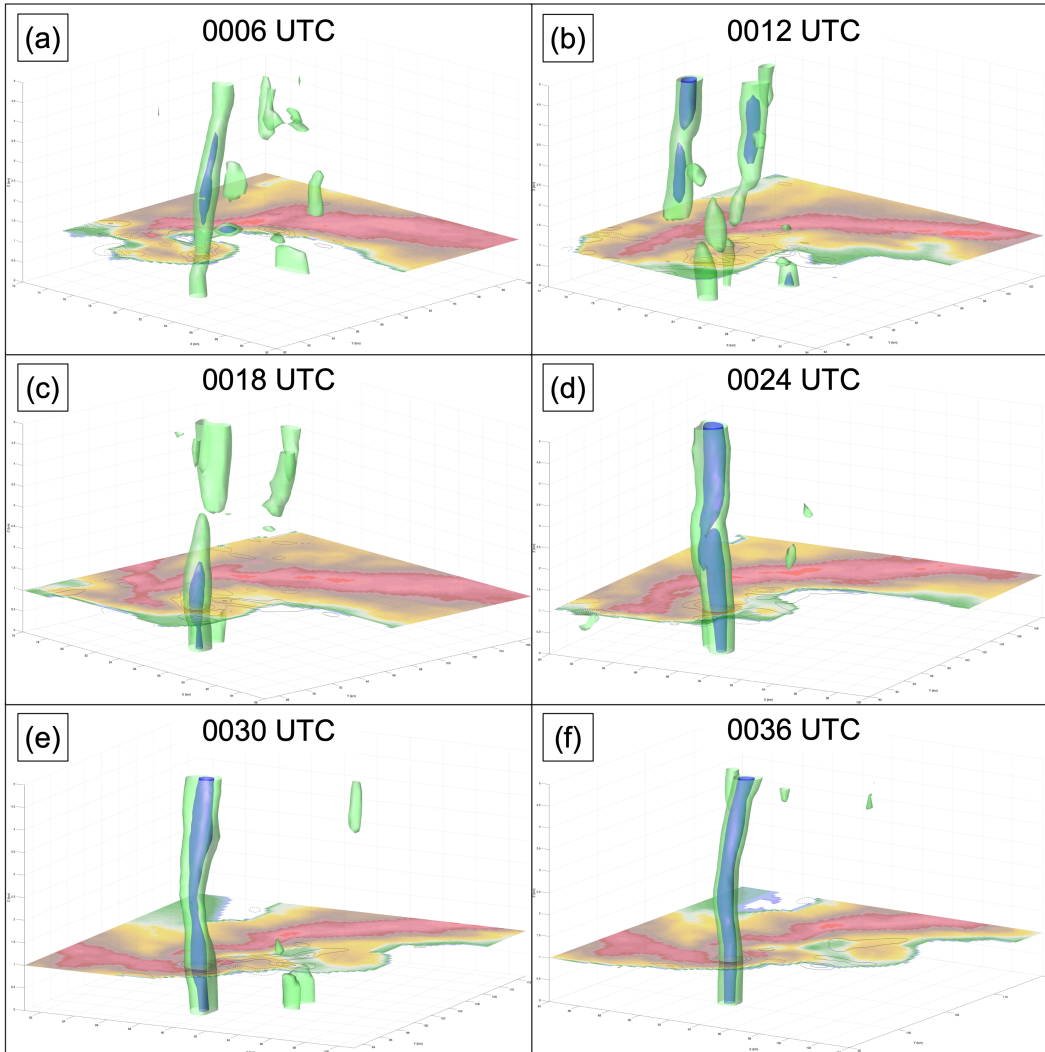


Figure 19: Isosurfaces of vertical vorticity representing values of 0.03 s^{-1} (green) and 0.05 s^{-1} at the same analysis times as Fig. 17 and 18. 1 km reflectivity is color shaded. 1 km vertical vorticity is contoured in black every 0.01 s^{-1} , with dotted contours representing negative values.

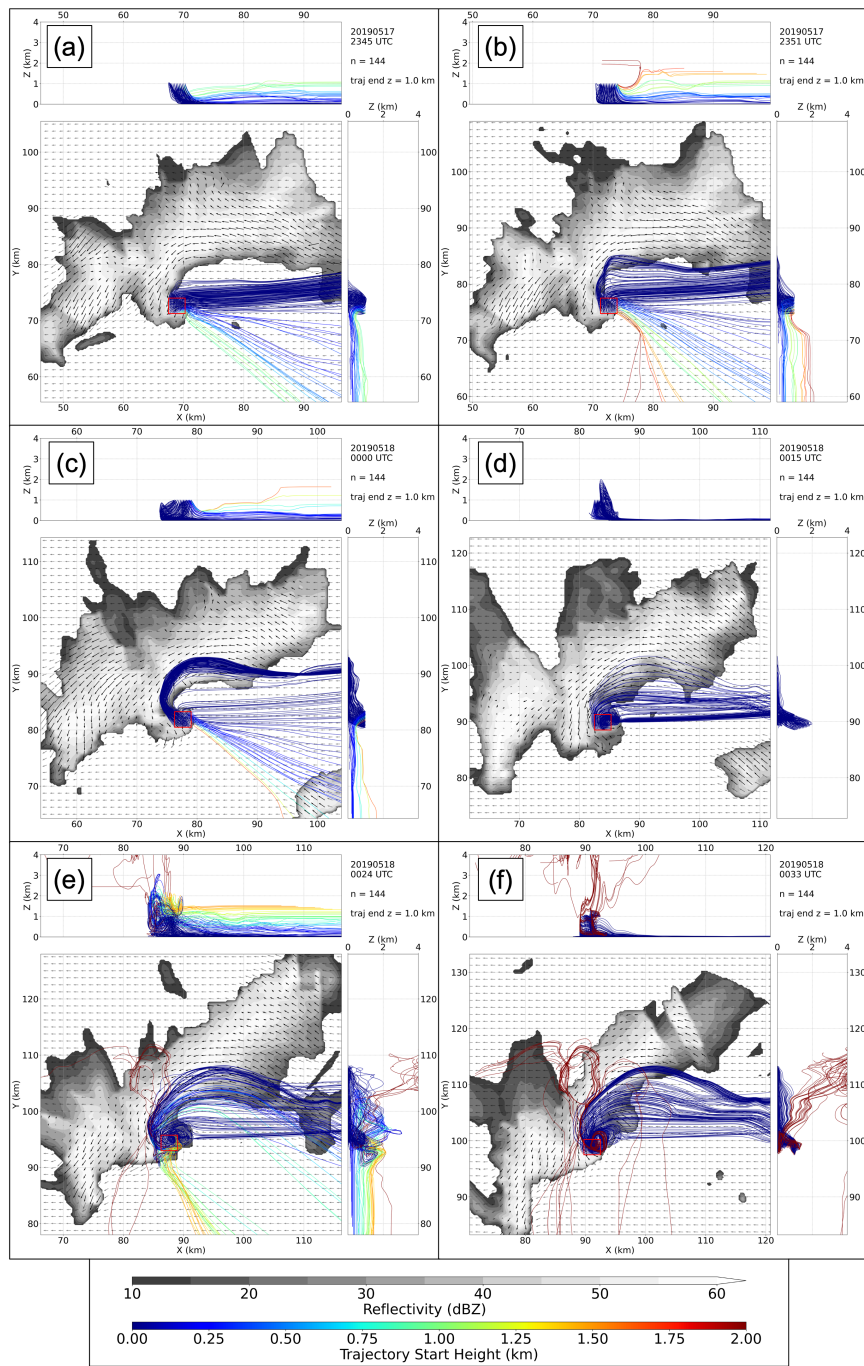


Figure 20: (Caption next page.)

Figure 20: Backward trajectories originating from 1 km AGL around a 1.5×1.5 km box around the low-level mesocyclone (red box) at (a) 23:45, (b) 23:51, (c) 00:00, (d) 00:15, (e) 00:24, and (f) 00:33 UTC. Middle figure in each panel shows reflectivity (gray-shaded) with arrows depicting surface horizontal wind vectors. Each backward trajectory is indicated by a colored line, with the color representing the starting height of the trajectory. Top figure in each panel gives an X-Z plane visualization of trajectories, and right figure gives a Y-Z plane visualization.

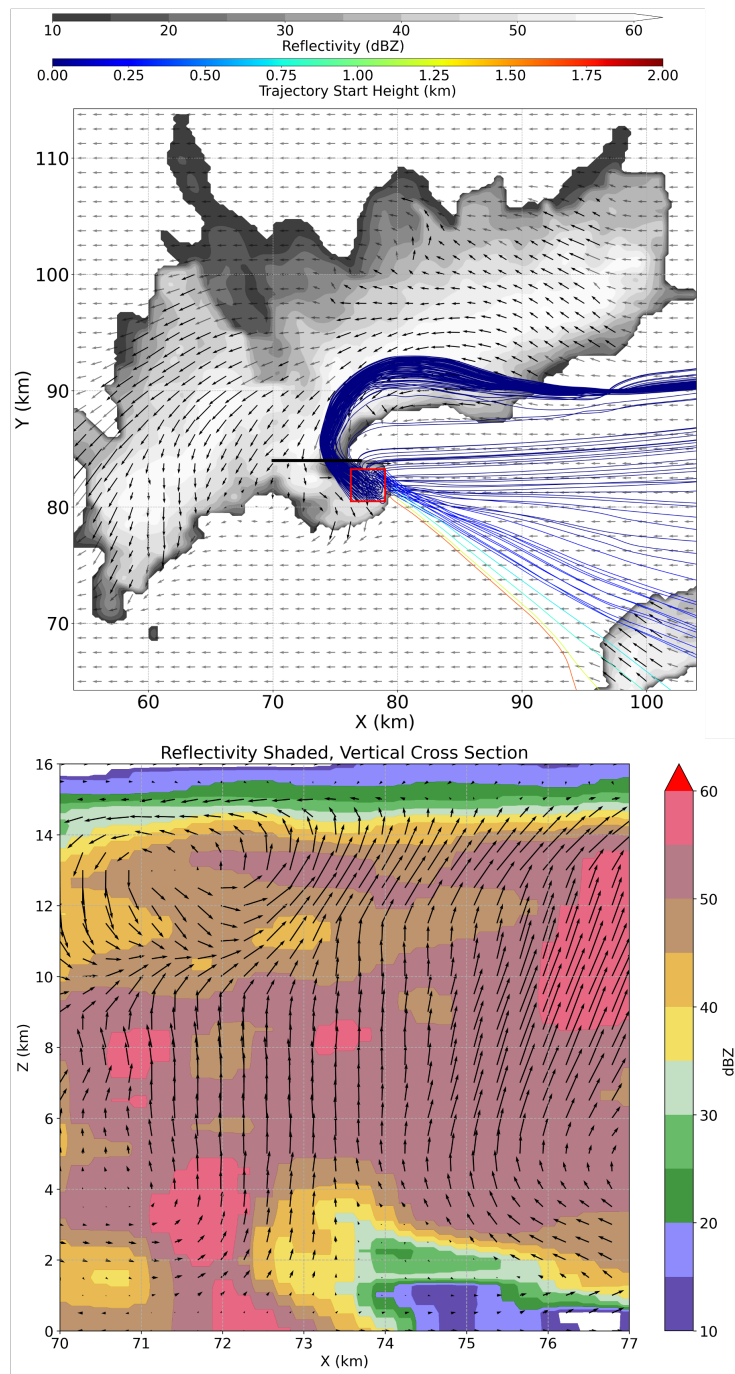


Figure 21: Top figure similar to Fig. 20 for 00:00 UTC, with the additional black line denoting the location of the cross section. Bottom panel shows the cross section with shaded reflectivity with arrows denoting winds in the cross-sectional plane.

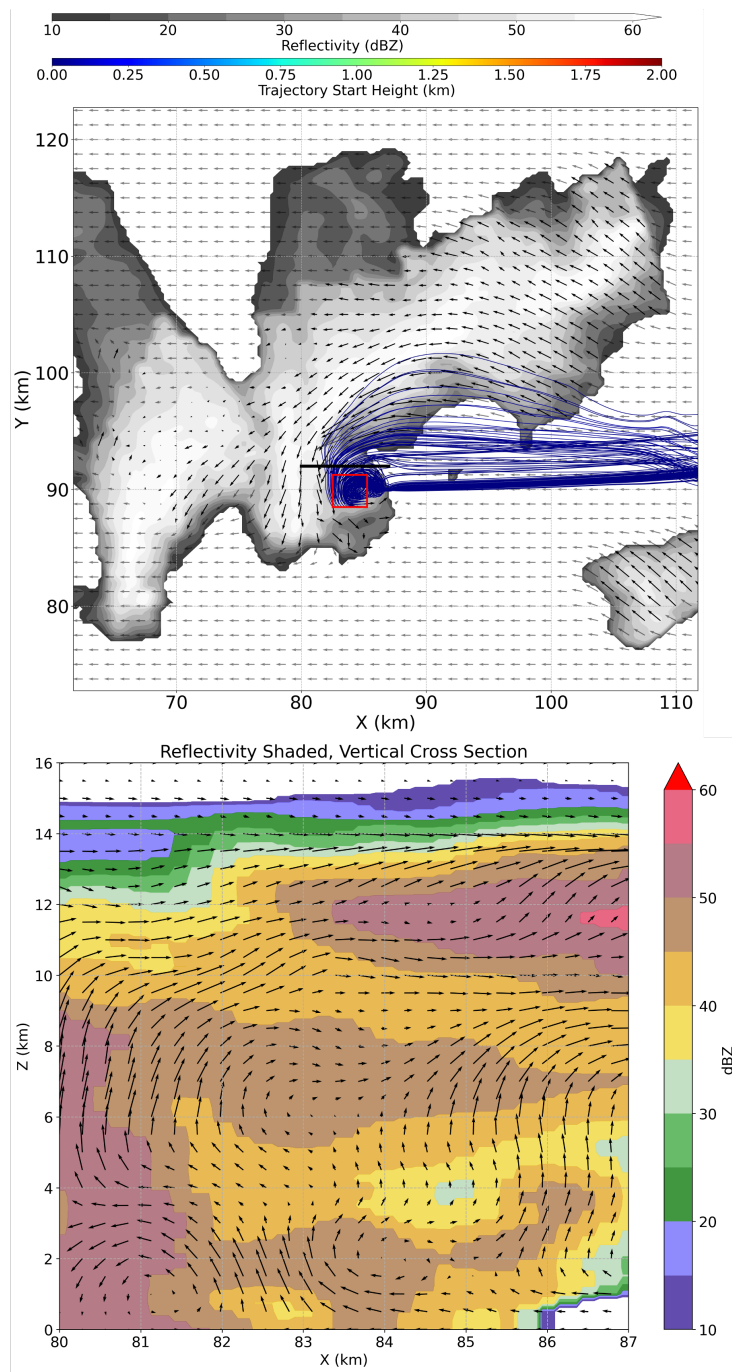


Figure 22: Similar to Fig. 21 but for 00:15 UTC.

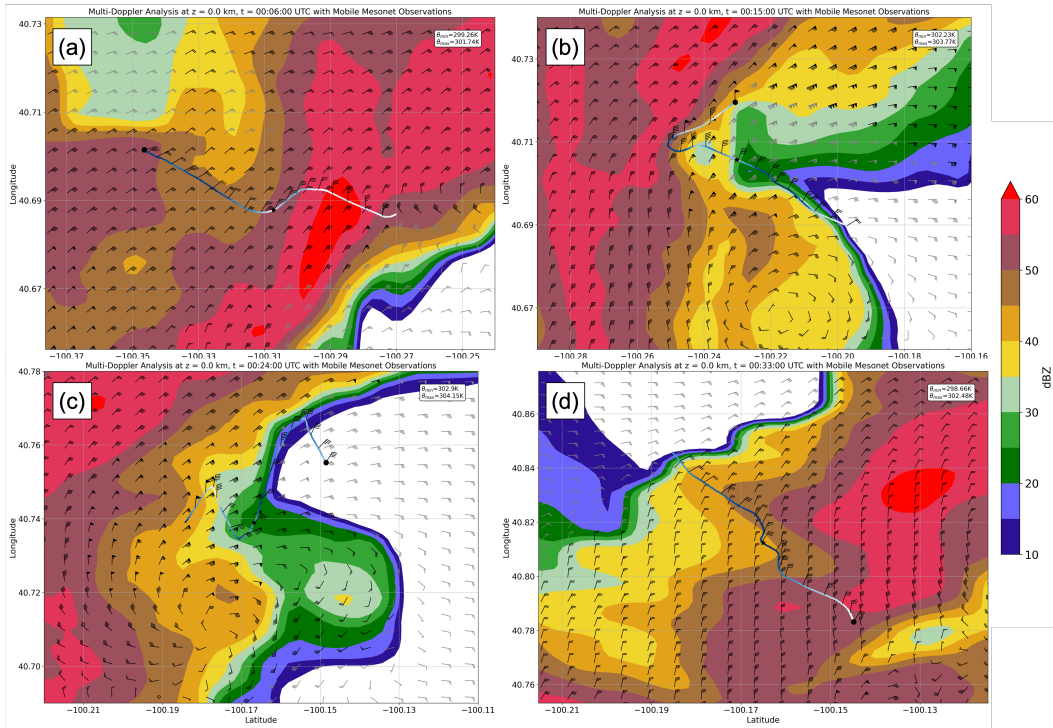


Figure 23: Observed mobile mesonet surface winds compared to the surface winds derived from multi-Doppler wind synthesis at (a) 00:06, (b) 00:15, (c) 00:24, and (d) 00:33 UTC. The gridded surface winds from analysis are indicated by smaller wind barbs superimposed on color-shaded reflectivity. Observed mobile mesonet winds are given by slightly larger wind barbs along the blue-shaded line — the line indicates the location of the mesonet vehicle which is spatially-corrected for storm motion while the color of the line represents potential temperature, with deeper blue colors indicating cooler θ values. Observed wind barbs are plotted every 20th measurement. The black dot indicates the Mobile start of the mesonet track and the black star represents the measurement taken at the analysis time.

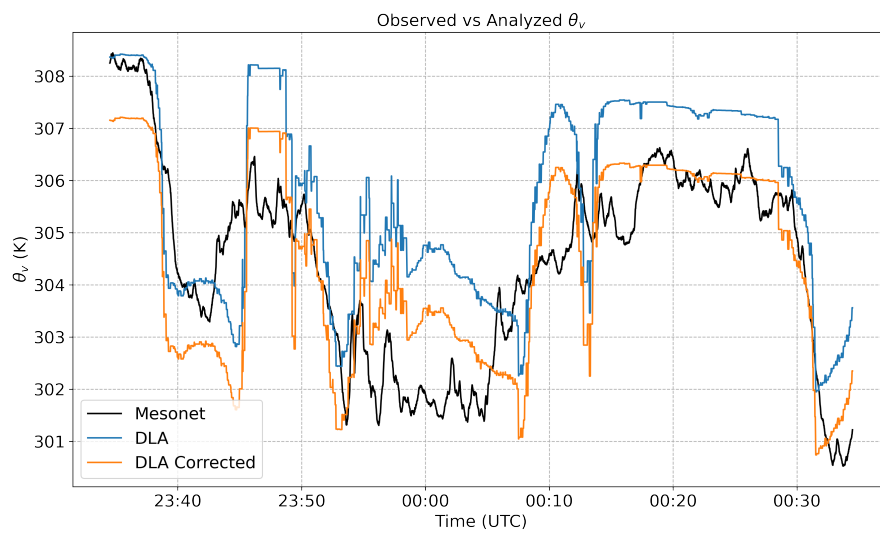


Figure 24: Time series of θ_v from the mobile mesonet (black) and closest grid point in the DLA (blue). The orange line represents the DLA θ_v corrected by the median bias.

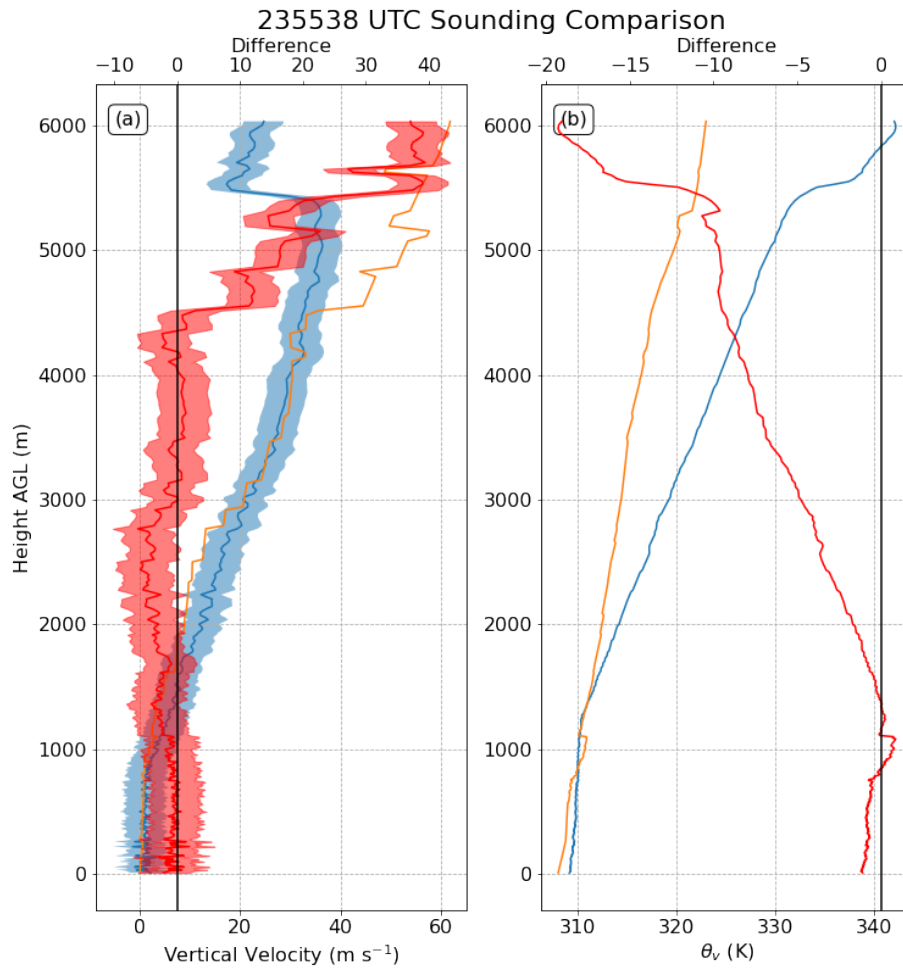


Figure 25: (a) Comparison of vertical velocity from the sounding (blue) launched at 23:55:38 UTC using an assumed constant balloon ascent rate of 5 m s^{-1} and an error bar of 4 m s^{-1} (transparent shading). The orange line is the corresponding vertical velocity from the wind synthesis, and the red represents the wind synthesis minus the sounding vertical velocity with error bar shaded. (b) θ_v from the sounding, with colors corresponding to that of panel (a).

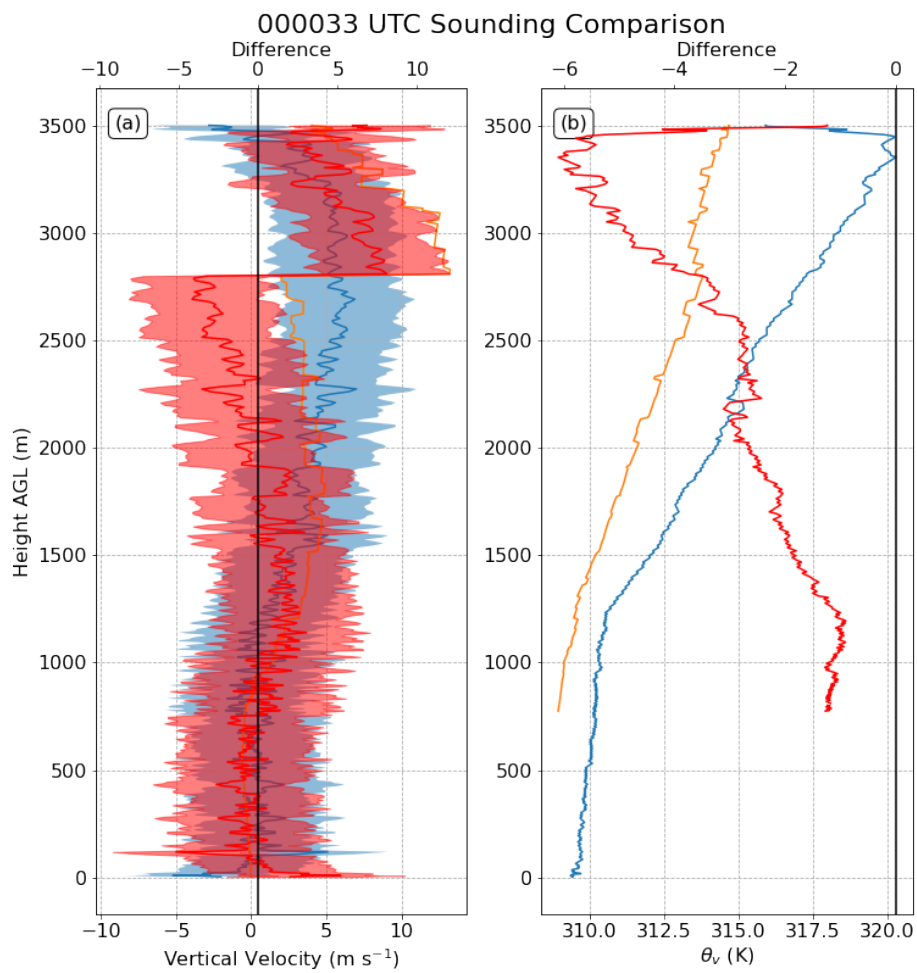


Figure 26: Same as Fig. 25 but for the sounding launched at 00:00:33 UTC.

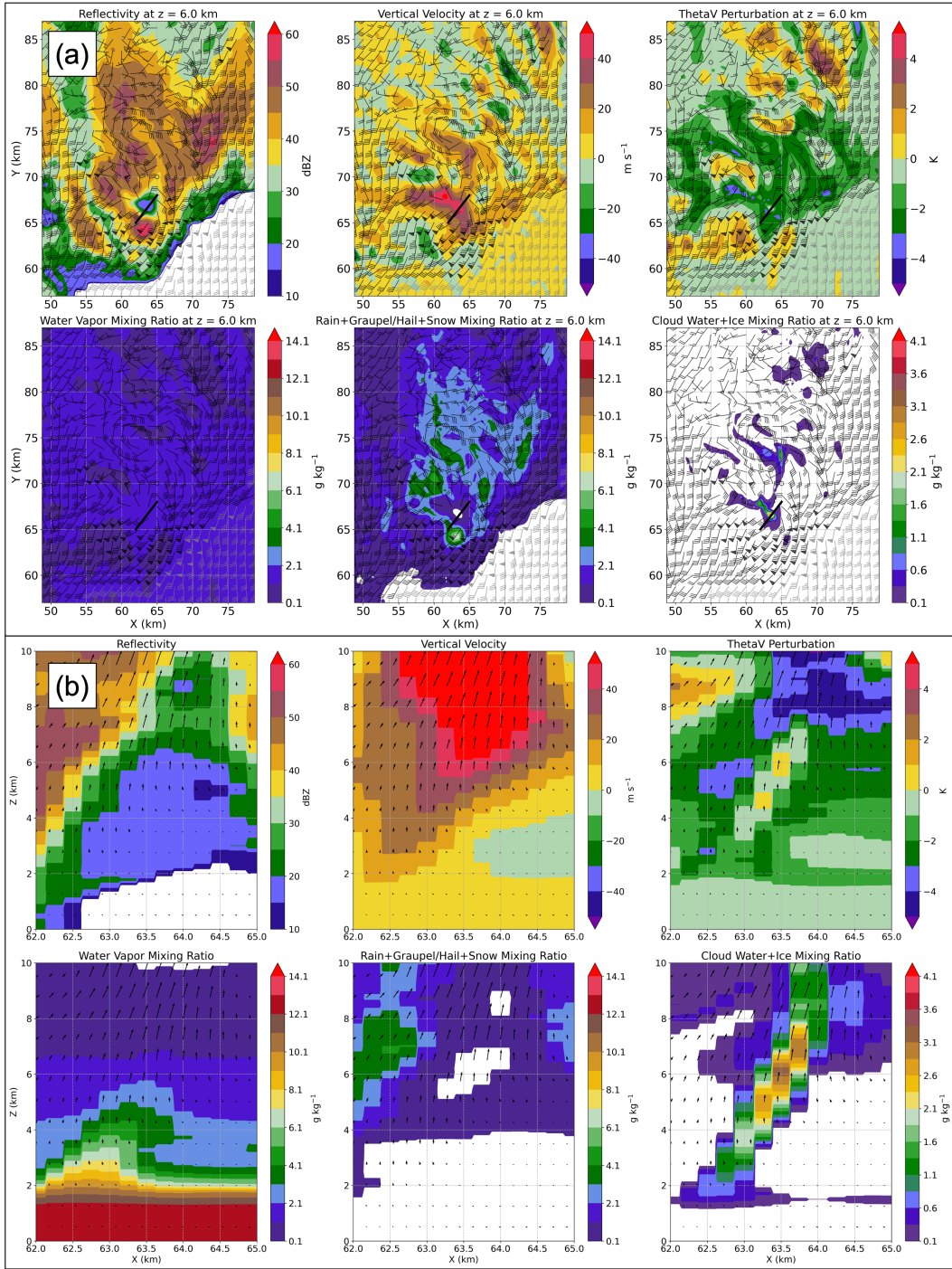


Figure 27: (Caption next page.)

Figure 27: (a) Shaded plots of reflectivity, vertical velocity, θ_v perturbation, water vapor mixing ratio, rain / graupel / hail / snow mixing ratio, and cloud water / cloud ice mixing ratio with wind barbs at 6 km AGL at 23:30 UTC. The solid black line indicates the location of the cross section shown in panel (b) which shows the same variables in the same order as (a).

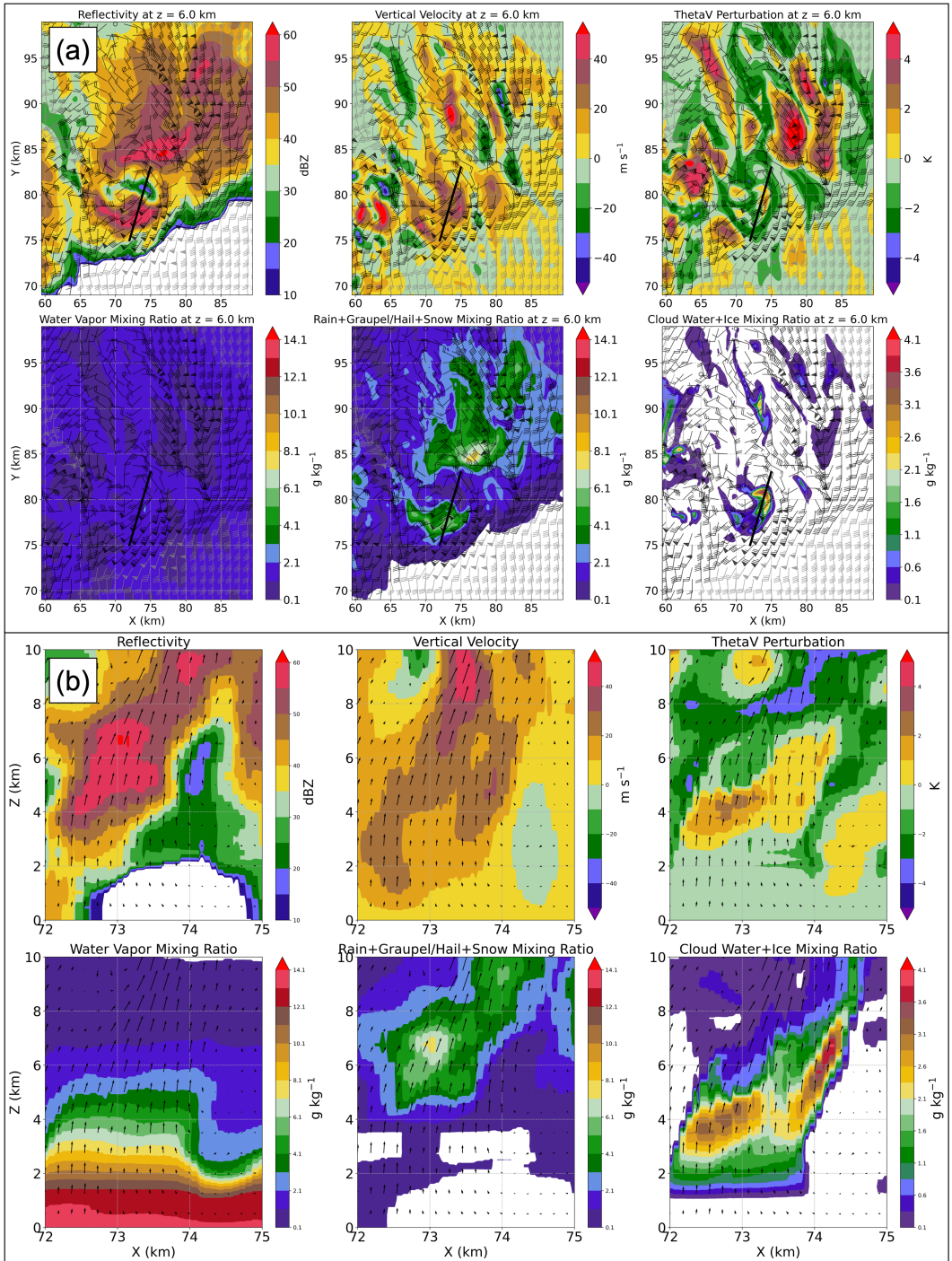


Figure 28: Same as in Fig. 27 but for 23:51 UTC.

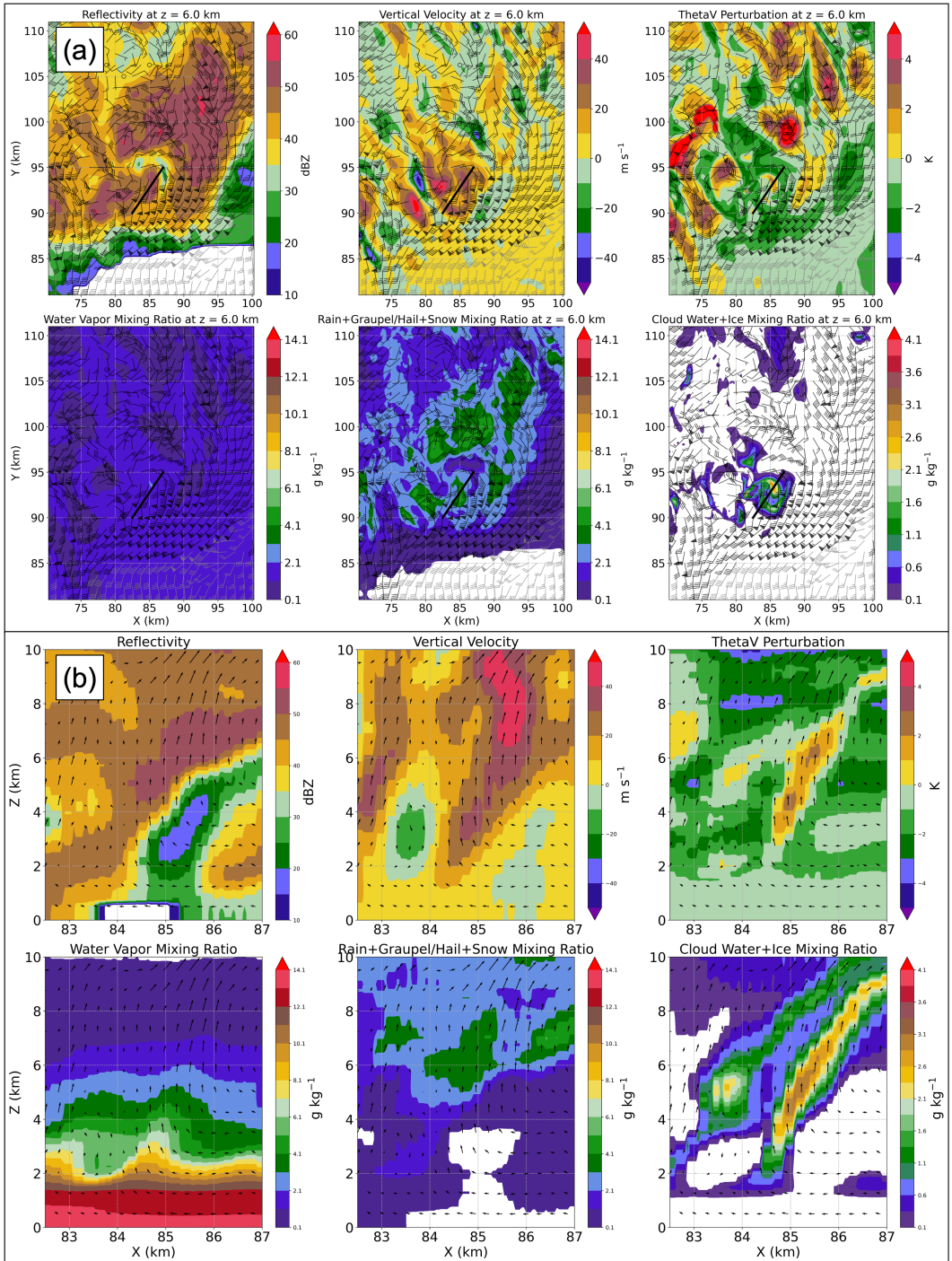


Figure 29: Same as in Fig. 27 but for 00:12 UTC.

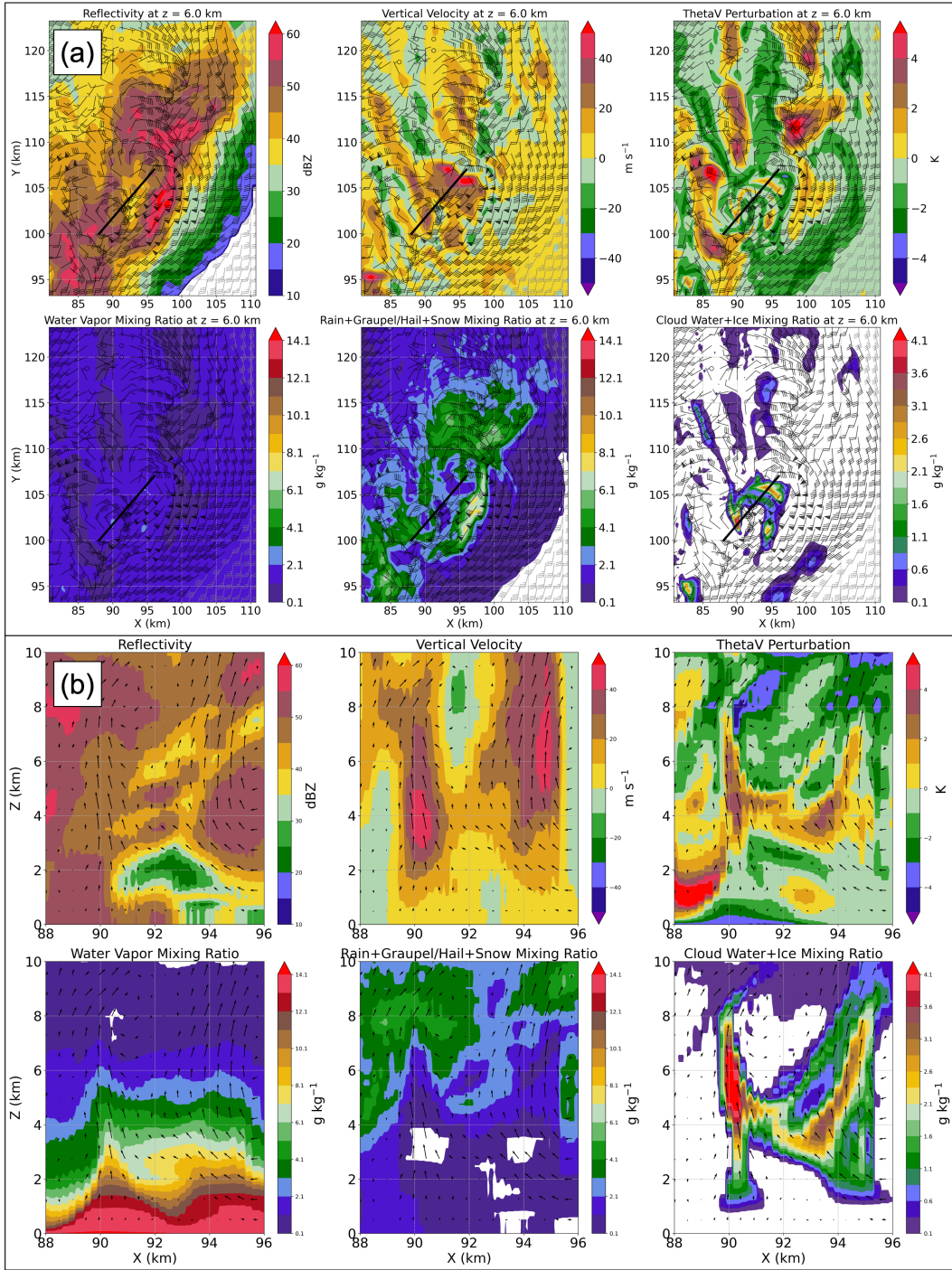


Figure 30: Same as in Fig. 27 but for 00:33 UTC.

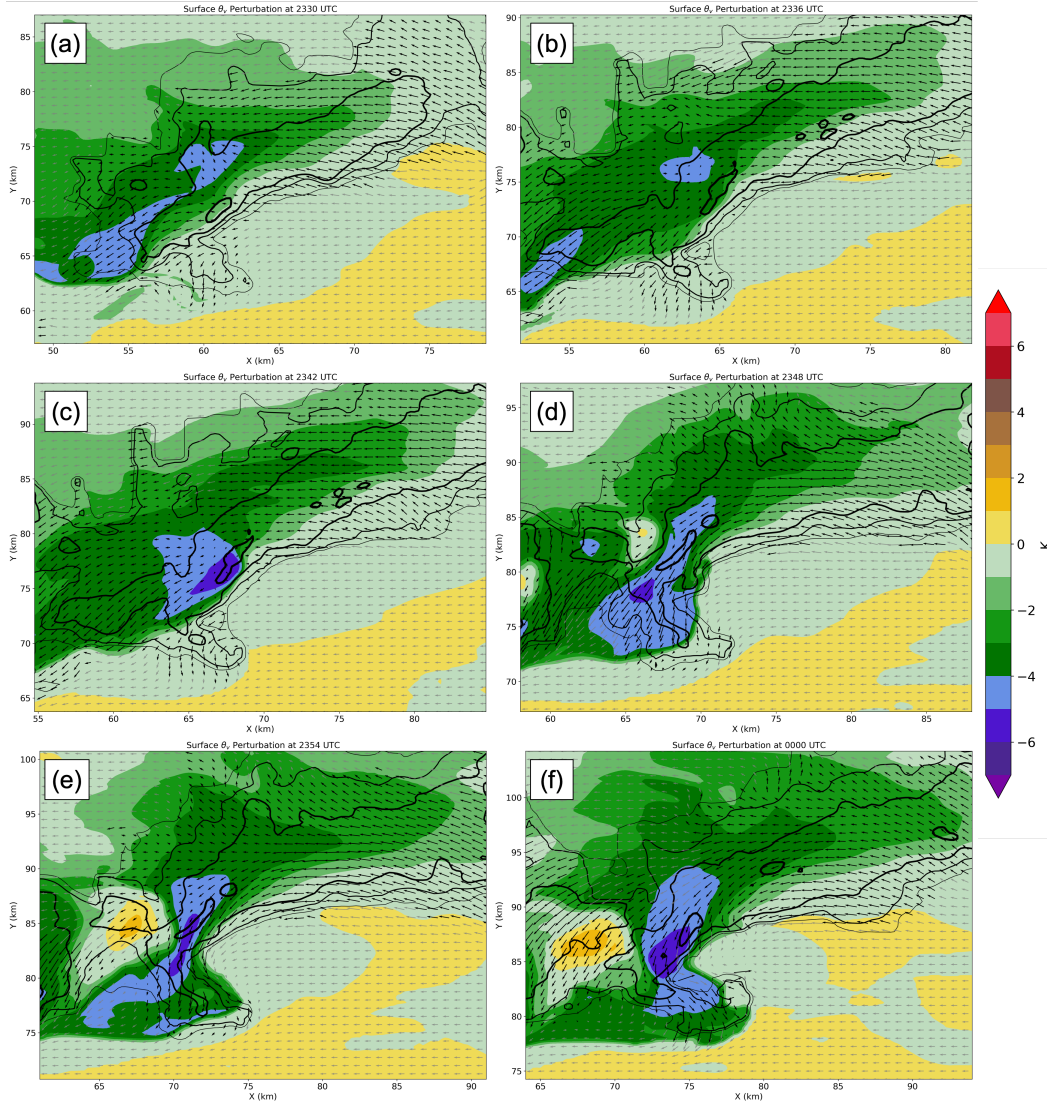


Figure 31: Surface θ_v perturbation with surface wind vectors overlaid at (a) 23:30, (b) 23:36, (c) 23:42, (d) 23:48, (e) 23:54, and (f) 00:00 UTC. The black contours are surface reflectivity, with the thickness increasing every 10 dBZ starting from 30 dBZ.

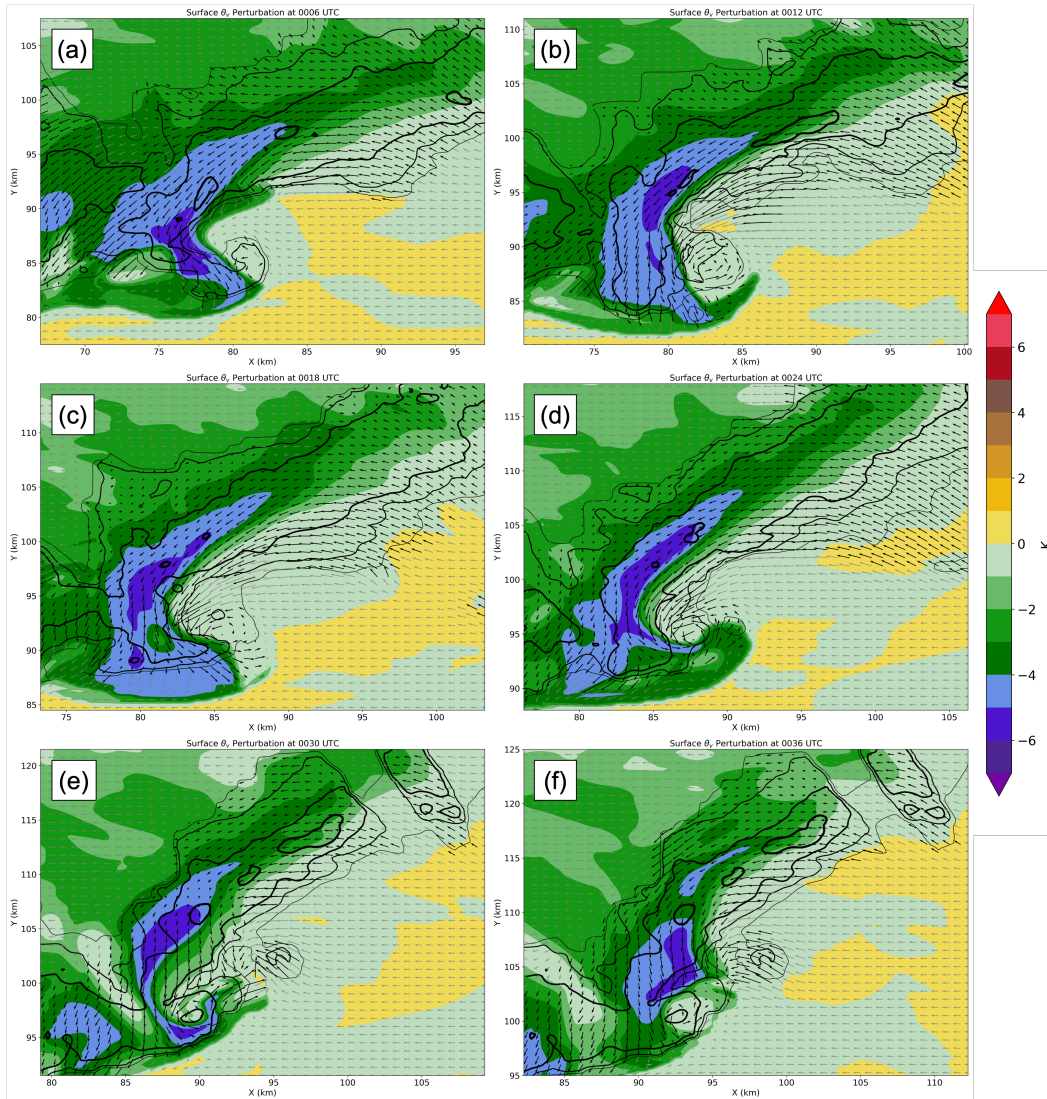


Figure 32: Same as Fig. 31 but for (a) 00:06, (b) 00:12, (c) 00:18, (d) 00:24, (e) 00:30, and (f) 00:36 UTC.

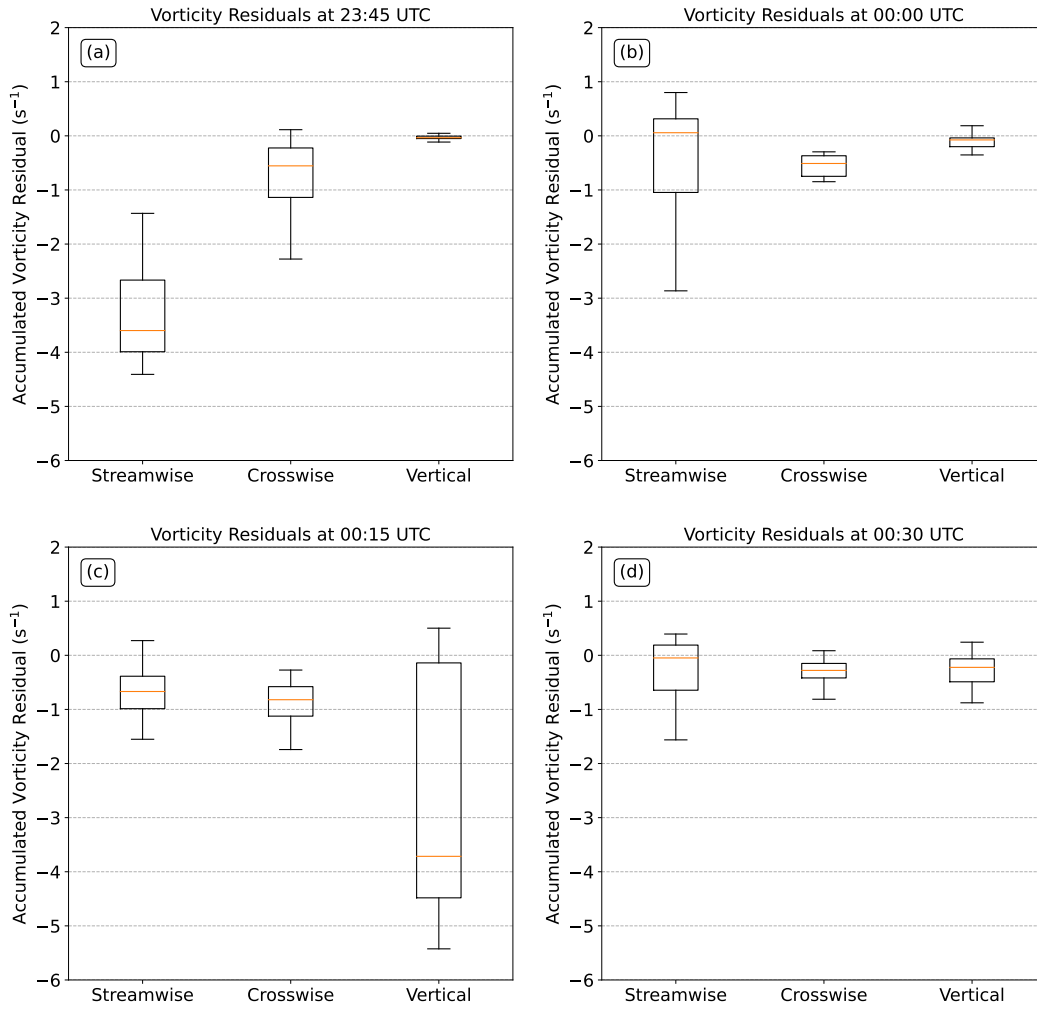


Figure 33: Boxplots of streamwise, crosswise, and vertical vorticity accumulated residuals along the 36 trajectories over the 15 min for (a) 23:45, (b) 00:00, (c) 00:15, and (d) 00:30 UTC.

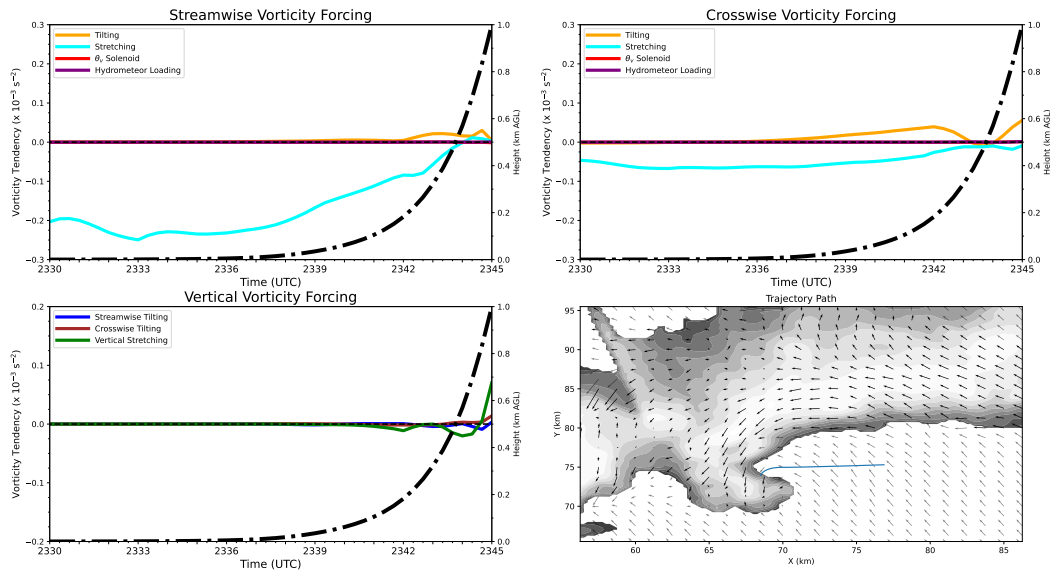


Figure 34: Vorticity tendency associated with forcing terms for streamwise (top left), crosswise (top right), and vertical vorticity (bottom left), along with the trajectory path superimposed on gray shaded reflectivity and 1 km AGL wind vectors at 2345 UTC (bottom right).

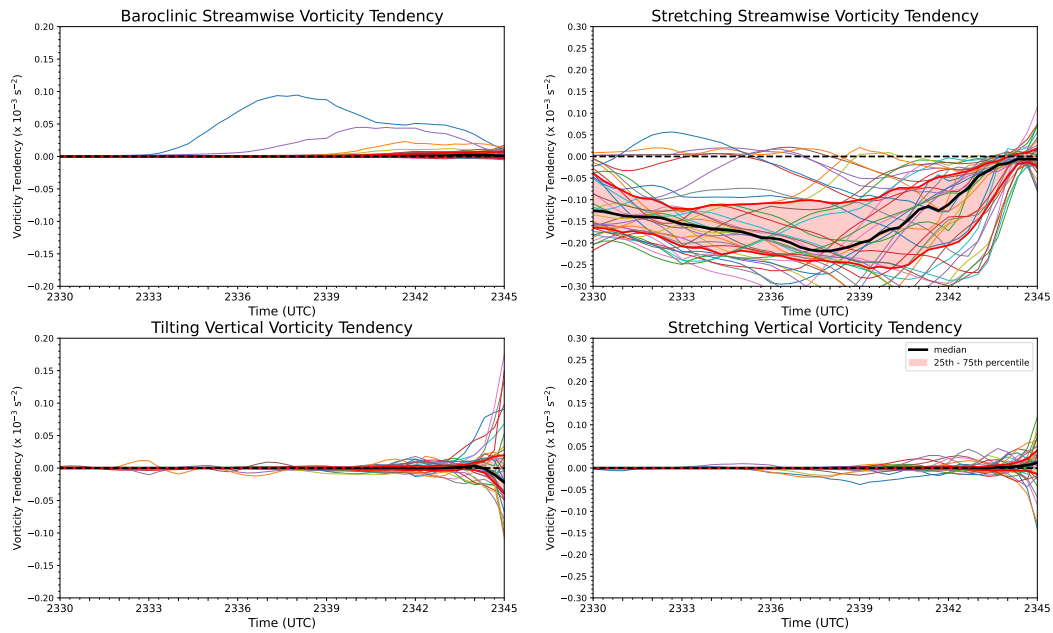


Figure 35: Vorticity tendency along 36 trajectories related to forcing associated with baroclinic streamwise vorticity (top left), stretching of streamwise vorticity (top right), tilting of horizontal vorticity into the vertical (bottom left), and stretching of vertical vorticity (bottom right). Colored lines represent each trajectory. The black line represents the median value and the red lines (and red shading) represent values in between the 25th and 75th percentiles.

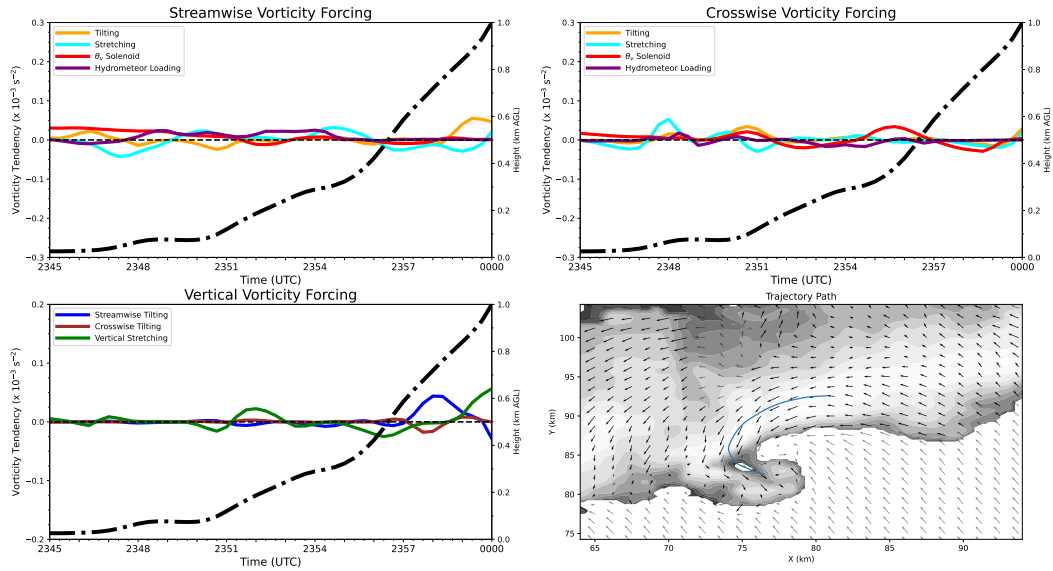


Figure 36: Same as Fig. 34 except for a trajectory terminating at 00:00 UTC.

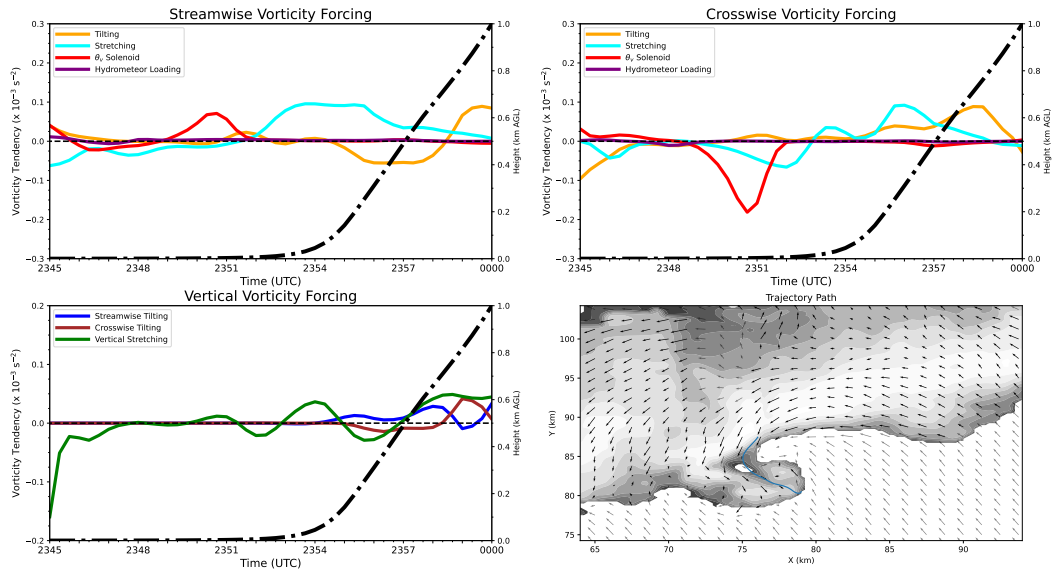


Figure 37: Same as Fig. 36 except for a different trajectory terminating at 00:00 UTC.

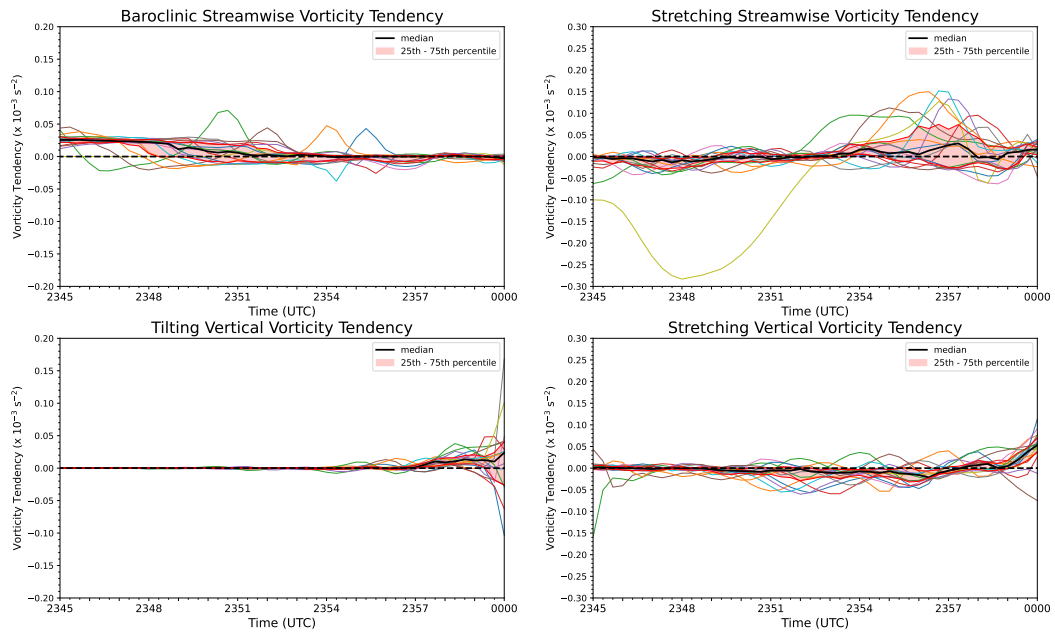


Figure 38: Same as Fig. 35 except for all trajectories terminating at 00:00 UTC which have an observed ζ value greater than 0.01 s^{-1} .

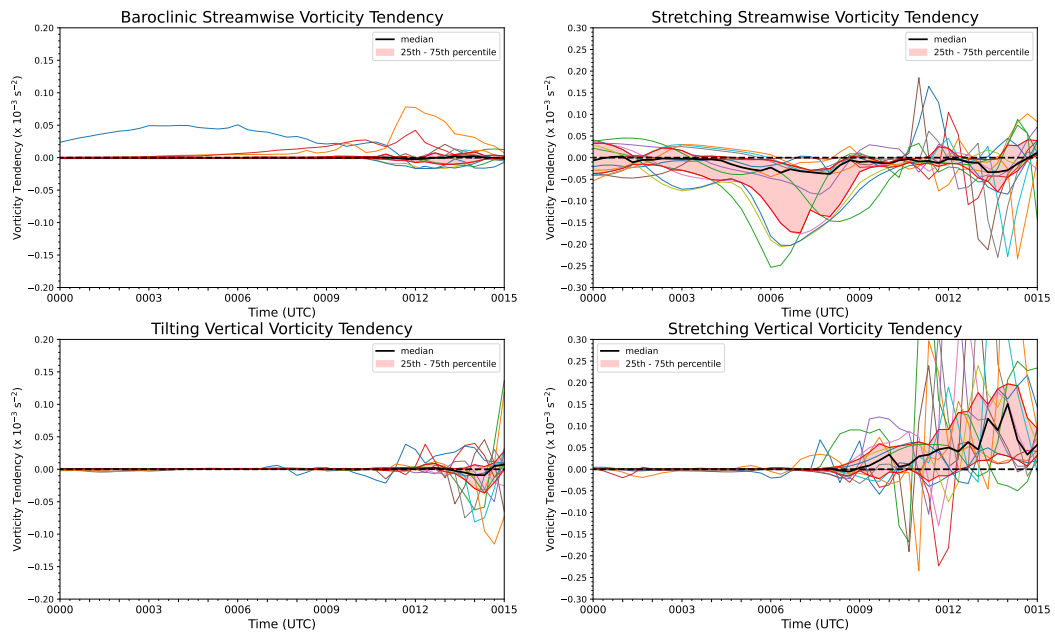


Figure 39: Similar to Fig. 35 except for trajectories terminating at 00:15 UTC which have a path through the forward-flank region (manually identified).